THE ANALYSIS OF FRACTURED Ti-6Al-4V MODULAR REVISION HIP STEMS WITH THE USE OF RADIOGRAPHIC ASSESSMENT, FINITE ELEMENT ANALYSIS, AND MECHANICAL TESTING

BY

PRIYA L.N. NAYAR

A Thesis submitted to the Faculty of Graduate Studies of

The University of Manitoba

in partial fulfillment of the requirements for the degree of

MASTER OF SCIENCE

Department of Mechanical and Manufacturing Engineering

University of Manitoba

Winnipeg, Manitoba, Canada

The Analysis of Fractured Ti-6A1-4V Modular Revision Hip Stems with the Use of Radiographic Assessment, Finite Element Analysis, and Mechanical Testing

BY

Priya L.N. Nayar

A Thesis/Practicum submitted to the Faculty of Graduate Studies of The University of Manitoba in partial fulfillment of the requirement of the degree

Of

MASTER OF SCIENCE

TABLE OF CONTENTS

ACKNOWLEDGEMENTS

I would like to express my deepest gratitude to Dr. J. R. Cahoon for granting me the opportunity to work on such an interesting and developing topic of research. I am also sincerely grateful to Dr. William Caley and Dr. Eric Bohm. My three advisors provided valuable guidance, supervision, and support throughout the duration of this work. I would also like to thank Dr. Olanrewaju A. Ojo for his guidance and encouragement. I acknowledge Dr. Norman L. Richards and Martin Petrak for their valuable insight.

I would also like to acknowledge the technical assistance from Irwin Penner, Daniel Rossong, Don Mardis, John Van Dorp, Dan McCooeye, Kim Majury, Mike Boskwick, and Wayne Forsey. I am grateful to all of the graduate students in the Materials Department. I would like to thank Concordia Hospital for supplying all of the modular implants examined in this study. I acknowledge the financial support from the Natural Sciences and Engineering Research Council of Canada (NSERC) and the Gibson Fund, University of Manitoba, Section of Orthopaedics. Finally, I would like to thank my family and friends for their love and support.

ABSTRACT

Five failed retrieved modular Ti-6Al-4V hip stems were examined to determine causes of failure. Investigation included microscopic and macroscopic analysis, finite element analysis, and mechanical testing of the modular hip implant. Method of failure was found to be fatigue, with crack initiation occurring on the lateral side of the modular junction. Bony ingrowth across the modular junction and on the proximal body was not present on both medial and lateral sides. Finite element analysis confirmed that the highest point of stress was where the crack was initiating, its magnitude, and that by utilizing a medial bone support, overall stresses on the modular implant decreased significantly. Tensile and hardness tests of the stem material produced results that were consistent with standard values. Fatigue results followed typical S-N curves and indicated that failure in vivo should have occurred after 10 million cycles. Implant assembly involves pulling the stem into the body. This created residual tensile stresses and decreased the fatigue life of the implant. Failure was found to be dependent on the material's modulus of elasticity.

LIST OF FIGURES

LIST OF TABLES

CHAPTER 1

INTRODUCTION

1.1 Purpose

This study was undertaken to examine the causes of failure of fractured modular titanium-based total hip replacement stems. A better understanding of the performance of such implants was gained with the objective of minimizing fractures in vivo.

1.2 Problem

Over the course of one year, the University of Manitoba Joint Replacement Group (UMJRG) has collected five fractured modular revision hip implants. These implants have fractured at the same modular junction on the implant, with crack initiation occurring on the lateral side. Since this is a commonly used design of implant, its mode of failure requires a thorough examination to prevent future fractures and subsequent revision surgery. The modular hip implant needs to be thoroughly analyzed to gain a better understanding of the reason of failure.

1.3 Scope

This work provides an introduction to orthopaedic hip replacement surgery, an overview of the current materials being used for orthopaedic hip implants and the current problems that they are facing, the importance of stem fixation and stability, as well as an

introduction to hip revision surgery. The modular revision hip implant is introduced, along with the specific problems with this system. Once sufficient background information is provided, research methods in this project are discussed. These include microscopic and macroscopic analyses, finite element analysis, and mechanical testing. Experimental results are discussed and from this, conclusions are determined. Finally, recommendations are made for further work in this developing area of research.

Methods of research include studying previous publications in orthopaedics and materials science, such as journal articles and related textbooks. Experimental work and consultations with professionals in the field of orthopaedics and engineering also contribute to the findings of this research project. Research work for this thesis project is limited to the modular hip implant system. Reference to other models of hip implants is used for comparison purposes only.

CHAPTER 2

BACKGROUND

2.1 An Introduction to Orthopaedic Hip Replacement Surgery

In the hip joint, the femoral head sits in the acetabulum. This acts as a ball-and-socket joint. The acetabulum is made up of three bones that are part of the pelvis: the illium, the pubis, and the ischium. These three bones come together to form the socket. This can be seen below in Figure 1:

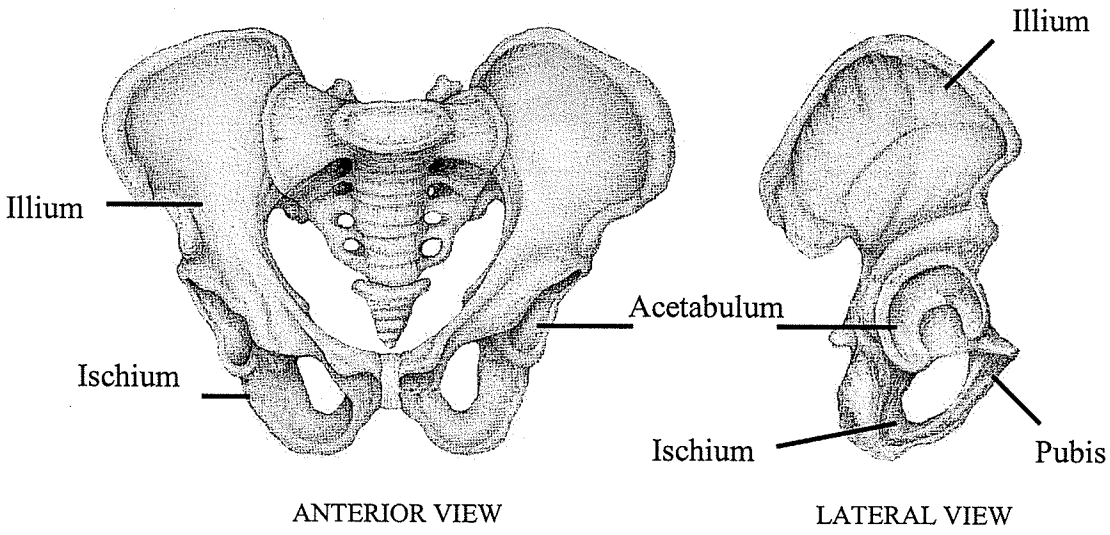

FIGURE 1: THE HUMAN PELVIS [1 - MODIFIED]

The ball-like head of the femur sits in the acetabulum. The femoral head is connected to the femoral neck. On the distal side of the neck, there are projections on the femur called the greater trochanter and the lesser trochanter. This then connects down to the shaft of the femur, which descends down to the knee joint.

The femur is commonly known as the "thigh bone", since it is the only bone in the thigh. Because of this, it is also the longest, largest, and strongest bone in the body. The complete femur can be seen below in Figure 2.

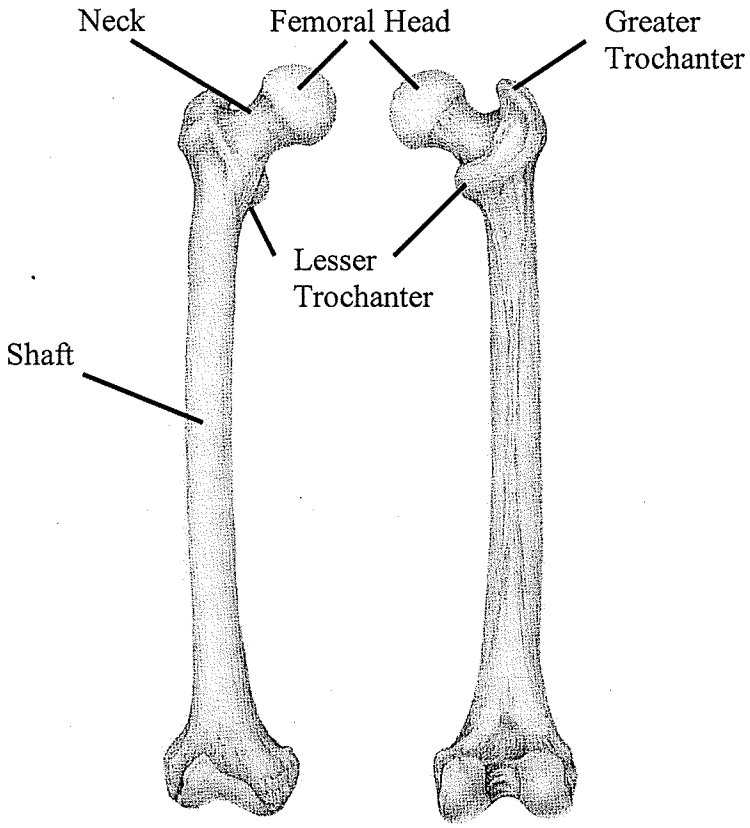

FIGURE 2: THE HUMAN FEMUR [1 - MODIFIED]

There are many forces that act on the hip joints since they must carry the entire weight of the upper body. In fact, the hip joint carries up to three times that of a person's body weight during normal gait [2]. Due to the high forces at the articulating joint, as a person ages and bone becomes weaker, fracture here becomes more likely if acute trauma occurs, such as a slip or a fall. In addition, bone deficiencies such as osteoporosis and

arthritis become more common, which cause the articulating surfaces in the hip joint to degrade and become unstable.

In both of these cases, a person is likely to require a total hip replacement (THR). This is also called a primary surgery. Prior to this surgery, a person is assessed to determine exact sizes of implants required. There are six major orthopaedic implant companies that manufacture and distribute implants in Canada and the United States. These will be mentioned in a subsequent section.

Every year, orthopaedic surgeons perform thousands of THR's and total knee replacements (TKR's). In the year 2001-2002, a total of 44,792 THR and TKR surgeries were performed in Canada. Due to North America's aging population, this total number increases every year. In the past seven years, the number of THR and TKR surgeries has increased by 39% [3]. In Manitoba alone, there were 2111[1] THR and TKR surgeries done in the 2004-2005 year. For the year 2005-2006, this number was projected to increase to 2820[1] [4]. Many of these surgeries are revision surgeries due to reasons that will be discussed later.

During a THR, the femoral head is cut off and a canal is reamed down the shaft of the femur. Once this is done, a metal stem is inserted in the canal. At the proximal end of the stem, there is a ball that replaces the original femoral head. The acetabulum is reamed out to remove the degraded bone and a metal cup is inserted in the socket. Certain models of acetabular cups require a metal cup and a polyethylene, ceramic, or metal insert. This surface will articulate with the head of the implant and form the new hip joint in the patient. An image of this can be seen below in Figure 3:

---

[1] This number does not include partial hip or emergency surgeries. [4]

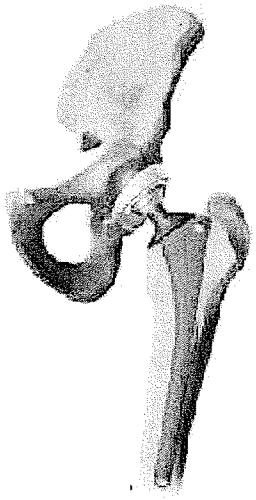

FIGURE 3: ANTERIOR VIEW OF A TOTAL HIP REPLACEMENT AT THE HIP JOINT [5]

If the patient has a fractured hip, but the acetabulum is not degraded, a THR is not always necessary. In cases like this, a partial hip replacement is sufficient, where only the femoral component of the implant is used.

2.2 Current Materials Being Used For Orthopaedic Hip Implants

In general, a hip implant is made up of four components: the femoral stem, the femoral head, the acetabular cup, and the acetabular liner. In some designs, the acetabular liner and the cup come as one component. A typical hip implant can be seen in Figure 4:

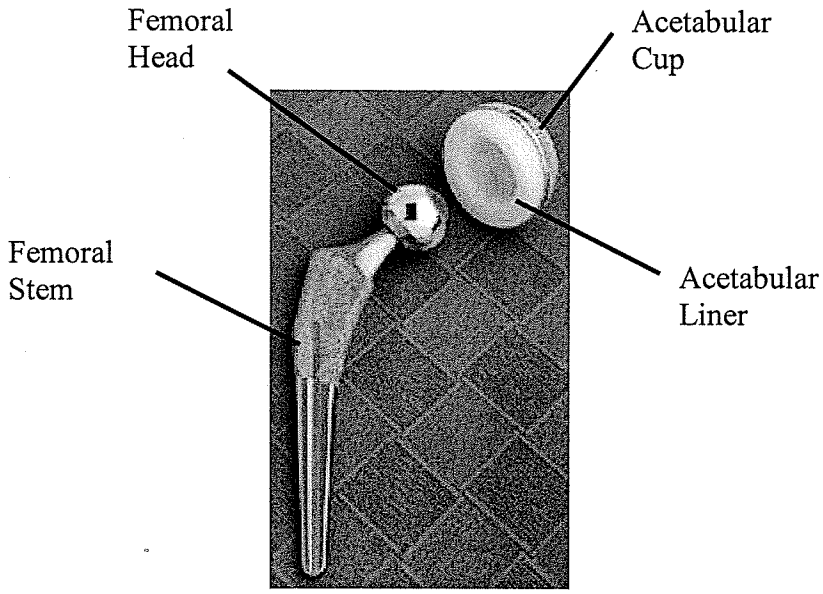

FIGURE 4: A TYPICAL ORTHOPAEDIC HIP IMPLANT [6]

There are several materials that are used to make these components of the femoral stem. Some of these materials are alloyed into different variations to produce the most desirable properties. Despite what material is being used, all hip implants must have similar characteristics: they must have high strength and fatigue characteristics, they must be corrosion and wear resistant, and they must be biocompatible.

The modulus of elasticity, E, or Young's modulus, of the material is important as well. This value is measure of stiffness, or resistance to strain, in a material. Human bone is an anisotropic material, which means that it has different mechanical properties in different directions. Some of these properties can be seen in Table 1:

TABLE 1: MECHANICAL PROPERTIES OF HUMAN LONG BONE [7]

Property	**Parallel to Bone Axis**	**Perpendicular to Bone Axis**
Modulus of Elasticity, GPa (psi)	17.4 (2.48×10^6)	11.7 (1.67×10^6)
Ultimate Strength, Tension, MPa (ksi)	135 (19.3)	61.8 (8.96)
Ultimate Strength, Compression, MPa (ksi)	196 (28.0)	135 (19.3)
Elongation at Fracture	3 - 4%	-

From the above table, it can be seen that parallel to the bone axis, its E = 17.4 GPa and perpendicular to the bone axis, its E = 11.7 GPa [7]. It is desirable for the selected material for a hip implant to have a low stiffness value, which will make it closer to the value of E for bone. If this is accomplished, the implant will behave more like bone in the body and will promote bone ingrowth into the implant. If the material's stiffness is too high, atrophy and resorption of the surrounding bone are more likely.

Developing proper bone adhesion to the implant is extremely important for implant stability and life. There are several ways of accomplishing this, depending on whether the implant does or does not require bone cement to accompany it in placement in the femur.

In general, if the femoral component is completely smooth, the implant requires bone cement as a grout. Bone cement is a compound commonly composed of 90% polymethylmetacrylate and 10% barium sulfate or zirconium oxide. The latter 10% of this compound allows bone cement to be radio-opaque [8]. This means that x-rays will not be able to penetrate it and thus bone cement is visible in radiographs. Bone cement is

a thermosetting material. Therefore, once heated and cooled to room temperature, it becomes permanently hard [8].

Unlike the smooth stem of a hip implant that requires cement, a cementless hip stem is macrotextured. The topography that is created on the stem allows bone to grow into it and causes fixation. This textured surface on the hip stem is created by using plasma spray and is made from a similar material as the hip stem. For example, a Ti-6Al-4V alloy stem is plasma sprayed with titanium. In some cases where bone density of the patient is low and/or bone growth is minimal, a coating of hydroxyapatite ($Ca_{10}(PO_4)_6(OH)_2$) will be added to the surface of a metallic hip stem. Hydroxyapatite is chemically similar to the mineral component in human bone and promotes osseointegration to the hip stem. These features ensure proper fixation of bone to the cementless hip stem.

The main materials that are used for femoral components will be outlined in this section. These materials include stainless steel, cobalt-chrome, ceramic, and titanium. Some of the properties of the main metals used are shown in Table 2. These include 316L stainless steel, MP35N (Co-Ni-Cr-Mo), and Ti-6Al-4V.

TABLE 2: MECHANICAL AND CORROSION PROPERTIES OF THE MOST COMMON METALLIC ALLOYS USED FOR FEMORAL COMPONENTS OF HIP IMPLANTS [7]

Alloy	**Modulus of Elasticity, GPa (psi)**	**0.2% Yield Strength, MPa (ksi)**	**Tensile Strength, MPa (ksi)**	**Elongation at Fracture, %**	**Fatigue Strength or Limit, 10^7 Cycles, MPa (ksi)**
316L Stainless Steel (cold worked)	196 (28.4×10^6)	700 (102)	875 (127)	12	383 (55.5)
MP35N (hot forged)	230 (33.4×10^6)	1000 (145)	1200 (174)	13	500 (72.5)
Ti-6Al-4V (hot forged)	120 (17.4×10^6)	950 (138)	1075 (156)	13	420 [9] (60.0)

Some of the values in Table 2 will be discussed further in the following sections.

2.2.1 Stainless Steel

In general, older designs of hip implants are made out of stainless steel, where the femoral stem and the femoral ball are both made from this alloy. Stainless steel is still used in some newer designs, where only the femoral stem is made from it and the ball is made from a different material, such as a cobalt-chrome alloy or ceramic. The most common form of this alloy used in vivo is 316L stainless steel. It has moderate strength, but may be susceptible to a modest amount of crevice corrosion. It also has a lower fatigue strength compared to Ti-6Al-4V and MP35N. Due to these material characteristics, 316L stainless steel hip implants are generally used in elderly and less active patients [7].

2.2.2 Cobalt-Chrome

In general, there are two types of cobalt-chrome being used for orthopaedic hip implants: a cobalt-chrome-molybdenum casting alloy (Co-Cr-Mo) and a cobalt-nickel-chromium-molybdenum wrought alloy (Co-Ni-Cr-Mo) [7]. Cobalt-chrome alloys have very high resistance to wear and corrosion. Therefore, because of these properties and the fact that there are high stresses when the femoral head articulates with the acetabular component, the head of the femoral component is generally made out of cobalt-chrome. In some implant designs, the femoral stem can be made out of a cobalt-chrome alloy.

Co-Ni-Cr-Mo (MP35N) is the most common cobalt-chrome alloy used for hip implants [7]. As shown in Table 2, it has an extremely high yield strength and tensile strength. It also has excellent corrosion resistance and fatigue characteristics, good ductility and toughness, and a high modulus of elasticity (E = 230 GPa) [7].

2.2.3 Ceramics

Some newer designs of hip implants are using ceramic materials for the femoral head. Two types of ceramic used in the body are aluminum oxide (Al_2O_3), or alumina, and zirconium oxide (ZrO_2), or zirconia. Of these, alumina is more common. Due to its high-density and high-purity polycrystalline structure, alumina is extremely hard. In fact, its hardness is second only to that of diamond [10]. Alumina also has superior corrosion and wear resistance. This material is very smooth and creates low frictional stresses when articulating with the

acetabular component at the hip joint. Therefore, due to these reasons, alumina is very biocompatible. In addition to this, the density of alumina is 3.98 g/cm^3, making it even lighter than titanium [7].

Despite these excellent characteristics, alumina has poor fracture toughness and fatigue strength. It also has a very high modulus of elasticity (E = 380 GPa), making this a very stiff material [7]. Ceramics, in general, are very brittle and thus have low tensile strength. For these reasons, alumina is limited to the femoral head and acetabular liner and the femoral stem is made from one of the other mentioned metals.

To improve on its weaknesses, alumina can be reinforced with zirconia particles. This is more commonly called zirconia-toughened alumina (ZTA). There is also alumina-toughened zirconia (ATZ), but its properties are not as superior as ZTA [11]. Properties of these composites, as well as their monolithics, are listed in Table 3.

TABLE 3: MATERIAL PROPERTIES OF ALUMINA, ZIRCONIA, ALUMINA-TOUGHENED ZIRCONIA (ATZ), AND ZIRCONIA-TOUGHENED ALUMINA (ZTA) [10]

Material Property	**Alumina**	**Zirconia**	**ATZ (Zirconia Matrix)**	**ZTA (Alumina Matrix)**
Toughness, Mpa$\sqrt{m}$	4	7	5 - 6	7 - 8
Fatigue Limit, K_{10}, Mpa$\sqrt{m}$	2.5	3.5	2.5 – 3	5 - 6
Hardness, VPH (kg/mm^2)	1800	1200	1300	1700

It can be seen from Table 3 that ZTA has a similar hardness to that of alumina. However, ZTA has higher toughness and hardness, and has a higher

fatigue limit. Together, these properties lead to an even higher wear resistance than alumina [11].

2.2.4 Titanium

One of the most common materials that femoral stems are made out of is a titanium-based alloy. The titanium alloys that are used in vivo are all very similar in composition, but the main alloy used is Titanium-6Aluminum-4Vanadium (Ti-6Al-4V). The chemical composition for Ti-6Al-4V can be seen in Table 4.

TABLE 4: ASTM INTERNATIONAL STANDARD FOR THE CHEMICAL REQUIREMENTS OF WROUGHT TI-6AL-4V ALLOY FOR SURGICAL IMPLANT APPLICATIONS [12]

Element	**Composition, %**
Nitrogen, max	0.05
Carbon, max	0.08
Hydrogen, max	0.015
Iron, max	0.30
Oxygen, max	0.20
Aluminum	5.5 - 6.75
Vanadium	3.5 – 4.5
Yttrium, max	0.005
Titanium	balance

Ti-6Al-4V has very desirable properties for use in vivo. It is very biocompatible and will thus minimize allergic reactions, rejection in the body, and will encourage osseointegration [7]. In addition to this, Ti-6Al-4V has excellent mechanical properties, such as yield strength and tensile strength, which can be seen in Table 2. Its density is 4.43 g/cm^3, which is significantly lower than other materials used for hip stems (316L stainless steel $\rho = 8.00$ g/cm^3, cobalt-chrome

alloys $\rho \approx 8.5$ g/cm^3) [7]. This means that these stems are very light in comparison to others.

Also, Ti-6Al-4V has a lower modulus of elasticity than the other materials used for hip implants, which means that it is less stiff. Looking at Table 2, the modulus of elasticity for Ti-6Al-4V is 120 GPa, which is significantly lower than the other two materials and closer to the value of bone. Therefore, the hip stem can behave more like bone in the body, and the body is less likely to reject it. Due to this, atrophy and resorption of surrounding bone are less likely. In addition to these very desirable properties, Ti-6Al-4V has a high fatigue strength.

2.3 Current Problems That Orthopaedic Hip Implants Are Experiencing

There are several problems that hip implants encounter when they are in vivo. The main problems include wear and degradation, infections and allergies, and cracking and breaking. Each of these will be discussed briefly in the following section.

2.3.1 Wear and Degradation

Recall that the femoral head of the hip implant articulates with the acetabular component. This occurs at high forces, causing wear to happen between the articulating surfaces. The amount of wear created is dependent on which material each surface is made from. As stated before, the femoral head is generally fabricated from cobalt-chrome or a ceramic. The acetabular liner can be made from a metal, a ceramic, or polyethylene. More wear is generated when two

surfaces of different hardness are articulating together, such as a cobalt-chrome femoral head and a polyethylene acetabular liner.

When wear occurs between the articulating surfaces, debris particles are formed. This wear debris acts as grit and increases wear even further. Also, the presence of these wear particles in vivo results in an inflammatory response, releasing certain chemicals to the surrounding area. Several of these chemicals involved with inflammation have been shown to contribute to osteolysis, which is the resorption of bone [13]. This is because these chemicals cause the production of osteoclasts, which are cells that break down bone cells, and inhibit the production of osteoblasts, which are bone-forming cells. Therefore, the presence of wear particles will result in bone loss. This can lead to widening of the femoral canal or lack of proper support for the implant, causing implant loosening and the potential for implant failure.

Wear of the femoral head or the acetabular liner can cause the shape of the articulating surface to change, which could also lead to the implant failing [7]. In addition to this, the frictional forces between the articulating surfaces can cause loosening of the hip stem in the femur or the acetabular component in the acetabulum [7]. This can cause implant degradation over time.

There are other factors that can contribute to implant degradation. One major factor is that fluid in the body is an aerated and warm solution that consists of approximately 1 wt% of NaCl [7]. There are also other salts and organic compounds in minor concentrations that are found in extracellular fluid. Together, these characteristics cause the fluid to be corrosive in nature. For hip implants that

are made from a metal, this can cause corrosion of the implant, such as crevice corrosion and pitting. Also, since hip implants experience high stresses in vivo, fretting corrosion, stress corrosion cracking, and fatigue corrosion can also be a problem [7]. Each of these types of corrosion, by itself or in combination, can cause degradation of the hip implant and shorten its life significantly.

2.3.2 Infections and Allergies

As stated in the previous section, when articulation occurs between the femoral head and the acetabular component, wear debris is formed. Some of these particles can travel to the surrounding tissues and cause mild to severe inflammation [7]. In addition to this, when on-going corrosion of the hip implant occurs, corrosion byproducts are also continuously created [7]. Metallic ions, such as Ni^{2+} and Cr^{3+}, are also released from metal hip implants [14]. Corrosion byproducts and metallic ions are quickly carried throughout the body through the circulatory system. These can be very toxic and harmful to the body, leading to many adverse physiological effects, including infections, tissue responses, and allergies [14].

Biocompatibility of the implant is extremely important to avoid reactions in the body. When any foreign material is introduced in vivo, there is a rejection reaction. This reaction is dependent on how biocompatible the material is, and can range from a mild irritation or inflammation of surrounding tissue to death [7].

Body sensitivity to metallic components in hip implants can also be a problem. This can cause adverse allergic reactions in the body, ranging from mild

irritation to severe tissue response. Common elements that can cause allergies are chromium, nickel, and cobalt [15].

2.3.3 Cracking and Fracture

Hip implant fracture is a concern in orthopaedics. In one study in London, Ontario, a group of researchers gathered five fractured stems from a series of 219 patients (2.3%), ranging in age, gender, and body mass index [16]. In a similar case study, a group of researchers identified ten cases of fractured femoral stems due to fatigue occurring between 1995 and 2004 [17].

Cracking and fracture can be caused by many factors. Wear and degradation of the implant material can weaken the material and compromise its mechanical properties. Corrosion, such as pitting, can also lower the mechanical properties of the material. This can cause crack initiation to occur. Once a crack is formed in a hip implant, high stresses and corrosive extracellular fluids will encourage crack propagation. Also, the formation of a crack may cause crevice corrosion, which will also lead to crack propagation. Fracture of a hip implant can also occur by a person falling. Once a crack is initiated, the crack will propagate until the hip implant fractures and fails in vivo. This occurs due to fatigue. Fatigue is a mechanism of failure that occurs when a material is subjected to fluctuating stresses and is responsible for approximately 90% of all metal fractures [7]. Fatigue is comprised of three stages [18]. The first is crack initiation and extremely slow crack propagation. Stage 1 occupies approximately 95% of the fracture life of the material, but only 5% of the fracture surface [19]. The second

stage is crack propagation, where the crack will start to propagate through the material faster and create microscopic bands, or fatigue striations, and macroscopic bands of crack tip propagation, or beachmarks [7]. The final stage of fatigue is final fracture, which is sudden catastrophic failure [18].

2.4 Stem Fixation and Stability

Stem fixation and stability of the implant system are crucial factors that mitigate implant fracture. According to Engh et al., there are three levels of fixation: bony ingrowth, fibrous ingrowth, and loose [20]. In the best case, bony ingrowth will occur into the hip implant. When this occurs, there will be no reactive lines present and there will be spot welds present on the radiograph. A reactive line is classified as a gap between the implant and the cancellous bone. This can be seen in patient radiographs as a dark line outlining the implant in the femur. A spot weld is a denser extension of bone that attaches to the porous surface of the implant in one spot [20]. An example of a fixated stem with no reactive lines and where spot welds are present is shown in Figure 5.

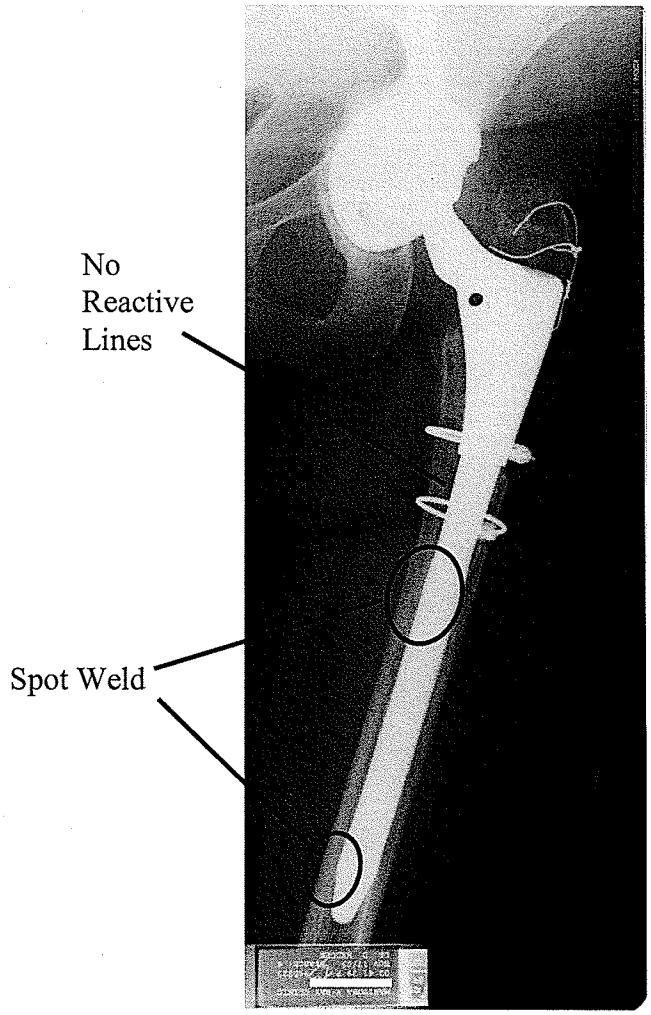

FIGURE 5: A MODULAR IMPLANT THAT HAS PROPER STEM FIXATION IN THE FEMUR

Figure 5 shows the lack of reactive lines and that the cancellous bone of the femur is grown into the porous surface of the stem of the modular implant. The presence of two spot welds is labeled in the image.

Fibrous ingrowth occurs when osseointegration has not occurred, but fibrous tissue has ingrown into the implant. There are reactive lines surrounding the hip implant and there are no spot welds present [20]. However, by examining patient radiographs over a period of time, there will typically be no subsidence. Subsidence of the hip

implant, which is also known as migration, is diagnosed when there is an increase in vertical distance between the implant and the tip of the greater trochanter over consecutive radiographs [20]. In this case, the implant subsides down into the femur, showing signs of instability.

Finally, the third level of fixation is where the hip implant is loose in the femur. In this case, there are reactive lines surrounding the hip implant, no spot welds present, and subsidence has occurred over consecutive radiographs [20]. This is the least desirable case. When the implant is loose, other signs of instability may emerge as well. These include pedestals, calcar hypertrophy/atrophy, and interface deterioration and particle shedding [20].

According to Wolff's Law, pedestals form in the canal of the femur to support the distal tip of the stem. Wolff's Law is a premise that bone will adapt according to the stresses that are applied to it. Although originally suggested in a strict mathematical sense, current usage normally involves only the general concept that mechanical loads on bone influence its structure [21]. In other words, bone deposition will occur at points of high stress, and alternately, bone will resorb at points of low stress. Therefore, when the distal tip of the stem subsides and applies stress to the edge of the canal of the femur, bone deposition occurs at that spot and a pedestal forms. In some cases, pedestals can extend over the entire width of the femoral canal [20].

Calcar hypertrophy/atrophy occurs when there is a change in bone density at the medial proximal end of the femur [20]. Hypertrophy will occur when bone deposition occurs, whereas atrophy will occur when bone resorption occurs.

Interface deterioration and particle shedding can also indicate instability of the hip implant in vivo if there is a change over consecutive radiographs. Interface deterioration involves the formation or widening of reactive lines. Particle shedding occurs when particles of metal from the implant have formed surrounding the stem [20].

2.5 Introduction to Orthopaedic Hip Revision Surgery

Although the purpose of a primary THR surgery is to resolve a patient's problems with his or her hip, this does not always happen. In some cases, the patient will require a revision surgery. This can be due to a number of reasons, such as excessive wear, infection, or implant fracture. In any of these cases, the patient requires surgery again and a new implant is inserted to replace the old one. By performing a revision surgery, problems with the hip implant that the patient had prior to surgery will be resolved. If this is not the case, then a second revision surgery is required. Although it is rare, a third revision surgery is possible as well.

As mentioned before, there are six major orthopaedic implant companies that manufacture and distribute hip implants in Canada and the United States. Each of these companies has their head quarters in the United States, with a corporate and sales extension located in Canada. These companies are Zimmer, Inc., DePuy Orthopaedics Inc. (a Johnson & Johnson company), Styker Orthopaedics, Smith & Nephew, Biomet Inc., and Wright Medical Technology, Inc. These companies supply implants for both primary and revision surgeries.

2.6 The Modular Revision Hip Implant

Although most hip stems are similar to that of Figure 4, not all models resemble this design. In some cases, instead of a single part, the femoral component is made up of three separate parts that fit together. This is called a modular hip implant. An example of this design that has been removed from a patient can be seen in Figure 6.

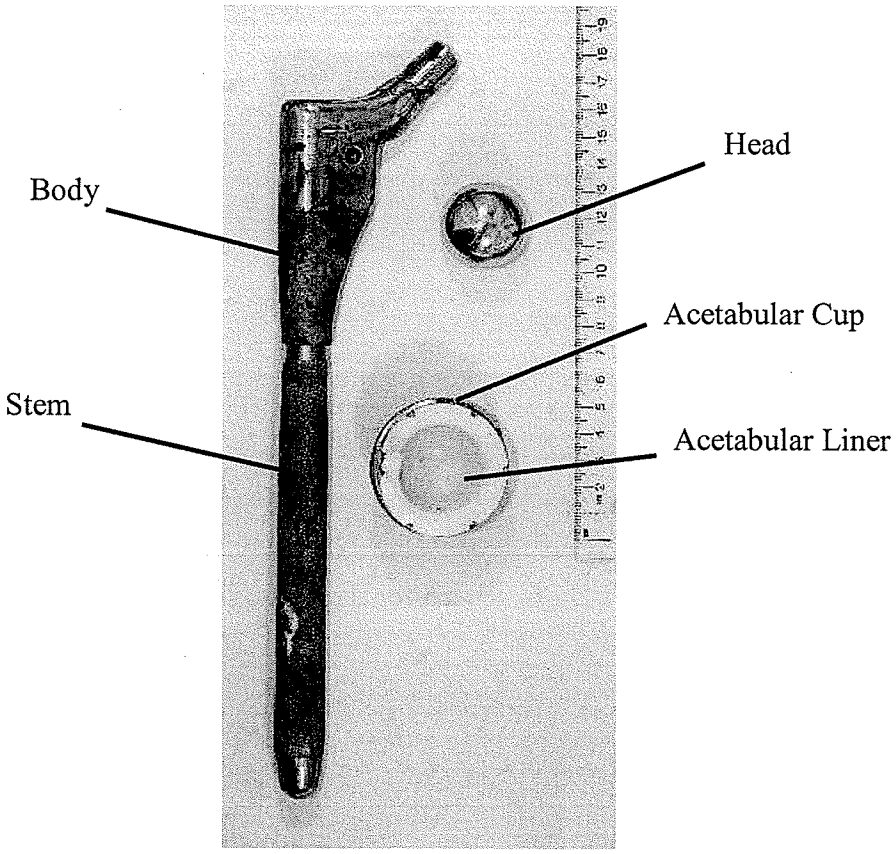

FIGURE 6: A MODULAR HIP SYSTEM

Figure 6 shows that a modular femoral component is made up of a stem, a body, and a head. The stem and the body are made from Ti-6Al-4V and are plasma sprayed with titanium to provide a textured surface for osseointegration. The femoral head is made from a cobalt-chrome alloy.

Irrespective of the manufacturer, careful preoperative planning goes into selecting the appropriate hip implant for the patient. The amount of bone loss is examined in the patient radiographs to determine the type of implant that is best suited to repair the hip and if any additional requirements are necessary, such as bone grafts, cables, or plates. Once this is done, the implant sizes are determined using templates and patient radiographs to provide a stable hip. Determining the parameters of the hip to restore proper joint motion, such as leg length, are also found. After this, the acetabulum is examined to determine if surgery is required there as well and how acetabular reconstruction would affect the femoral component of the implant [22].

For the modular hip system, when the appropriate hip implant components are chosen and are ready for insertion into the patient during surgery, the tapered, non-plasma-sprayed-end of the stem is pulled up into the body of the implant with approximately 4,893 N (1,100 lbs) using a special tool [23]. Using a torque wrench, a compression nut is securely tightened to approximately 15 N·m (130 in·lbs) on the end of the stem that is in the body of the implant [22]. The femoral head is simply hammered onto the trunion of the body.

Since this type of femoral component is modular, it is easier to obtain the perfect fit for any size of patient. Also, this means that fewer implants need to be kept on hand during the surgery to accommodate the patient. These make it much more flexible and convenient for hip surgery compared to non-modular hip implants.

2.7 Problems That the Modular Revision Hip Implants Are Facing

Although the modular hip system provides more flexibility for accommodating different patient sizes, the modular junction introduces some problems. Interface behaviours, such as micro-motion, are introduced on the implant at each junction. Also, by creating an interface where the stem and body meet, stress risers and a potential point of fracture have been introduced to femoral component. A close-up view of the junction can be seen in Figure 7.

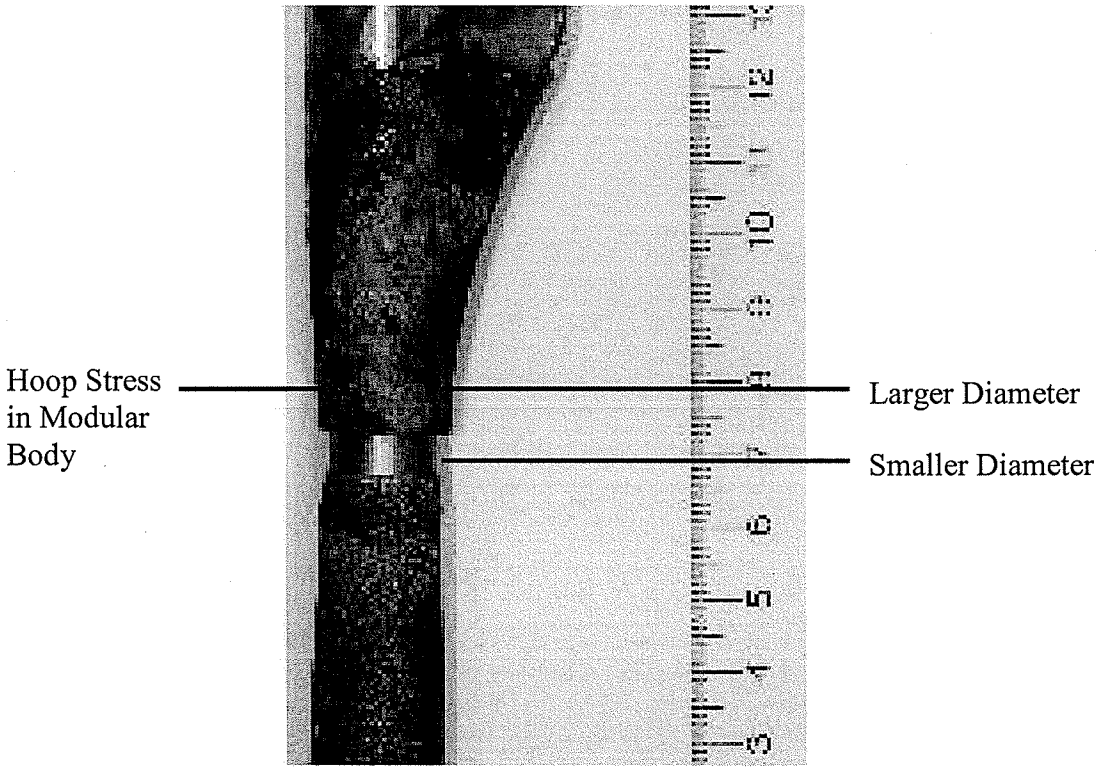

FIGURE 7: CLOSE-UP OF THE MODULAR JUNCTION

First, Figure 7 shows the modular junction of the stem and the body. The diameter of the stem by itself is smaller than the diameter of the body with the upper part of the stem inside of it. This creates a stress riser at the junction since the part goes from a

larger diameter to a smaller diameter, with a sharp corner separating the two. Second, when the stem is pulled up into the body component and then tightened, high compressive forces are introduced all around the stem inside the body of the implant (i.e. hoop stress). This hoop stress tends to introduce a circular notch on the modular stem. The combination of a stress riser due to section change and the presence of a notch possibly introduced by the circumferential stress of the implant body dictate that if the hip implant fractures, the break would likely occur at the modular junction.

Before fracture of the hip implant can occur, a crack must be initiated. Once the crack forms, the crack will propagate due to the continuous cyclic load applied and the hip stem will fail from fatigue. Also, since extracellular fluid is corrosive, crevice corrosion in the crack could drive crack propagation and accelerate the failure of the implant. The progression of implant failure can be seen in Figure 8.

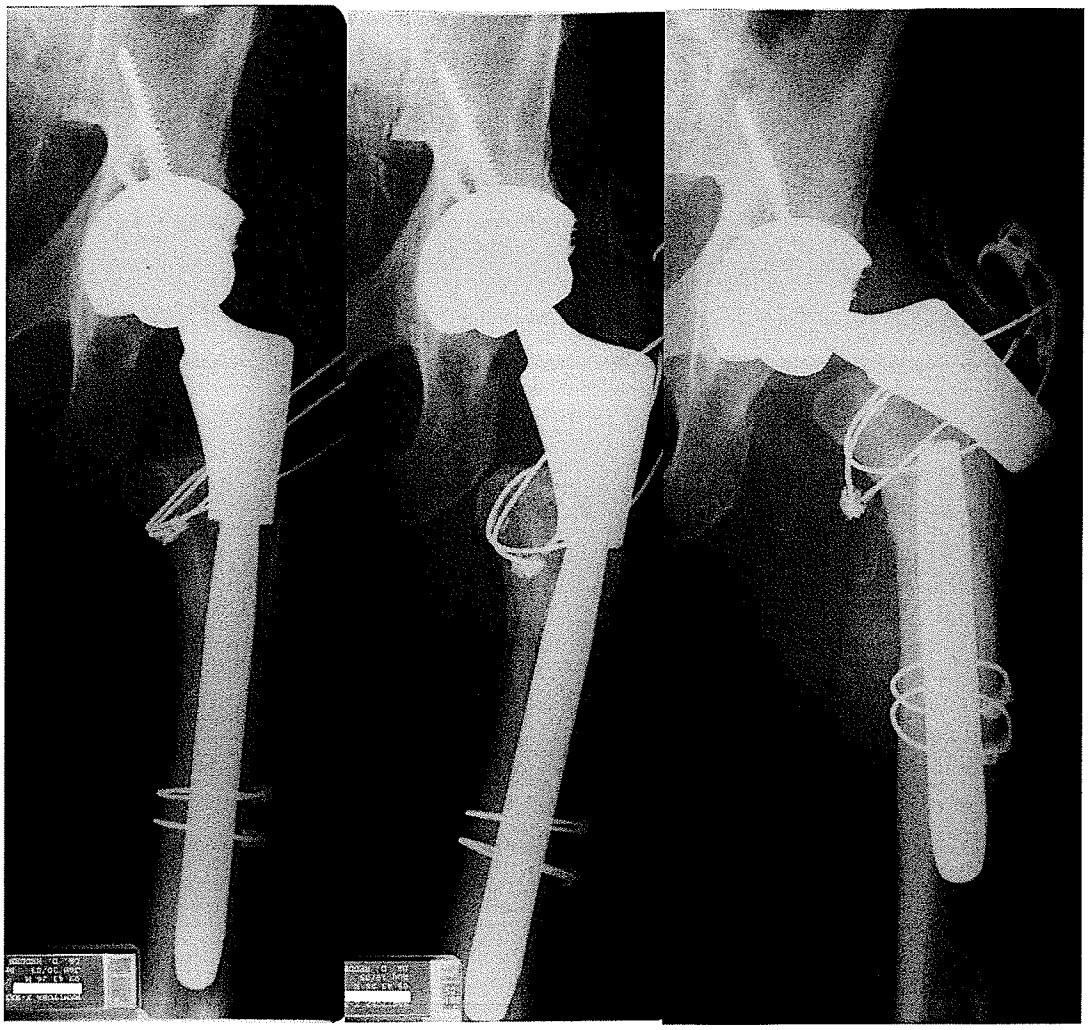

(A) (B) (C)

FIGURE 8: PROGRESSION OF MODULAR IMPLANT FAILURE, (A) 9.5 MONTHS IN VIVO, (B) 40 MONTHS IN VIVO, (C) 40.5 MONTHS IN VIVO

Figure 8 shows the progression to failure of the same modular implant implanted in the body. Figure 8(A) shows the modular hip system after being implant for only 9.5 months. It can be seen that the axis along the stem and the body components is straight. However, in Figure 8(B), the axis along these components is starting to bend. This would indicate crack initiation has already occurred. Figure 8(C) shows the same implant less than two weeks later, where the proximal end is completely separated from the distal end.

Over the course of approximately one year, the UMJRG at Concordia Hospital in Winnipeg, Manitoba, Canada collected five failed modular hip implants. These implants fractured at the same modular junction on the implant. Since it is still commonly used, the failure of the modular hip implant requires examination to better understand the causes of failure and to investigate ways to mitigate the clinical risk. Failed implants, such as those being investigated here, play a significant role in the study of prostheses, their performance in vivo, and for advances in orthopaedic technology, which can lead to safer and more reliable joint replacement for patients.

CHAPTER 3

METHODS OF ANALYSIS

It is hypothesized that failure was due to material or design defect. Possible material defects include improper strengths, high inclusion content, and porosity. Other defects include failure by corrosion (i.e. crevice corrosion, corrosion fatigue, and pitting corrosion), stress corrosion cracking, and fatigue.

This study utilizes five fractured stems collected over a one year period. Patient information including as age, gender, weight, and the implanted time were extracted from the UMJRG arthroplasty patient database, patient medical records, and operative reports. Each patient consented to having his/her implant(s) and personal information studied for research. The five implants from each of the five patients studied can be seen below in Figures 9-13.

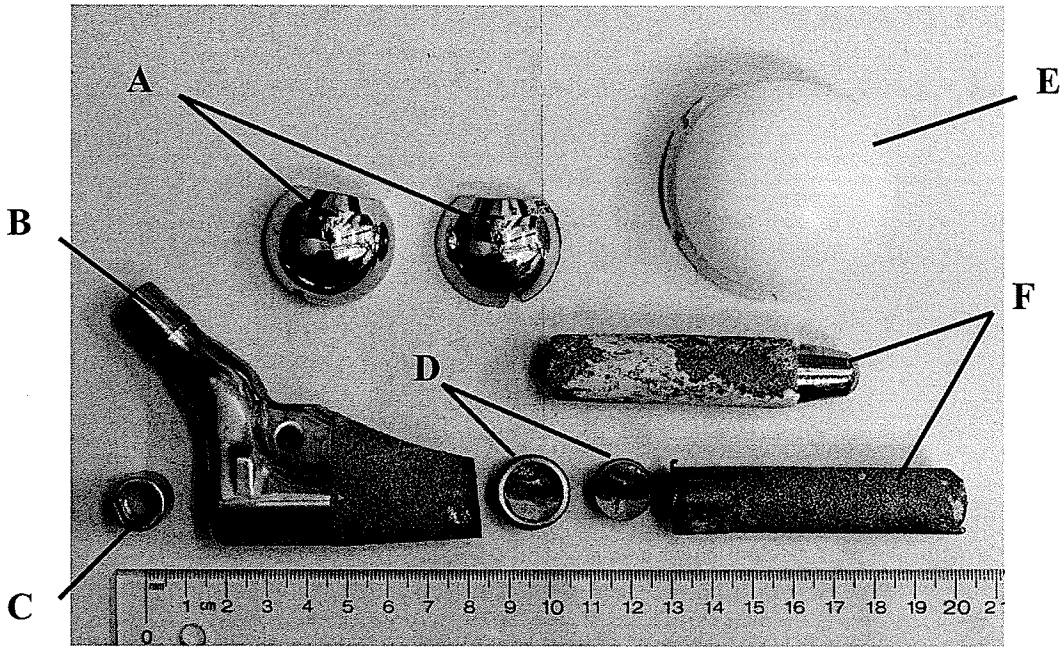

FIGURE 9: MACROSCOPIC IMAGE OF IMPLANT #1, WHERE A IS THE FEMORAL HEAD CUT IN HALF, B IS THE BODY, C IS THE COMPRESSION NUT, D ARE THE TWO MATING FRACTURE SURFACES, E IS THE POLYETHYLENE ACETABULAR LINER, F IS THE FEMORAL STEM

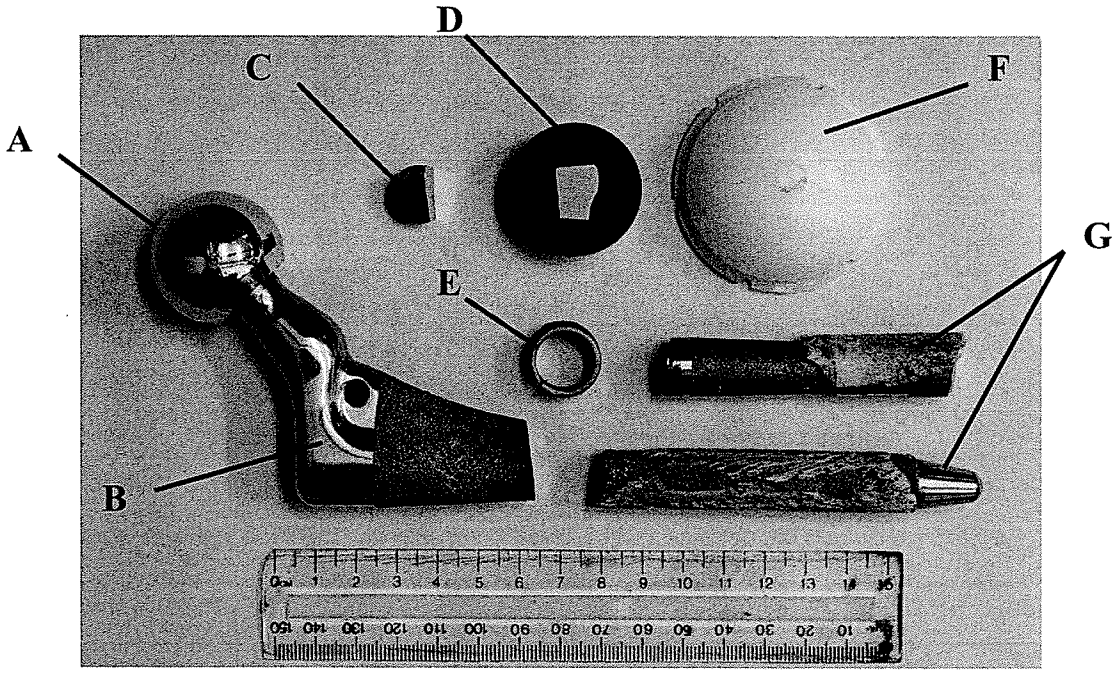

FIGURE 10: MACROSCOPIC IMAGE OF IMPLANT #2, WHERE A IS THE FEMORAL HEAD, B IS THE BODY, C IS THE FRACTURE SURFACE WITH A SMALL PORTION CUT OFF, D IS A MOUNTED AND POLISHED PORTION OF THE FRACTURE SURFACE, E IS PART OF THE BODY THAT WAS CUT OFF FROM AROUND THE FRACTURE SURFACE, F IS THE POLYETHYLENE ACETABULAR LINER, G IS THE FEMORAL STEM

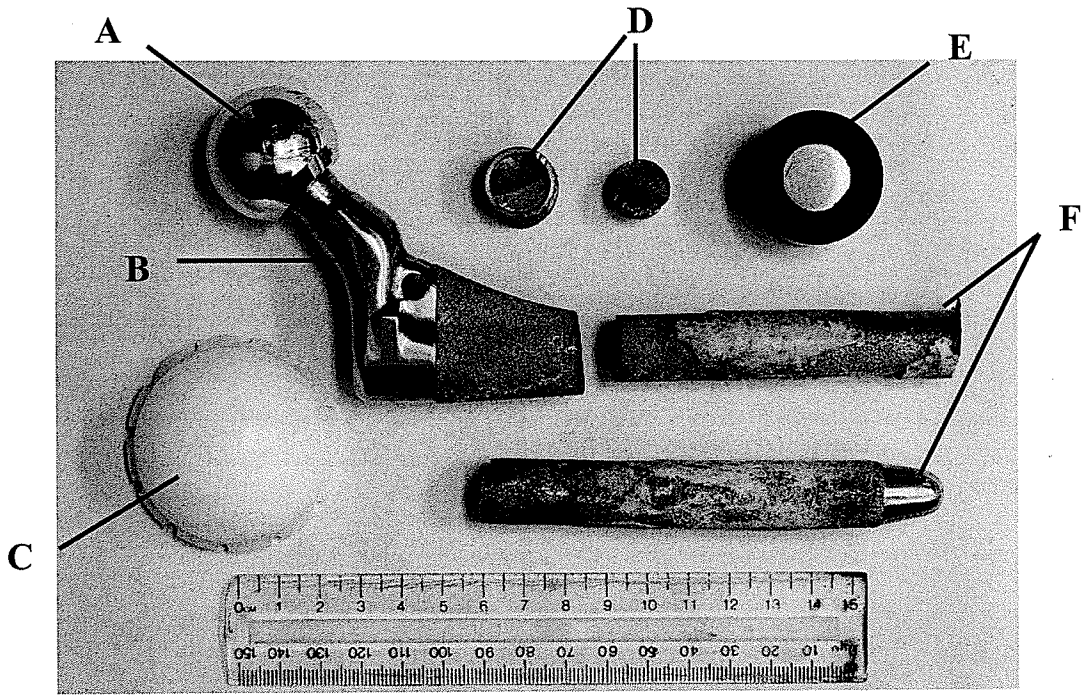

FIGURE 11: MACROSCOPIC IMAGE OF IMPLANT #3, WHERE A IS THE FEMORAL HEAD, B IS THE BODY, C IS THE POLYETHYLENE ACETABULAR LINER, D ARE THE TWO MATING FRACTURE SURFACES, E IS A MOUNTED AND POLISHED SAMPLE OF THE STEM, F IS THE FEMORAL STEM

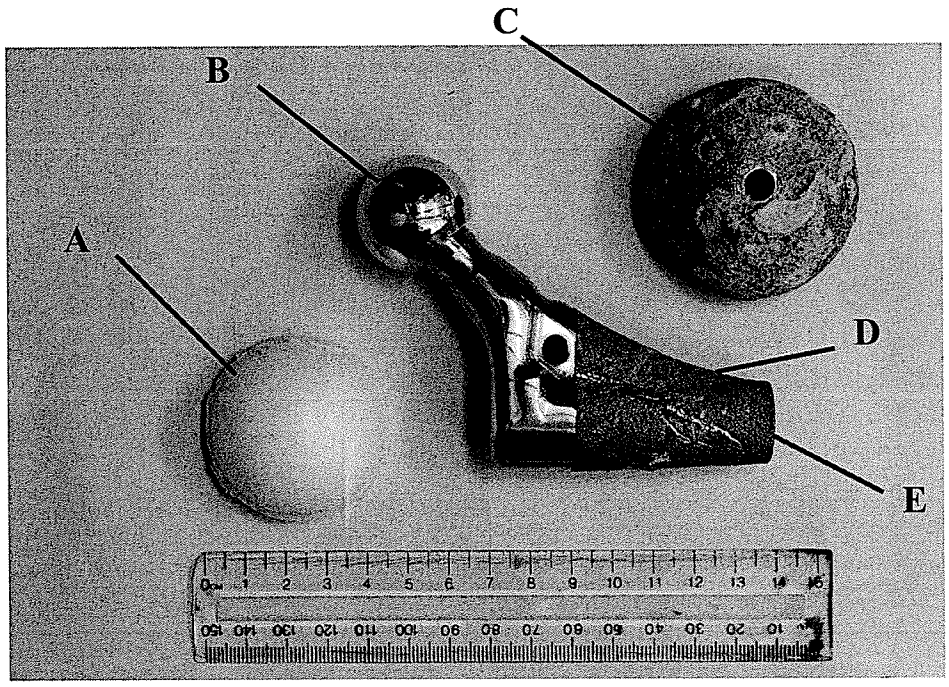

FIGURE 12: MACROSCOPIC IMAGE OF IMPLANT #4, WHERE A IS THE POLYETHYLENE ACETABULAR LINER, B IS THE FEMORAL HEAD, C IS THE ACETABULAR CUP, D IS THE BODY, E IS THE LOCATION OF FRACTURE

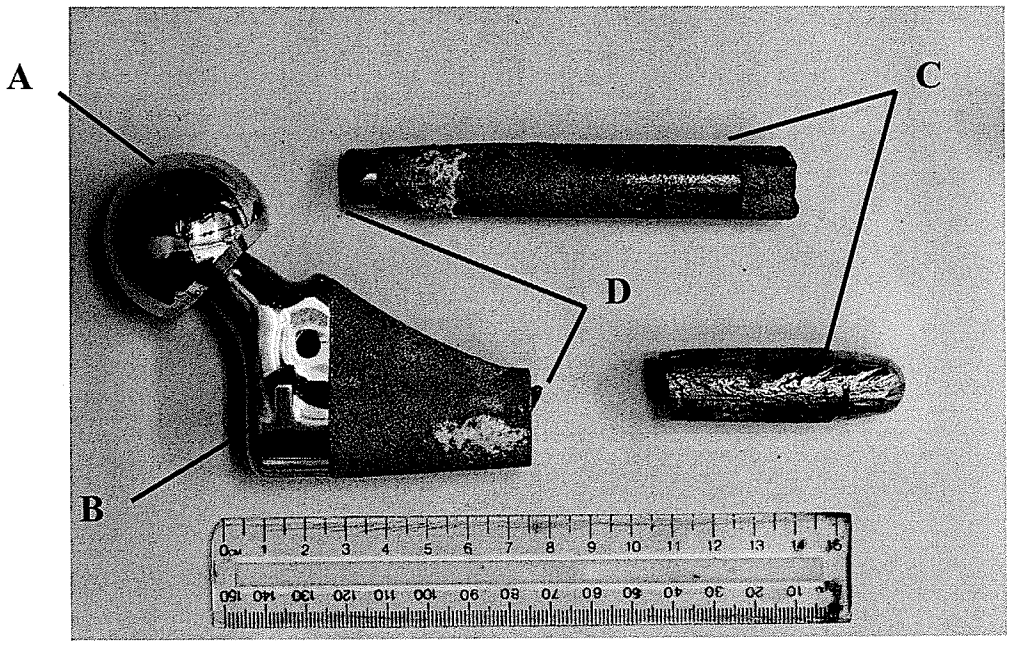

FIGURE 13: MACROSCOPIC IMAGE OF IMPLANT #5, WHERE A IS THE FEMORAL HEAD, B IS THE BODY, C IS THE FEMORAL STEM, D ARE THE TWO MATING FRACTURE SURFACES

All components received from the UMJRG are included in these images. The lower part of the stems seen in Figures 9-13 had been cut during removal from the patient by the surgeon. Other parts that have been cut or mounted occurred during analysis of the implants.

There were four major methods of analysis that were utilized for this study. These include microscopic analysis of the modular Ti-6Al-4V hip stem, macroscopic analysis of the modular hip system and the bone ingrowth of the patient, and finite element analysis and mechanical testing of the modular hip implant. Each of these will be described in the following sections.

3.1 Microscopic Analysis of the Modular Hip Stem

The first stage of analysis was to closely examine the modular Ti-6Al-4V hip stems under a microscope to determine if corrosion, major material defects, stress corrosion cracking, or fatigue contributed to failure. First, the two mating fracture surfaces were cut off with a cutting wheel and analyzed separately under a Nikon SMZ800 optical microscope and SEM. The fractured surfaces were analyzed in detail and methods of implant failure were determined from this. The interface at the modular junction was also examined for evidence of mechanisms contributing to failure, such as fretting, crevice corrosion, and pitting.

A sample of the stem was then cut off with a cut-off wheel and mounted in Bakelite. Each sample was polished on 280, 320, 400, and 600 silicon carbide paper and then with 6 micron and 1 micron diamond suspension in preparation for microscopic inspection. Each mounted sample was etched for 5-60 seconds using a solution of 2 mL of hydrofluoric acid, 10 mL of nitric acid, and 88 mL of water [24]. This allowed the grain boundaries in the material to become visible under the microscope. Microstructure was examined under a Zeiss Axiovert 25 CA Inverted Reflected-Light Microscope, and three-dimensional images at a higher magnification and chemical analysis using Energy-Dispersive X-Ray Spectroscopy (EDS) were obtained from a Jeol JSM-5900LV Scanning Electron Microscope (SEM). EDS is utilized for chemical analysis on the SEM, where the electron beam of the SEM scans the surface of the material and causes the sample to emit x-rays. These x-rays are measured in the SEM to determine their numbers and energies, which indicate elements that are present and their relative amount in the sample

being analyzed [25]. EDS was done to determine if there were any defects or impurities in the implant alloy.

3.2 Macroscopic Analysis of the Modular Hip System and the Bone Ingrowth of the Patient

Macroscopic analysis involved several different methods. First, the two mating fracture surfaces of the hip stem were macroscopically studied to determine if fatigue was a mechanism of failure. Characteristics including point of crack initiation, beachmarks, area of slow fatigue and rapid fracture, and amount of surface damage were examined.

Second, stem fixation of the five patients was examined to determine its contribution to failure. Bony ingrowth was examined by using patient radiographs and by visual inspection. Patient radiographs of the implanted modular Ti-6Al-4V hip implant were closely studied and several factors, including stem fixation, the presence of proximal bone and osseointegration, and the presence of proximal bone across the modular junction were evaluated. Proximal bone was investigated to determine if the body component was supported properly in vivo, which could prevent fatigue failure at the modular junction. Bony ingrowth was defined as "yes" if there were spot welds present or if there was no evidence of subsidence, as "probable" if there were no spot welds present, but cortical bone was intimate to the stem and no radiolucent lines were present, and as "no" if radiolucent lines were present and/or evidence of subsidence. If bone was present at the medial and lateral part of the body, it was determined if there was less than or greater than 50% present comparing to a healthy femur.

Visual inspection of the body and stem component of the modular hip implant was also done to confirm the results obtained from patient radiographs in determining the presence of any bony ingrowth into the textured surface of the implant. If osseointegration was accomplished in vivo, bone will likely still be present on the implant even after removal from the patient. Patient factors that were considered during stem analysis included weight, gender, age, and patient activity.

In addition to examining for stem fixation, the operative reports of the modular implant insertion surgery were reviewed for mention if a bone graft on the femur was used during the operative procedure.

3.3 Finite Element Analysis of the Modular Hip Implant

The modular Ti-6Al-4V hip implant was three-dimensionally modeled using Pro-Engineer Wildfire 2.0 (© 2004). Using the Pro-Mechanica component of the program, specific parameters were added to the modular Ti-6Al-4V model to simulate motion in vivo. These parameters will be discussed later. This simulation provided a stress distribution throughout the implant and located where the highest point of stress is during load application.

In addition to this, a medial support was added to the three-dimensional model for comparison of internal stresses in the implant. This medial support was meant to simulate a medial bone graft.

3.4 Mechanical Testing of the Modular Hip Stem

Since Ti-6Al-4V modular hip stems are expensive, fatigue tests were first conducted on 6061-T651 aluminum alloy simulated stems. Tensile properties were obtained using a Baldwin Universal Testing System on specimens machined to ASTM Standard E8-04 [26]. For the Ti-6Al-4V alloy, a distal end of a modular stem was utilized for tensile testing since the stem had to be shortened to fit into the compression cage for fatigue testing. Hardness tests were performed using a Versitron AT130-R Rockwell Hardness Testing System. The Rockwell A scale, diamond brale indenter with a 60 kg load was employed on the tensile testing specimen and each of the failed implants being studied. These tensile and hardness tests were done primarily for comparison with published typical values and to ensure that none of the fractured stems were deficient with respect to mechanical properties.

Fatigue testing was done to simulate patient motion and to determine if the implant would fracture and fail by the same mechanism at the same modular junction as in vivo. To accomplish the fatigue testing of the implants in this study, an Instron 8502 fatigue machine was used. Since the grips on the machine work best in tension, a cage was constructed to house the implant and accomplish compression forces. Photographs of this compression cage can be seen in Figure 14.

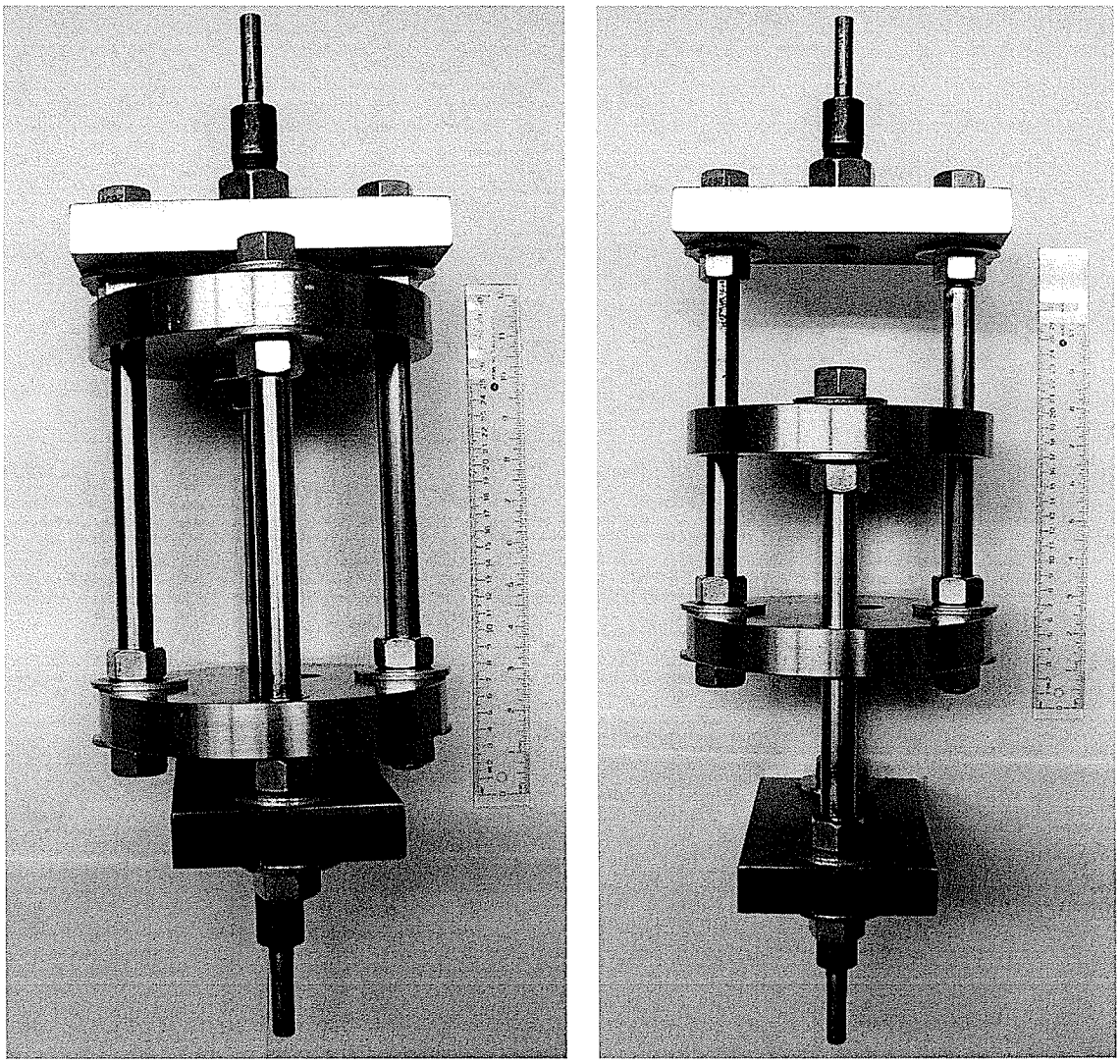

(A) (B)

FIGURE 14: COMPRESSION CAGE USED FOR FATIGUE TESTING, (A) OPEN, (B) CLOSED

Figure 14 shows that the compression cage is comprised of two circular plates, two rectangular plates, and four rods. At each end of the compression cage are grip sections, a rod that threads into the rectangular plate at one end and fits into the grips of the tensile fatigue testing machine at the other. Figure 14(A) shows the cage with a maximum space extended between the circular plates. Figure 14(B) shows what happens when the bottom grip is pulled downwards. It can be seen that even though a tensile force

was used, the circular plates come closer together, creating compressive forces on the implant that was housed inside. The dimensioned drawings of the compression cage assembly and its components are included in Appendix A. In each picture, a 30 cm ruler was used to show a scale.

Initially, stems were machined using aluminum (Al) 6061 alloy ($\rho = 2.70$ g/cm^3), which is very inexpensive in comparison to a modular Ti-6Al-4V hip implant and is easy to machine. This material was also used to test different loads in order to obtain a ratio of maximum fatigue load to its yield strength. Once a ratio was obtained, a load was found using the yield strength of Ti-6Al-4V, and the actual modular Ti-6Al-4V stem was fatigued at this load. The properties of the 6061 aluminum alloy can be seen in Table 5.

TABLE 5: ASM MECHANICAL PROPERTIES OF THE 6061 AL ALLOY [27]

Temper	**Modulus of Elasticity, GPa (psi)**	**Tensile Strength, MPa (ksi)**	**Yield Strength, MPa (ksi)**	**Elongation, %**		**Shear Strength, MPa (ksi)**
				1.6mm (1/14 in) thick specimen	**13mm (1/2 in) dia. specimen**	
T651	68.9 (9.99×10^6)	310 (45)	276 (40)	12	17	207 (30)

The temper/heat treatment of the aluminum alloy used was T651, which means that the alloy was solution heat treated, artificially aged, and stress relieved by stretching [27]. By comparing Table 5 with Table 2, it can be seen that the tensile strength and yield strength are approximately a third of that of Ti-6Al-4V. Also, the modulus of elasticity for the 6061 aluminum alloy is 68.9 GPa, which is significantly less than 120 GPa for Ti-6Al-4V.

The 6061 aluminum alloy stem was machined to have the same taper as the Ti-6Al-4V stem to ensure the same fit into the body component. The bottom of the 6061 aluminum alloy stem is threaded with a 0.95 cm (3/8 in) hole that is 1.27 cm (1/2 in) deep. This is to allow fixation with a bolt to the compression cage, simulating distal fixation in a patient's femur. However, since the fracture occurs at the modular junction, the length chosen for the aluminum alloy stem is considerably shorter than the Ti-6Al-4V stem to minimize the length necessary for the rods of the compression cage. Dimensional drawings of the 6061 aluminum alloy stem are provided in Appendix B. A photograph of this stem is shown in Figure 15.

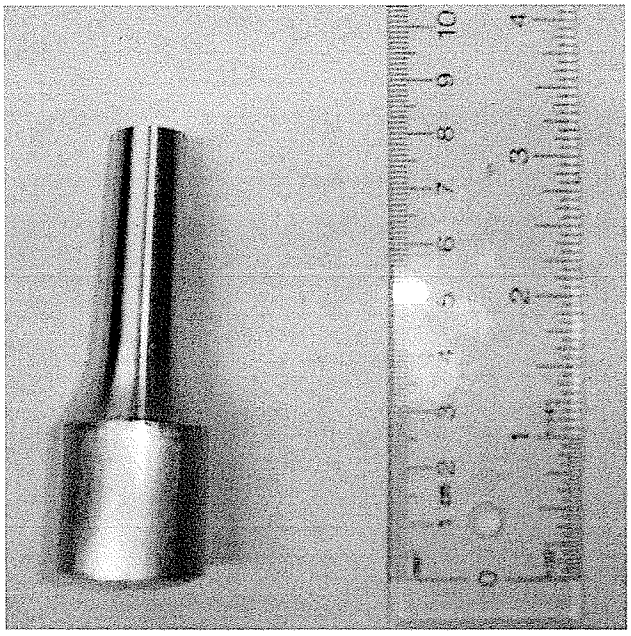

FIGURE 15: THE 6061 AL ALLOY STEM USED FOR FATIGUE TESTING

An image of the 6061 aluminum alloy stem assembled with the body component in the compression cage can be seen in Figure 16.

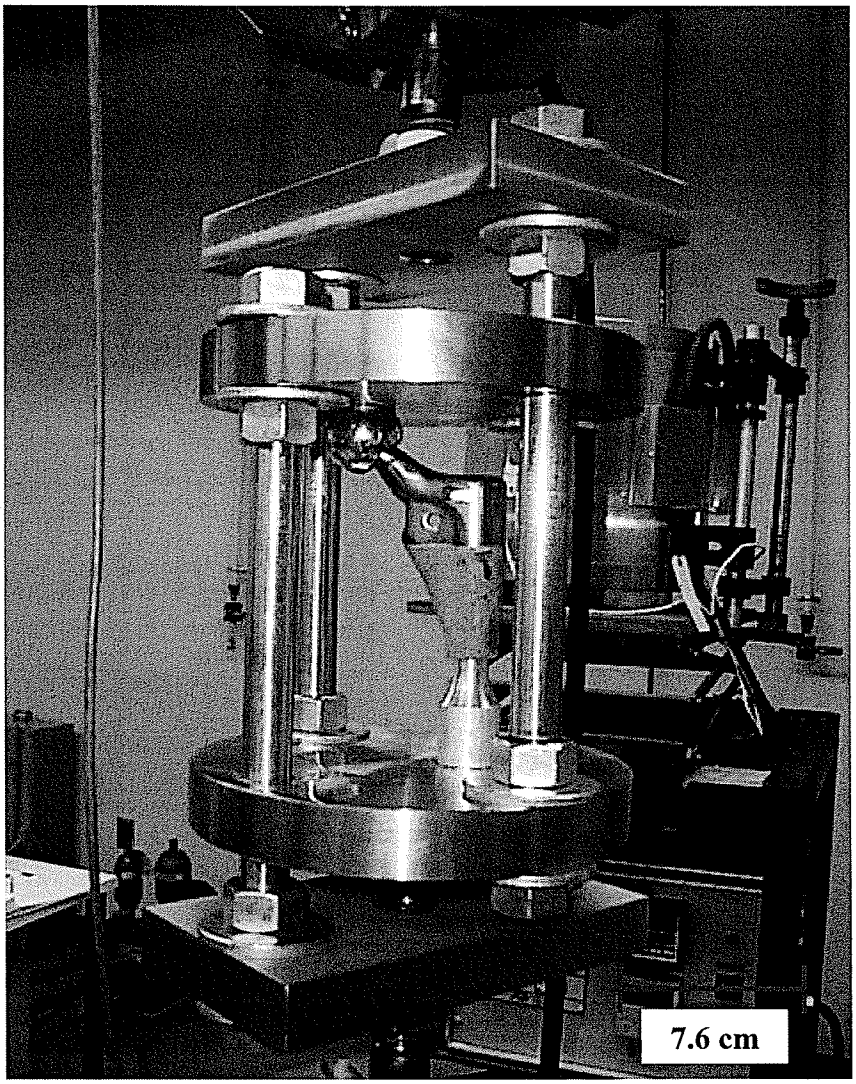

FIGURE 16: THE 6061 AL ALLOY STEM SET UP IN COMPRESSION CAGE

Once the 6061 aluminum alloy stems were fatigued and a load was obtained to test the Ti-6Al-4V stems, the latter were cut to approximately 10 cm (4 in) to ensure that the hip assembly would fit into the compression cage. Since the diameter of this stem is only approximately 1.3 cm (0.5 in), the stem could not be fixed to the compression cage with a bolt, as the 6061 aluminum alloy stem was. Therefore, a 5 cm (2 in) diameter holder was made from the 6061 aluminum alloy. The stem was fixated in the holder using

two bolts, with the bottom of the holder fixed to the bottom plate of the compression cage. This arrangement is shown in Figure 17.

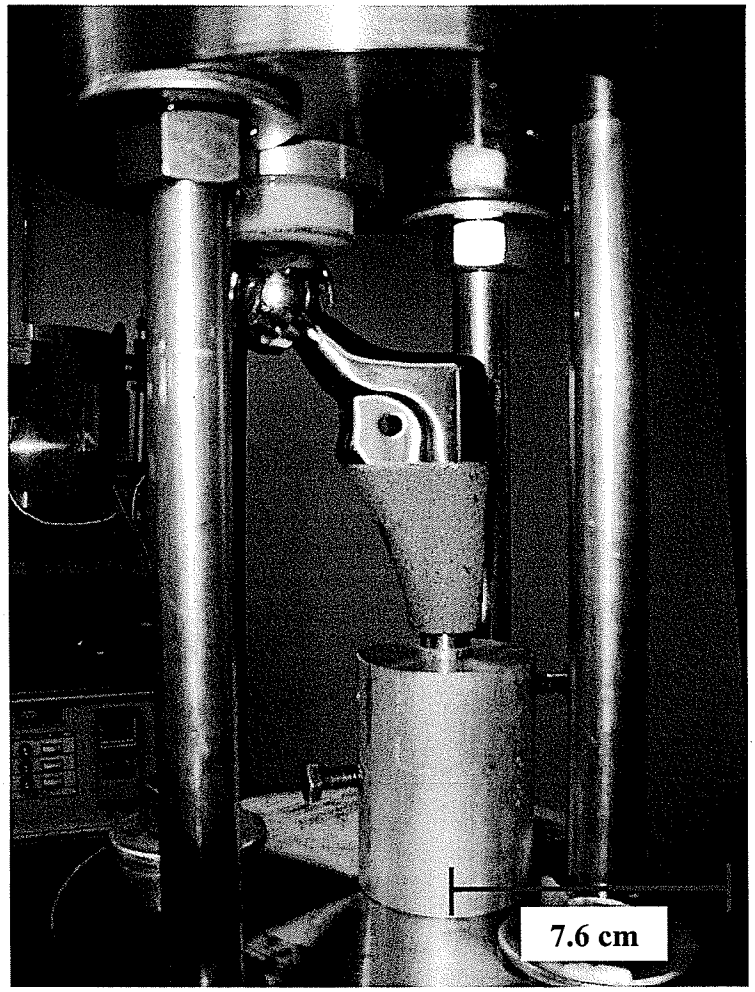

FIGURE 17: TI-6AL-4V STEM IN HOLDER SET UP IN COMPRESSION CAGE

Following the testing of the 6061 Al alloy stems, the rods and bearings of the compression cage were changed to ensure that wear of the bearings would not affect the Ti-6Al-4V fatigue tests. The stainless steel rods were lengthened by approximately 7.5 cm (3 in) to accommodate the stem and stem holder. Fatigue testing was done on the Ti-

6Al-4V stems with the intent of replicating the point of crack initiation and failure in vivo.

It should be noted that in the fatigue test results that are reported in the following chapter, the load to the femoral head was applied axially to the femoral stem as illustrated in Figure 17. In actuality, the femur is at an angle of approximately 10° to the axis of loading [28]. However, this value varies from person to person and is influenced by the individual's gait as well as muscular forces. Therefore, for simplicity, a vertical force was used on the femoral head.

CHAPTER 4

EXPERIMENTAL RESULTS AND DISCUSSION

In this section, the results of each method of analysis are recorded and discussed. These include results from the microscopic analysis of the modular Ti-6Al-4V hip stem, macroscopic analysis of the modular hip system and bone ingrowth of the patient, the finite element analysis of the modular hip implant, and the fatigue and tensile testing of the 6061 aluminum alloy and Ti-6Al-4V hip stems. After these have been covered, there will be further discussion on other possible contributors to stem failure.

Profiles for the recipients of the modular hip implants studied in this investigation were considered during analysis. Factors considered include age, height, weight, and activity level of the patient at the time of implant fracture, as well as the duration of implantation and which side of the body the implant was removed from. Table 6 summarizes the results that were found.

TABLE 6: SUMMARY OF RESULTS OF PATIENT AND IMPLANT FACTORS AT THE TIME OF IMPLANT FRACTURE

	Age	Height	Weight	Duration of Implantation	Side of the Body	Activity Level
Implant #1	81 years	182.9 cm (72 in)	97.5 kg (215 lbs)	4.13 years	Left	Not Active
Implant #2	65 years	160.0 cm (63 in)	81.2 kg (179 lbs)	4.30 years	Left	N/A
Implant #3	61 years	188.0 cm (74 in)	98.9 kg (218 lbs)	3.82 years	Left	Not Active
Implant #4	73 years	N/A	71.7 kg (158 lbs)	4.86 years	Left	N/A
Implant #5	62 years	188.0 cm (74 in)	90.7 kg (200 lbs)	3.04 years	Left	Not Active
Average	**68.4 years**	**179.7 cm (70.8 in)**	**88 kg (194 lbs)**	**4.03 years**	**Left**	**Not Active**

By looking at Table 6, it can be seen that the average age of the patients is 68 years old, the average height is 180 cm (71 in), and the average mass is 88 kg (194 lbs). Therefore, patients were not particularly obese. Where the information was available, patients were deemed to be not active by their surgeons. Despite these factors, the modular hip implant was in vivo for approximately 4 years on average before fracture. Although all implants examined were from the left side of the body, this would not contribute to failure since the load should be equal over the left and right side of the body.

4.1 Microscopic Analysis of the Modular Hip Stem

As stated in the previous section, the first stage of analysis was to closely examine the modular Ti-6Al-4V hip stems under a microscope to determine if corrosion, major material defects, stress corrosion cracking, or fatigue contributed to failure. Fatigue characteristics that were searched for was a slow fatigue zone (stage 2 of fatigue), a transition zone (between stages 2 and 3), a rapid fracture zone (stage 3 of fatigue), and curved beachmarks on the fracture surface. Microscopic analysis allowed for study of the finer details of the fracture surface.

The fracture surfaces were studied carefully for the point of crack initiation, macroscopic striations, and any other surface features. These images that were captured on the optical microscope can be seen in Figures 18-21.

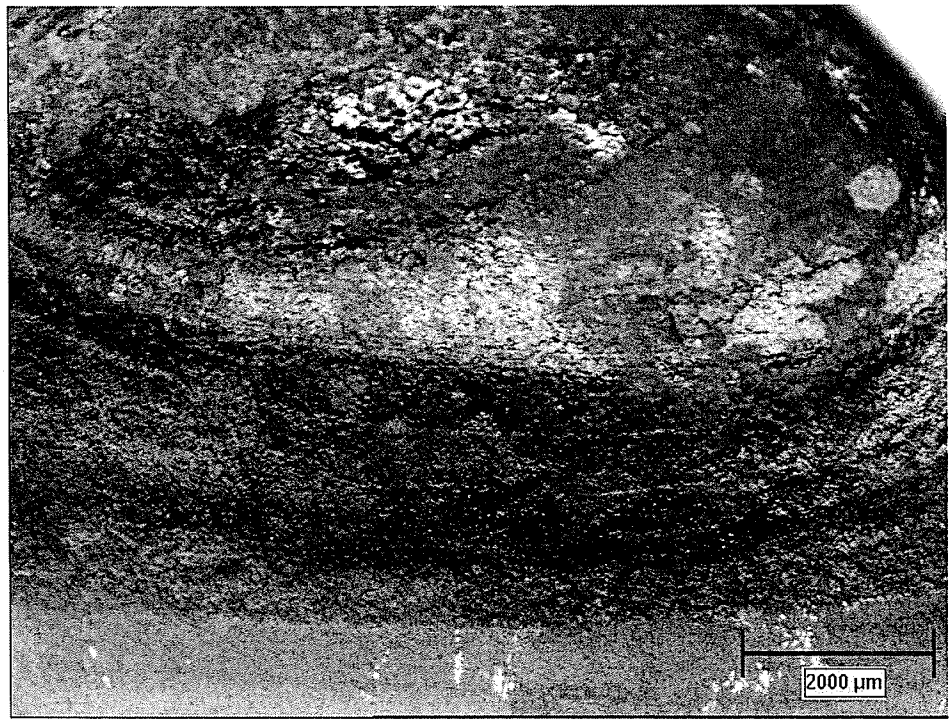

FIGURE 18: FRACTURE SURFACE OF IMPLANT #1 TAKEN AT 10X, SLOW FATIGUE AND TRANSITION ZONES, CRACK INITIATION IS TOWARDS THE TOP OF THE SECTION

From Figure 18, the slow fatigue and transition zone of the fracture surface of implant #1 can be seen. Crack initiation occurs towards the top of the section. The slow fatigue area occurs over a longer duration of time than the rapid fracture area since the crack tip propagates very slowly. Surface damage is likely to occur in this region since the mating surface remains in contact with it despite having separated by crack propagation. Surface damage can be seen in Figure 18 where there are lighter, brighter spots. The transition zone is where the crack tip will start to propagate faster and lead to the rapid fracture zone. When the rapid fracture area appears, beachmarks are present. This is because the rate of crack propagation is increasing. The slow fatigue area is darker in appearance than the rapid fracture area due to surface corrosion from exposure to extracellular fluid that enters the crevice during fatigue. When extracellular fluid enters the crevice, the pH in the crevice decreases. This creates a more acidic environment for the fracture surface.

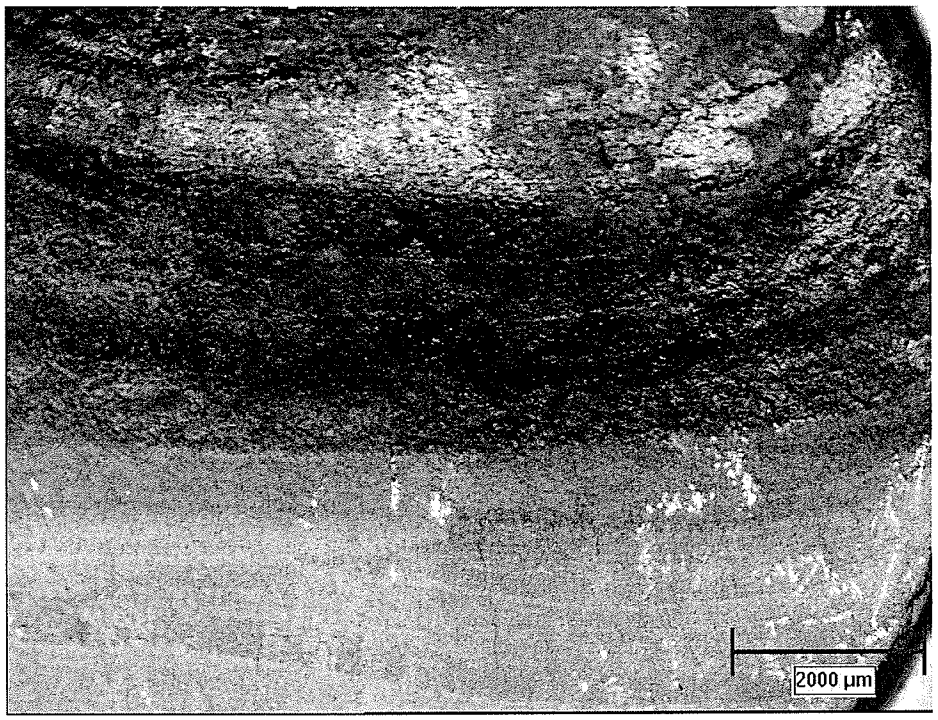

FIGURE 19: FRACTURE SURFACE OF IMPLANT #1 TAKEN AT 10X, TRANSITION ZONE BETWEEN SLOW FATIGUE AND RAPID FRACTURE ZONES, CRACK INITIATION IS TOWARDS THE TOP OF THE SECTION

Figure 19 shows the transition zone between the slow fatigue area and the rapid fracture area of implant #1. Crack initiation occurs towards the top of the section. It can be seen that the rapid fracture zone is lighter in comparison to the slow fracture zone. This is likely because when rapid fracture occurs, the surface is not attacked by extracellular fluid in a crevice and surgery to remove the implant occurs soon after fracture. Beachmarks are also evident in this area. The curvature of the beachmarks indicates the location of crack initiation of the implant, since they expand away from that point. It is clear from Figures 18 and 19 that crack initiation occurred in the upper portions of these images, which is the lateral side of the stem at the modular junction. However, due to the fracture surface damage of this implant, the exact point cannot be indicated.

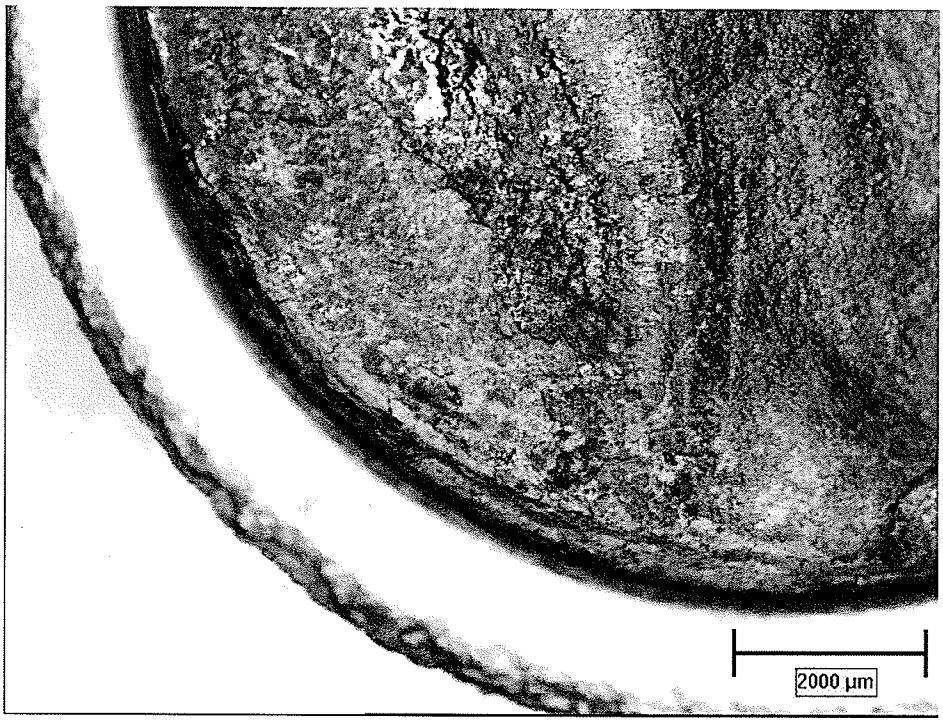

FIGURE 20: FRACTURE SURFACE OF IMPLANT #1 TAKEN AT 10X, DAMAGED SLOW FATIGUE ZONE, CRACK INITIATION IS TOWARDS THE LEFT OF THE SECTION

Figure 20 shows the damaged area of the slow fatigue zone of implant #1. Crack initiation occurs towards the left of the section. It is clear that the exact point of crack initiation cannot be determined since no beachmarks are visible, although an approximate point can be determined on the lateral side of the modular stem. This area of the fracture surface appears to be covered in a layer of unknown material. This was investigated further using the SEM.

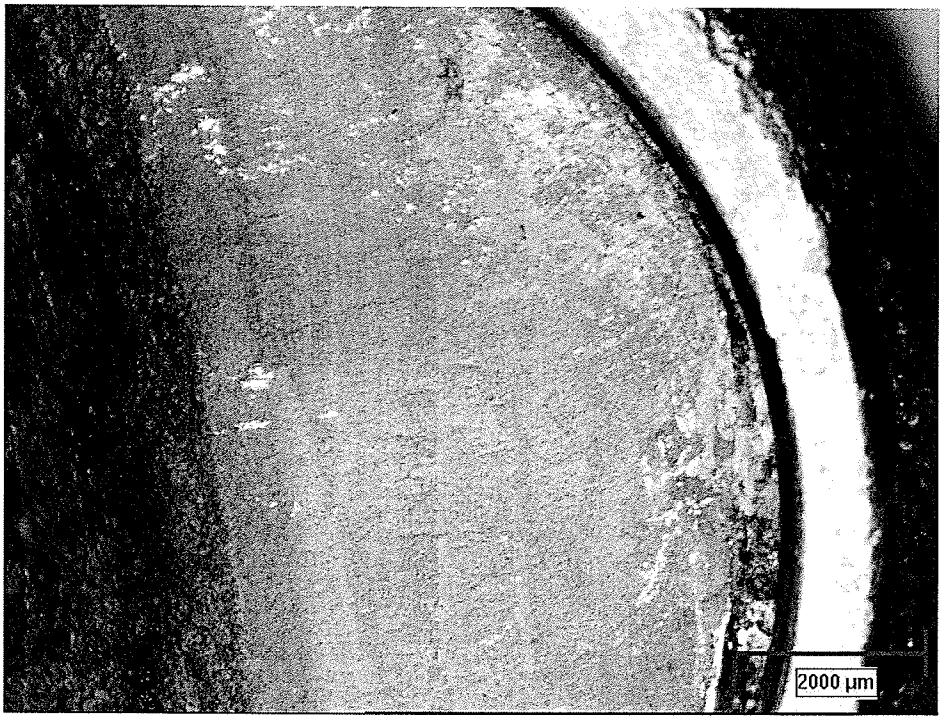

FIGURE 21: FRACTURE SURFACE OF IMPLANT #1 TAKEN AT 10X, RAPID FRACTURE ZONE, CRACK INITIATION IS TOWARDS THE LEFT OF THE SECTION

Figure 21 shows the rapid fracture zone of implant #1. Crack initiation occurs towards the left of the section. Beachmarks are clearly visible in this area. Brighter spots on the surface indicate damage.

FIGURE 22: FRACTURE SURFACE OF IMPLANT #2 TAKEN AT 10X, CRACK INITIATION IS TOWARDS THE RIGHT OF THE SECTION

Figure 22 shows the fracture surface of implant #2. The slow fatigue zone, the transition zone, and the rapid fracture zone can be seen in this picture. Crack initiation occurs towards the right of the section. The slow fatigue area for implant #2 is darker in appearance due to crevice corrosion from extracellular fluid. It also appears to be covered in a layer of unknown material, which will undergo investigation using the SEM. The beachmarks on the rapid fracture area are very clear and their curvature confirms that the point of crack initiation occurred on the lateral side of the stem in the slow fatigue zone.

FIGURE 23: FRACTURE SURFACE OF IMPLANT #3 TAKEN AT 10X, DAMAGED SLOW FATIGUE ZONE, CRACK INITIATION IS TOWARDS THE BOTTOM OF THE SECTION

Figure 23 shows the slow fatigue zone of implant #3. Crack initiation occurs towards the bottom of the section. Similar to implant #1 and #2, the surface is darker due to crevice corrosion by extracellular fluid and appears to be covered in a layer of unknown material. The image also displays surface damage that occurred in vivo. Although there seems to be a crack on the surface, which would indicate signs of stress corrosion cracking, closer inspection revealed that this was merely topography created by the fracture. There are no visible beachmarks in this area. Therefore, an exact point of crack initiation cannot be determined solely from this section.

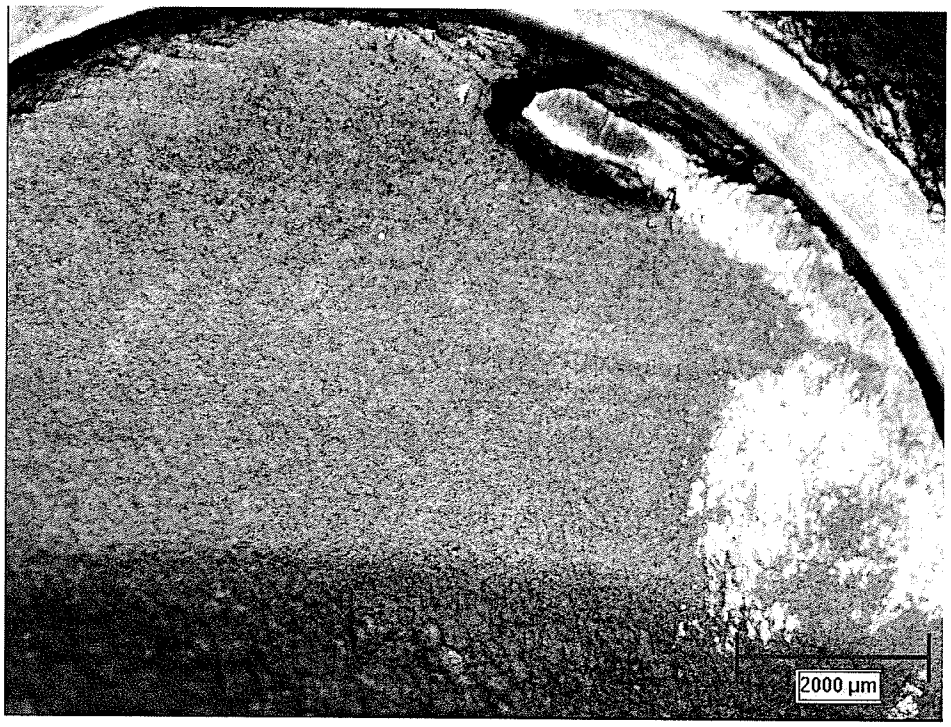

FIGURE 24: FRACTURE SURFACE OF IMPLANT #3 TAKEN AT 10X, TRANSITION AND RAPID FRACTURE ZONES, CRACK INITIATION IS TOWARDS THE BOTTOM OF THE SECTION

Figure 24 shows the transition zone and the rapid fracture zone of implant #3. Crack initiation occurs towards the bottom of the section. The beachmarks that are present are visible, but not as pronounced as implant #1 or implant #2. Again, the curvature of the beachmarks indicates that crack initiation occurred on the lateral side of the stem. Surface damage due to the mating fracture surface can be seen on the right side of the image. It is also clear to see that the final point of fracture removed a portion of the surface.

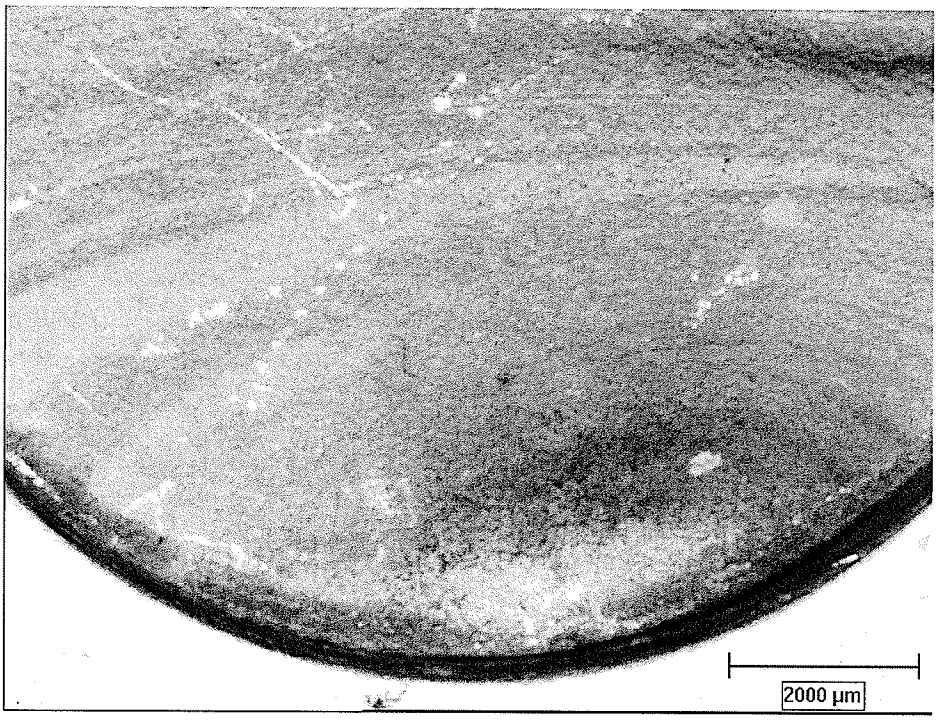

FIGURE 25: FRACTURE SURFACE OF IMPLANT #4 TAKEN AT 10X, SLOW FATIGUE AND RAPID FRACTURE ZONES, CRACK INITIATION IS TOWARDS THE BOTTOM OF THE SECTION

Figure 25 shows the slow fatigue zone and the rapid fracture zone for implant #4. Crack initiation occurs towards the bottom of the section. Unlike the other implants examined to this point, implant #4 shows a very small slow fatigue zone in comparison to implants #1, #2, and #3. Therefore, it is clear that rapid crack propagation and stem fracture occurred soon after crack initiation in the stem. This is somewhat unusual since a large rapid fracture area is typical of high loads. However, Table 6 shows that this implant was taken from the lightest person in the study (≈ 72 kg). Due to the rapid failure of the implant, this also means that corrosion in the crevice from extracellular fluid did not attack the slow fatigue zone for as long as the other implants that were examined. Since this area was not corroded as heavily, the slow fatigue zone is not significantly darker in appearance than the rapid fracture zone. Therefore, the transition zone between

the slow fatigue area and the rapid fracture area is difficult to see. Beachmarks are evident and their curvature clearly indicates that crack initiation occurred on the lateral side of the stem, which is located at the bottom of Figure 25. Minor damage can be seen due to the mating fracture surface.

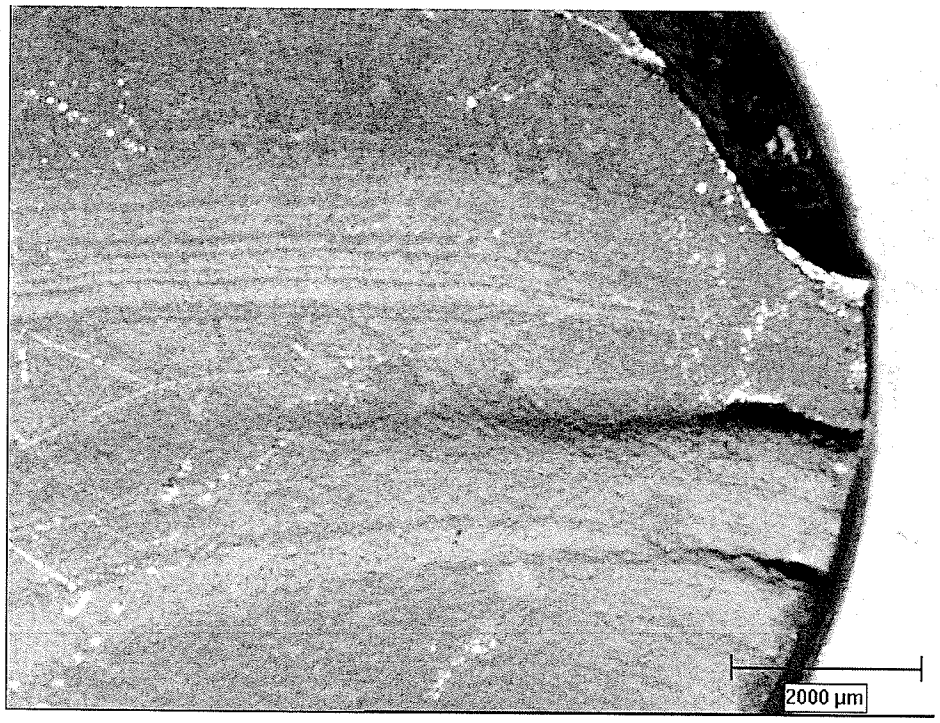

FIGURE 26: FRACTURE SURFACE OF IMPLANT #4 TAKEN AT 10X, RAPID FRACTURE ZONE, CRACK INITIATION IS TOWARDS THE BOTTOM OF THE SECTION

Figure 26 shows the rapid fracture zone of implant #4. Crack initiation occurs towards the bottom of the section. Beachmarks are clearly visible and it appears as though the last point of fracture removed a portion of the surface. This can be seen in the top right corner of the image. There also appears to be two cracks in the surface, which can be seen on the right edge of the stem. However, with closer inspection, these are both simply topography created by the rapid fracture. Minor surface damage can be seen.

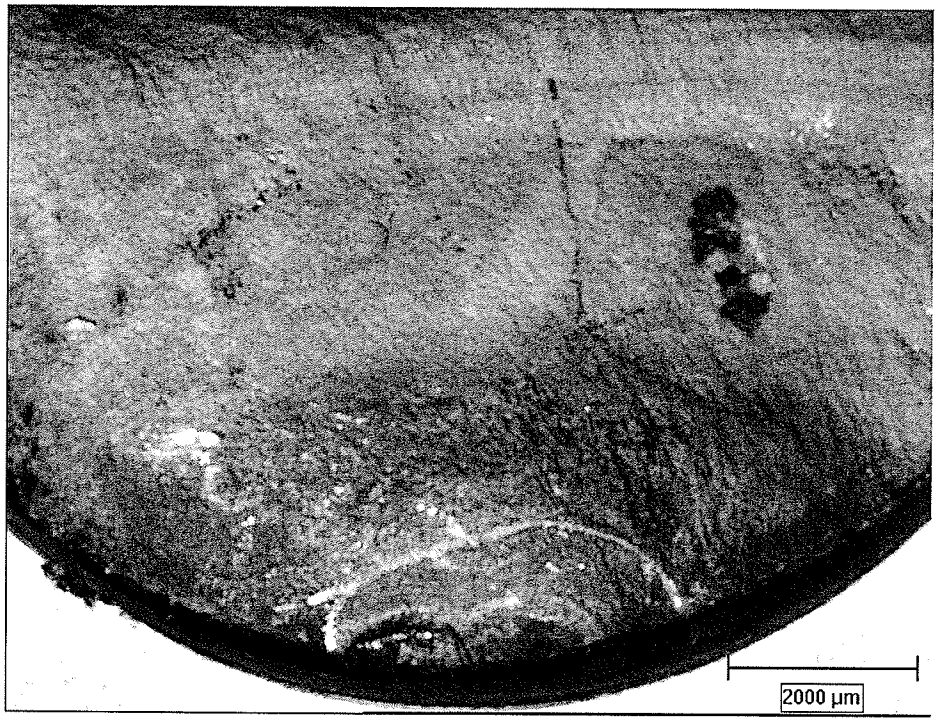

FIGURE 27: FRACTURE SURFACE OF IMPLANT #5 TAKEN AT 10X, SLOW FATIGUE AND TRANSITION ZONES, CRACK INITIATION IS TOWARDS THE BOTTOM OF THE SECTION

Figure 27 shows the slow fatigue zone and transition zone of implant #5. Crack initiation occurs towards the bottom of the section. Similar to implant #4, the slow fatigue area is very small in comparison to implants #1, #2, and #3. This means that in this case as well, rapid crack propagation and stem fracture occurred soon after crack initiation. The slow fatigue area is also not much darker in appearance in comparison to the rapid fracture zone due to minimal exposure to crevice corrosion of extracellular fluid in vivo. The transition zone of implant #5 is easier to see than with implant #4. Beachmarks are clear to see and their curvature indicates that crack initiation occurred on the lateral side of the stem. Minor damage can be seen on the fracture surface.

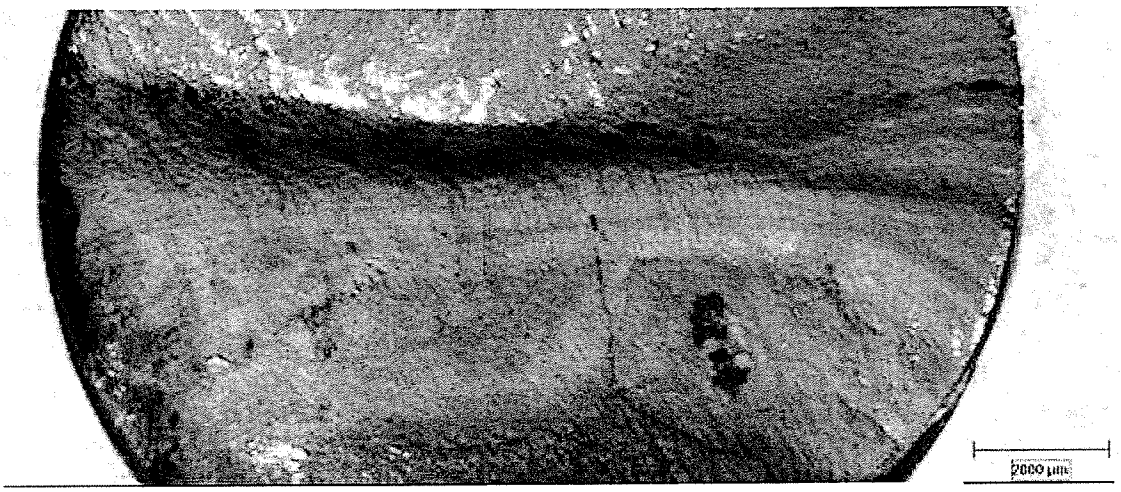

FIGURE 28: FRACTURE SURFACE OF IMPLANT #5 TAKEN AT 10X, RAPID FRACTURE ZONE, CRACK INITATION IS TOWARDS THE BOTTOM OF THE SECTION

Figure 28 shows the rapid fracture zone of implant #5. Crack initiation occurs towards the bottom of the section. Beachmarks in the transition zone are evident. Minor damage can be seen on the fracture surface.

Stereomicroscopic examination of the fracture surfaces of all five implants confirm fatigue failure with crack initiation occurring on the lateral side of the stem.

As mentioned in the previous chapter, a portion of the stem away from the fracture surface was cut off and mounted in Bakelite. This surface was then polished and etched in order to view microstructure and the presence of any inclusions that could contribute to fatigue failure.

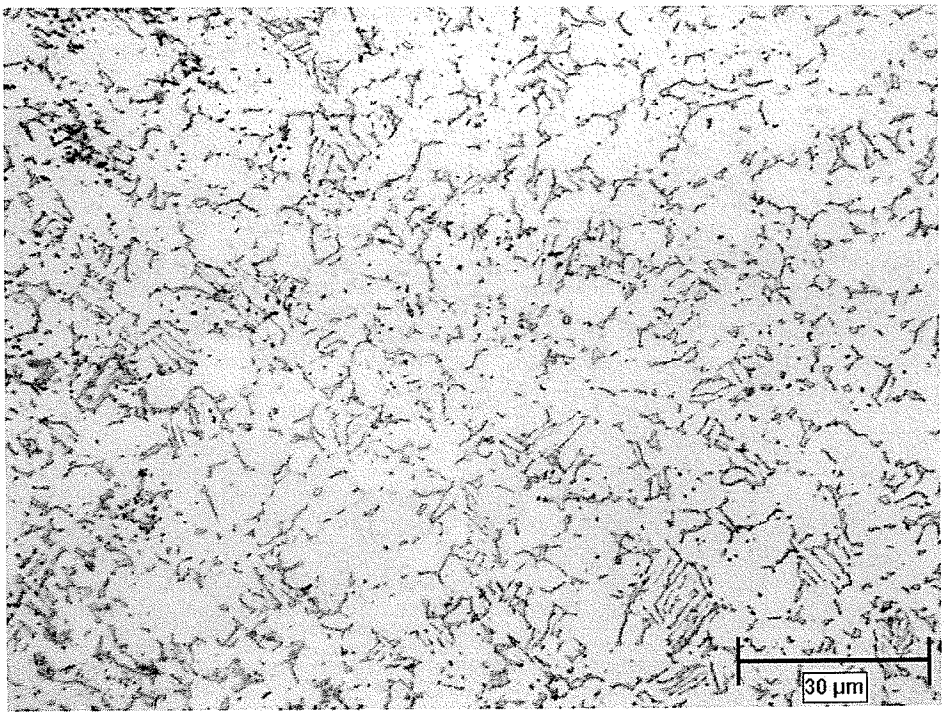

FIGURE 29: CROSS-SECTION SAMPLE OF TI-6AL-4V STEM FROM IMPLANT #3, MOUNTED, POLISHED, AND ETCHED TAKEN AT 1000X

Figure 29 shows a cross-section sample in the transverse plane of the stem from implant #3 that has been mounted, polished, and etched. This sample was etched until there was some bubbling on the surface when immersed in the etching solution, which was approximately 5-10 seconds. This image is representative of all five implants that are being examined in this study. Grain boundaries are mostly visible in Figure 29. Any additional etching to make grain boundaries more visible only caused over-etching to occur. This is a typical microstructure for Ti-6Al-4V alloy and there are no apparent defects or impurities [24].

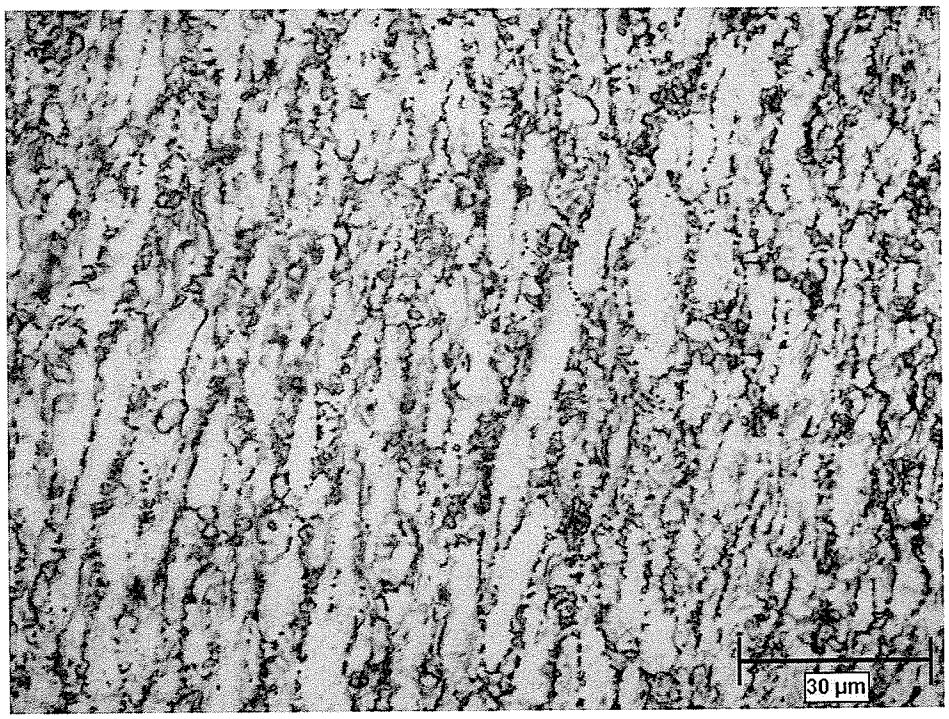

FIGURE 30: AXIAL CROSS-SECTION SAMPLE OF TI-6AL-4V STEM FROM IMPLANT #2, MOUNTED, POLISHED, AND ETCHED TAKEN AT 1000X

Figure 30 shows a vertical cross-section sample in the axial plane of the stem from implant #2 that has been mounted, polished, and etched. This sample was also etched until there was some bubbling on the surface when immersed in the etching solution, which was approximately 5-10 seconds. It can be seen that on a 90° plane difference from Figure 29, the grains appear stretched. These elongated grains mean that the Ti-6Al-4V material was cold-worked in the stem manufacturing process and simply indicate directionality of rolling. In Figure 30, the lighter matrix is α-phase and the darker particles are β-phase. This is also a typical microstructure for Ti-6Al-4V alloys [24].

.

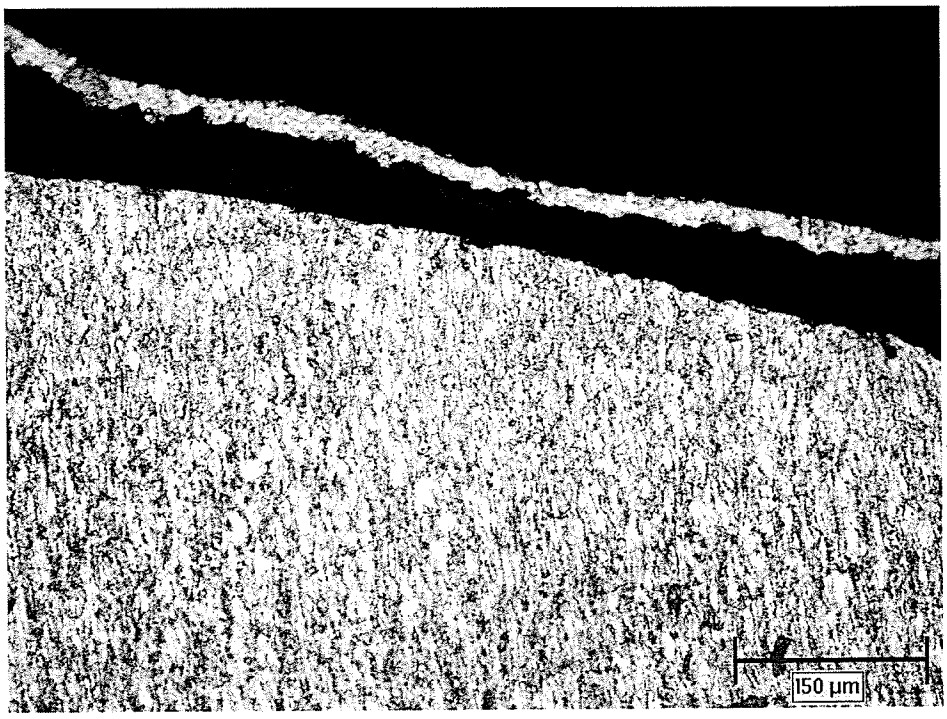

FIGURE 31: AXIAL CROSS-SECTION SAMPLE OF TI-6AL-4V STEM FROM IMPLANT #2, MOUNTED, POLISHED, AND ETCHED TAKEN AT 200X, FRACTURE SURFACE IS ALONG THE TOP OF THE SECTION

Figure 31 shows a vertical cross-section sample in the axial plane of the stem from implant #2 that has been mounted, polished, and etched for approximately 5-10 seconds. It can be seen that there is a thin layer above the stem sample. This appears to be the layer of unknown material that was seen before in the optical microscope pictures. During the high temperature and high pressure of the mounting process in Bakelite, the layer seems to have separated from the fracture surface. This layer was analyzed under the SEM and the rest of the sample was broken out of the Bakelite with the intent to view the fracture surface without the layer.

After optical microscope examination was complete, SEM analysis was done. A semi-quantitative chemical analysis using EDS was done on the fracture surface and

three-dimensional images at a higher magnification were obtained. Images of these can be seen below.

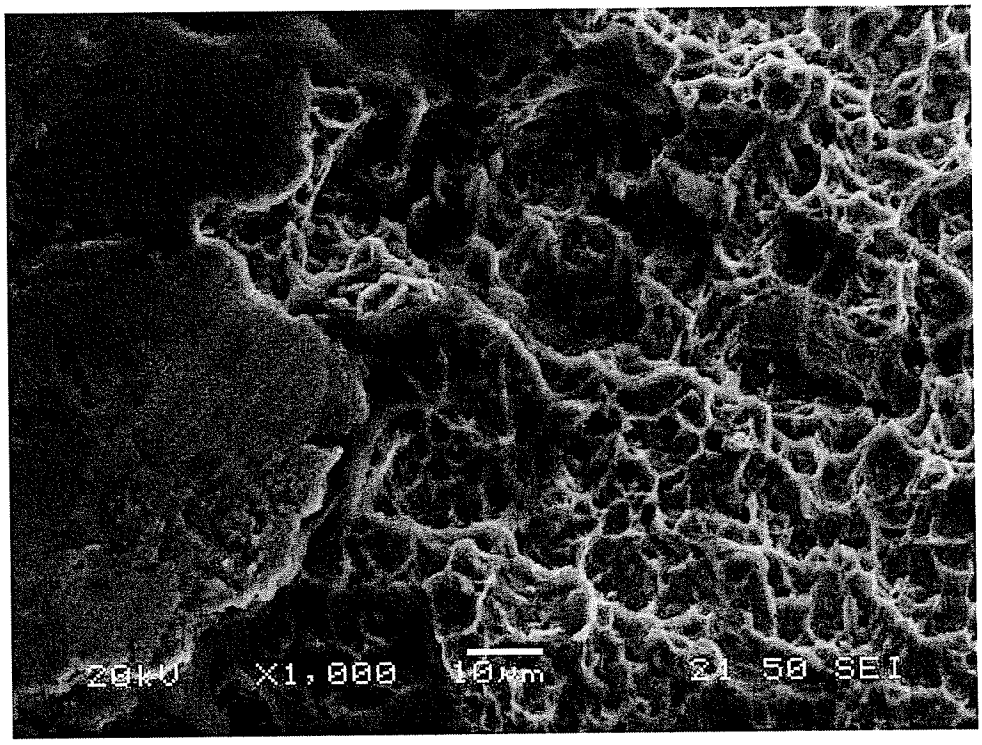

FIGURE 32: SEM IMAGE OF IMPLANT #2, RAPID FRACTURE ZONE TAKEN AT 1000X

Figure 32 shows the rapid fracture zone of implant #2. This image shows that during rapid fracture, the stem broke in a cup-and-cone ductile manner. This was the case for all five fractured implants that were studied. The left side of this image shows a flat smooth area. This is what the damaged area appears to be under a magnification of 1000x. This occurs when the mating proximal fracture surface comes into contact with the distal fracture surface under load, causing flattening of any topography that was created during repeated cycles.

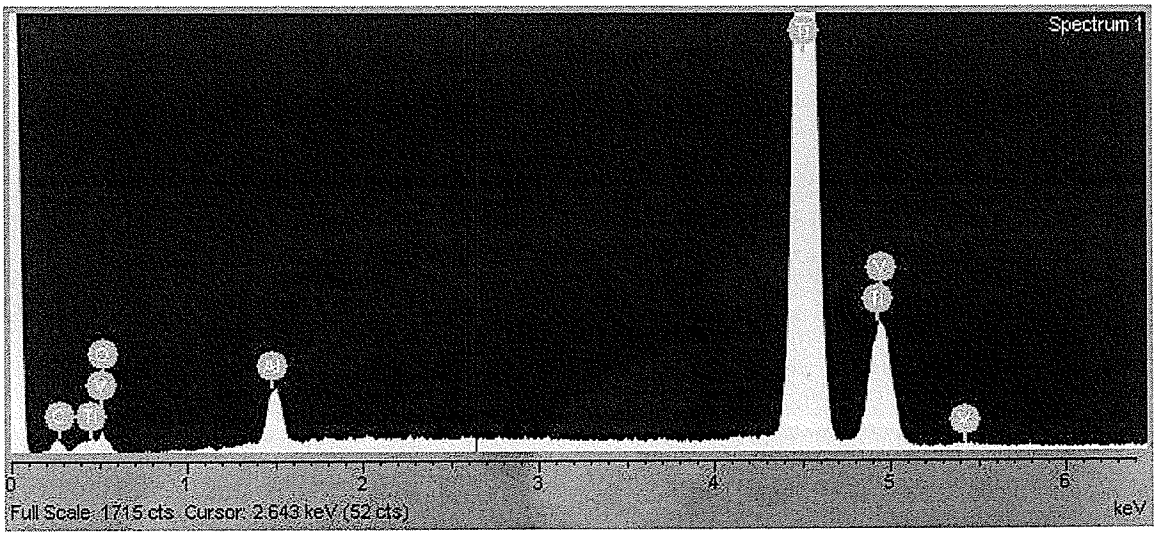

FIGURE 33: CHEMICAL ANALYSIS OF THE FRACTURE SURFACE OF IMPLANT #1 USING EDS ON THE SEM

Figure 33 shows the results of the chemical analysis done on the fracture surface of implant #1 using EDS on the SEM. This analysis confirms the relative presence of titanium, aluminum, and vanadium in the alloy being studied and does not show any presence of impurities. Analysis of all five implants gave very similar spectra. It can be seen that the highest and most prominent peak is titanium, followed by smaller peaks of aluminum and vanadium.

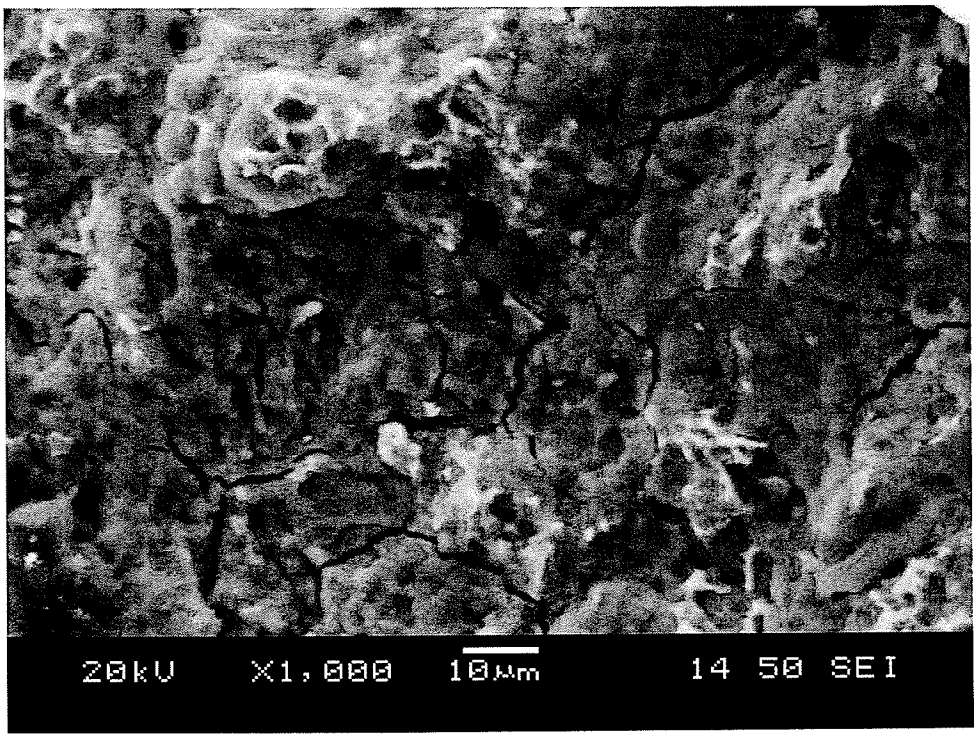

FIGURE 34: UNKNOWN LAYER COVERING SLOW FATIGUE ZONE OF IMPLANT #3 TAKEN AT 1000X

Figure 34 shows an image of the layer of unknown material that was on the slow fatigue zone of implant #3. This layer was present on all five fracture surface pairs in the slow fatigue zone, which made it extremely difficult to view microscopic striations. When the electron beam from the SEM remained in any area of this layer for more than only 2-3 seconds, the layer would then proceed to start cracking due to the heat from the beam. This can be seen in the image above.

The sample that was studied in Figure 31 that showed the layer separated from the fracture surface was examined under the SEM. Initially, this layer was thought to be biological. However, when chemical analysis was done only on the layer, the peaks that the EDS generated showed mostly titanium, with smaller peaks of aluminum, vanadium, and oxygen. Also, if the layer was biological, the surface would have started to charge

underneath the electron beam of the SEM, creating a very bright microscopic image. The results from the chemical analysis indicate that the layer most likely an oxide layer (TiO_2) that is created on the surface as a result of corrosion by extracellular fluid.

The presence of the TiO_2 layer in a crevice will cause the crack to propagate slightly faster. This is because the density of TiO_2 is 4.23 g/cm^3, which is slightly less than the density of Ti-6Al-4V, which is 4.43 g/cm^3 [29]. The lower density TiO_2 must occupy the same space as the Ti-6Al-4V once did, and thus expands. This creates high stresses at the crack tip and causes a wedging action, making the crack propagate faster [30]. This has a small effect on the progression of crack propagation, since crack propagation occupies only the final few percentage of the fatigue life and thus has little effect on the total life of the implant [19]. Therefore, it is not the mechanism that causes implant failure.

Since the oxide layer had separated from the fracture surface during the mounting process, the sample was removed from the Bakelite in order to view the fracture surface without the TiO_2 layer. However, when this was done and the sample was re-examined under the SEM, the oxide layer was still present and restricting the view of any microscopic striations. The layer also continued to crack under the heat of the electron beam of the SEM. Therefore, this means that when the TiO_2 originally separated in the mounting process, only part of the layer actually separated from the surface.

In another attempt to remove the oxide layer, the sample was put into a furnace for a half hour at 270°C. Since the heat from the mounting process caused the oxide layer to separate from the fracture surface, the high temperature used with the furnace should have accomplished the same thing. When the sample was removed from the furnace, the

surface was lightly brushed with a soft brush to remove any part of the layer that separated. However, when the sample was re-examined again under the SEM, the TiO_2 layer was still present. This means that the layer must have separated from the fracture surface due to the combination of high temperature and high pressure from the mounting machine. Due to the presence of the oxide layer and the unsuccessful removal of it, striations could not be seen in the slow fatigue zone of the fracture surface.

All images obtained from the optical microscope and SEM show typical microstructures of Ti-6Al-4V and confirm that failure occurred by fatigue. There was no evidence of stress corrosion cracking, general corrosion (i.e. crevice corrosion, corrosion fatigue, pitting corrosion), major material defects (i.e. high inclusion content, porosity), or any other defect that would contribute to failure of the implant in vivo. This was expected since implants are not made out of materials that experience such problems in vivo anymore. There was also no evidence of a notch created on the stem from being pulled into the body component. Therefore, further investigation must occur to delineate the reasons for failure.

4.2 Macroscopic Analysis of the Modular Hip System and the Bone Ingrowth of the Patient

As mentioned in Chapter 3, several methods were used for macroscopic analysis. From macroscopically examining the two mating fracture surfaces of the hip stem, the majority of the conclusions that were obtained from microscopic analysis were confirmed. It was clear that the implants failed by fatigue since a slow fatigue zone, a

rapid fracture zone, and curved beachmarks indicating a point of crack initiation were macroscopically visible on the fracture surfaces. The area of the slow fatigue zone and the rapid fracture zone varied from implant to implant, as did the topography of the fracture surface. Beachmarks were visible and distinct, and their curvature indicated the point of crack initiation on the lateral side of the stem. Macroscopically, there were no other major surface features.

Stem fixation of the five patients was examined by studying patient radiographs and by visual inspection. The radiographs prior to implant fracture were obtained from the UMJRG and were analyzed for several factors. More specifically, they were examined for stem fixation, medial and lateral bone at the body, medial and lateral bone continuity across the junction, and medial and lateral bone ingrowth at the body. If bone was present at the medial and lateral part of the body, it was determined if there was less than or greater than 50% present comparing to a healthy femur. The results of each radiograph of the five fractured hip stems are discussed next.

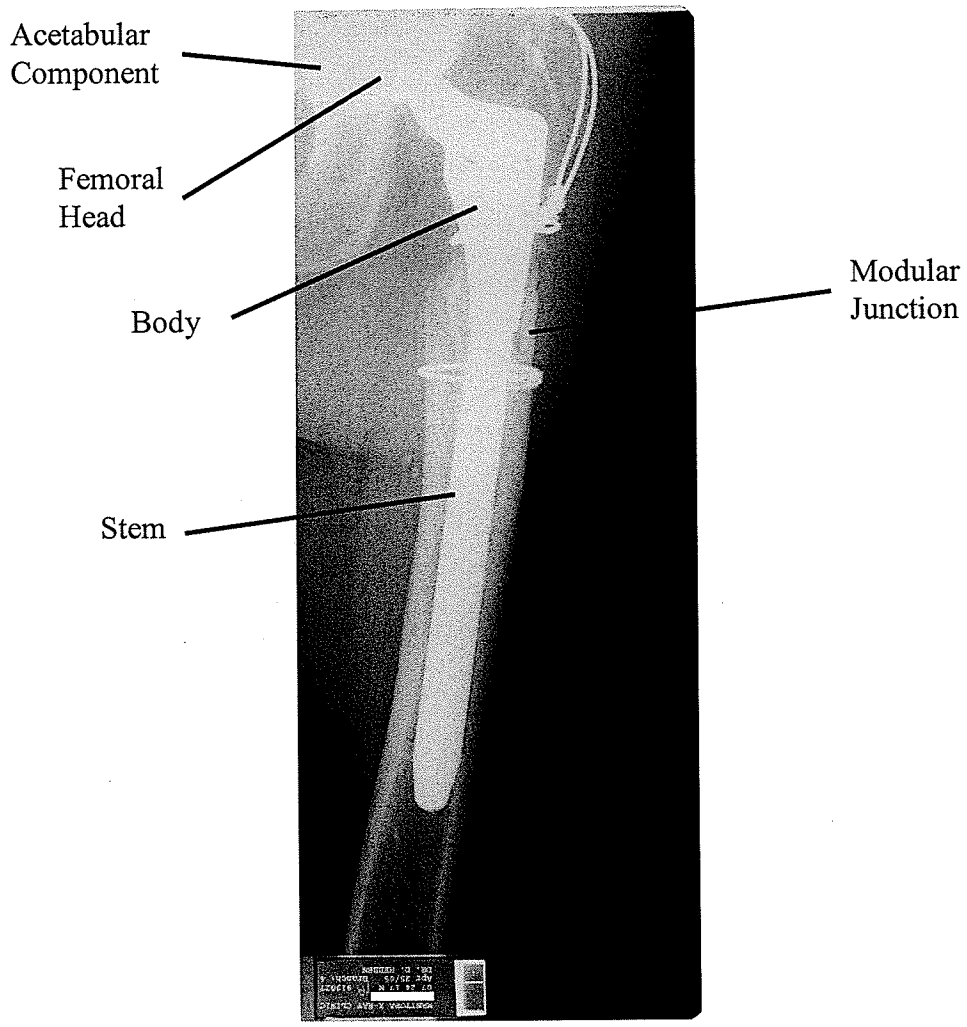

FIGURE 35: RADIOGRAPH OF IMPLANT #1 BEFORE STEM FRACTURE

Figure 35 shows the radiograph of implant #1 prior to implant failure. From this image, it can be seen that the stem is fixated in the femur since there are no reactive lines surrounding the femoral stem. In fact, there was no subsidence when comparing this to the previous radiograph. This confirms stem fixation. A close-up of the medial and lateral bone at the body can be seen in Figure 36.

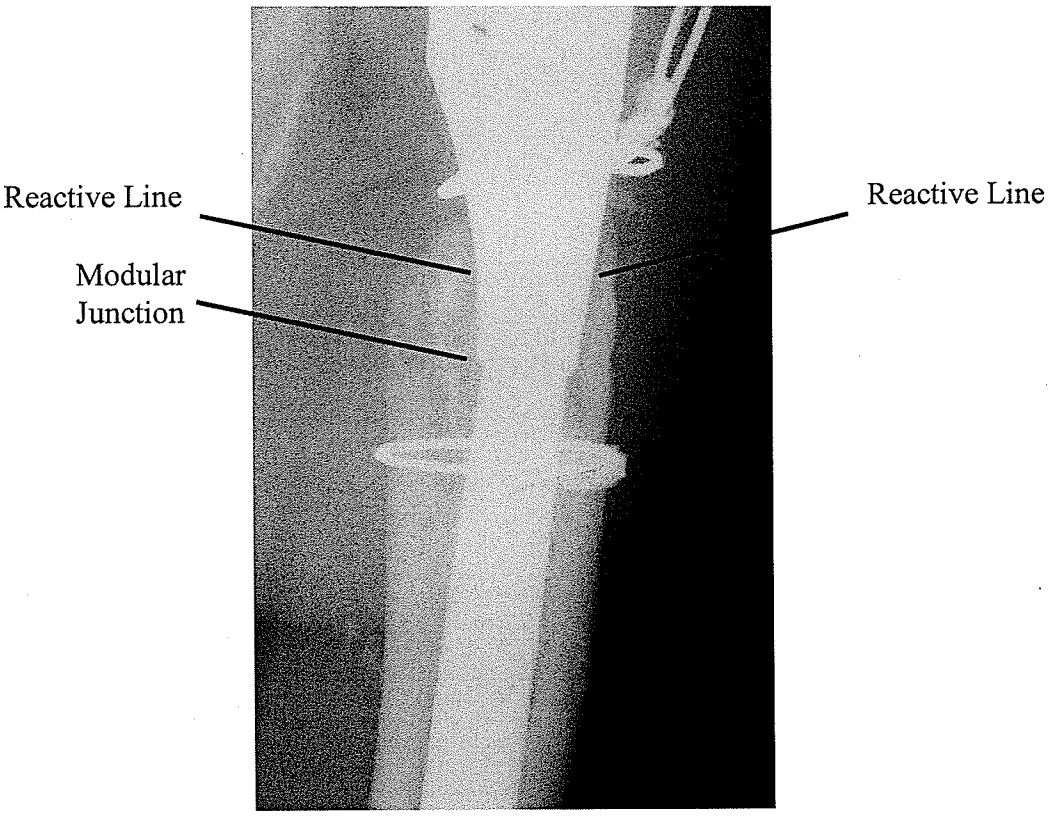

FIGURE 36: CLOSE-UP OF RADIOGRAPH OF IMPLANT #1

By examining the medial bone as shown in Figure 36, it is clear that there is less than 50% present. Although the medial bone is continuous across the modular junction, there does not appear to be medial bone ingrowth at the body. By examining the lateral bone, it is also clear that the femur extends across less than 50% of the body. Similarly, the lateral bone is continuous over the modular junction, but does not appear to be ingrown onto the body. There are no spot welds present.

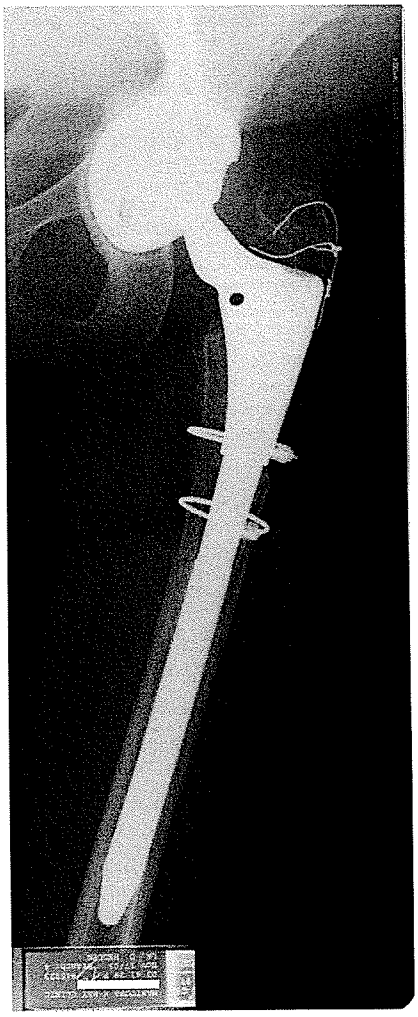

FIGURE 37: RADIOGRAPH OF IMPLANT #2 BEFORE STEM FRACTURE

Figure 37 shows the radiograph of implant #2 prior to implant fracture. From this image, it can be seen that there are no reactive lines along the stem. Therefore, stem fixation has been achieved. A close-up of the medial and lateral bone at the body is shown in Figure 38.

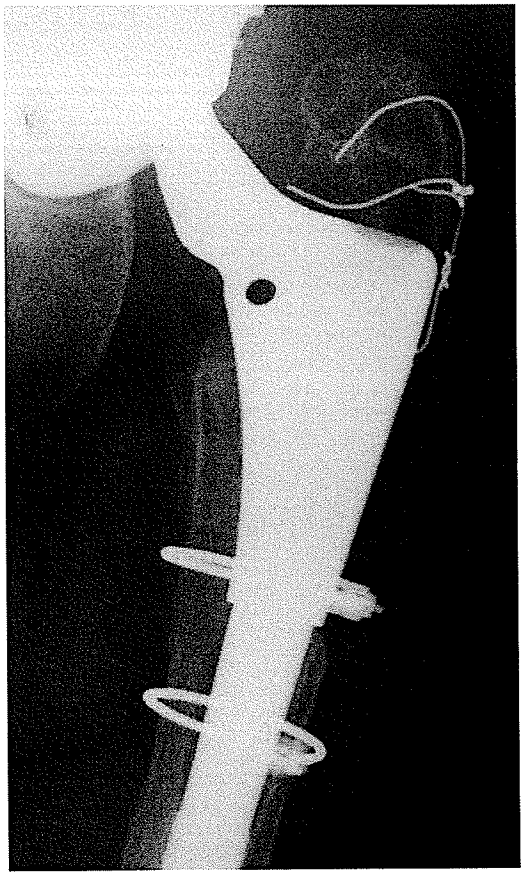

FIGURE 38: CLOSE-UP OF RADIOGRAPH OF IMPLANT #2

By examining Figure 38, it can be seen that there is greater than 50% of medial bone at the body. It can also be seen that the medial bone is continuous across the medial junction and that it is probable that bone has ingrown here. On the other hand, there is close to 0% of lateral bone at the body. Although there is evidence that the greater trochanter is present, there is no lateral bone connecting this to the femoral shaft.

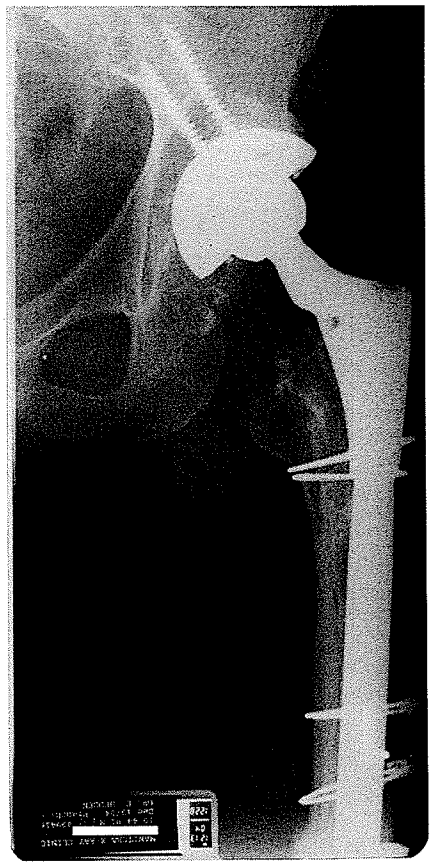

FIGURE 39: RADIOGRAPH OF IMPLANT #3 BEFORE STEM FRACTURE

Figure 39 shows the radiograph of implant #3 prior to implant fracture. This image shows stem fixation with no reaction lines along the canal of the femur. A close-up of the medial and lateral bone at the body can be seen in Figure 40.

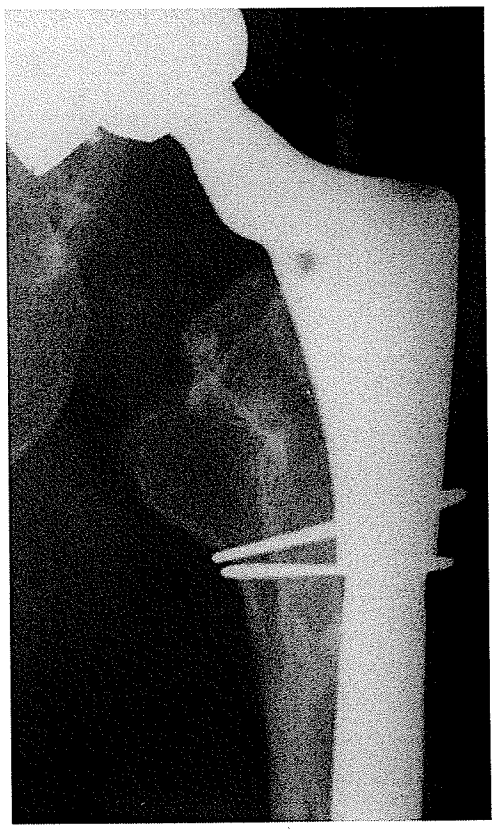

FIGURE 40: CLOSE-UP OF RADIOGRAPH OF IMPLANT #3

Figure 40 shows that there is greater than 50% of medial bone at the body. In fact, it appears as though the medial bone and lesser trochanter are very comparable to a healthy femur. It can also be seen that the medial bone is continuous across the medial junction and that most likely, the bone has ingrown here. There is also greater than 50% of lateral bone at the body. However, the lateral bone is not continuous over the modular junction and is not ingrown into the body.

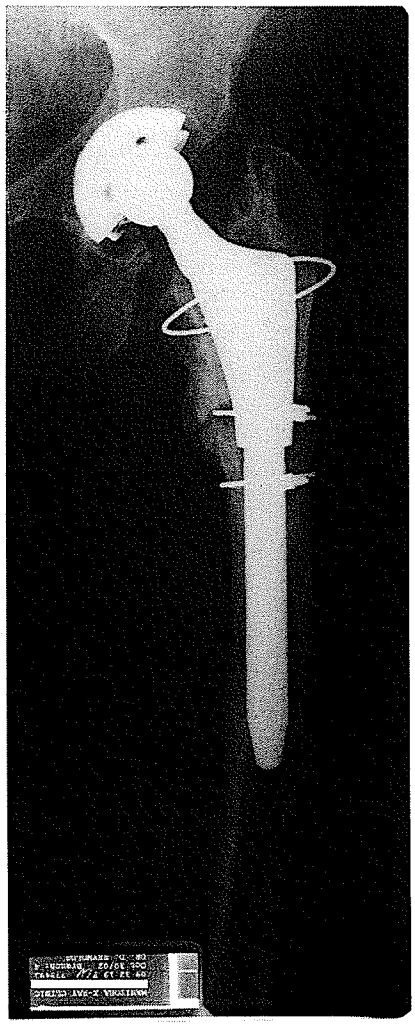

FIGURE 41: RADIOGRAPH OF IMPLANT #4 BEFORE STEM FRACTURE

Figure 41 shows the radiograph of implant #4 prior to implant fracture. From this image, it can be seen that the stem is fixed distally in the femur. There are no reactive lines present around the stem. A close-up of the medial and lateral bone at the body can be seen in Figure 42.

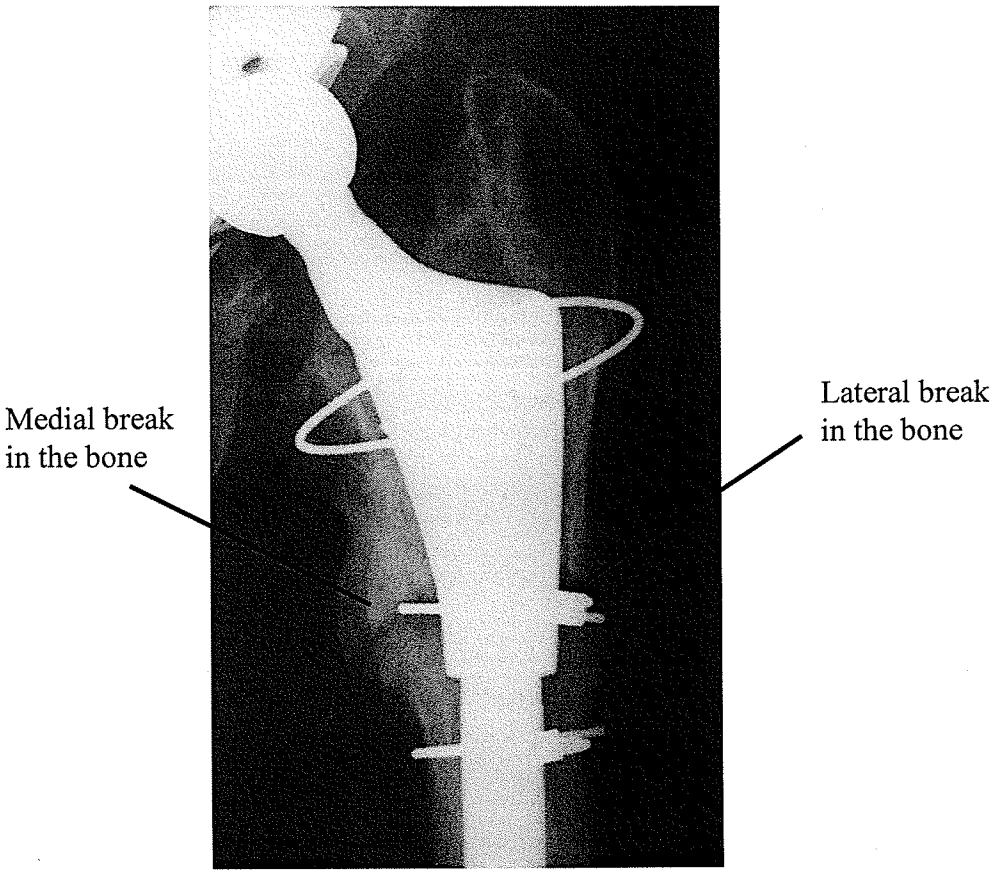

FIGURE 42: CLOSE-UP OF RADIOGRAPH OF IMPLANT #4

Figure 42 shows that there is greater than 50% of medial bone at the body. However, the radiograph shows that the medial bone is not continuous over the modular junction since there is a break in the bone slightly above the modular region. Due to the fact that there is no medial ingrowth, the small portion of the bone that extends slightly over the modular junction is disregarded. The lateral side has greater than 50% of bone present, but experiences the same problem as the medial side in that there is no ingrowth. The lateral bone also contains a break in the bone slightly above the modular region, but since there is no bone ingrowth on the lateral side, the small portion of bone that extends

slightly over the modular junction is disregarded. Therefore, it is considered that the lateral bone is not continuous over the modular junction.

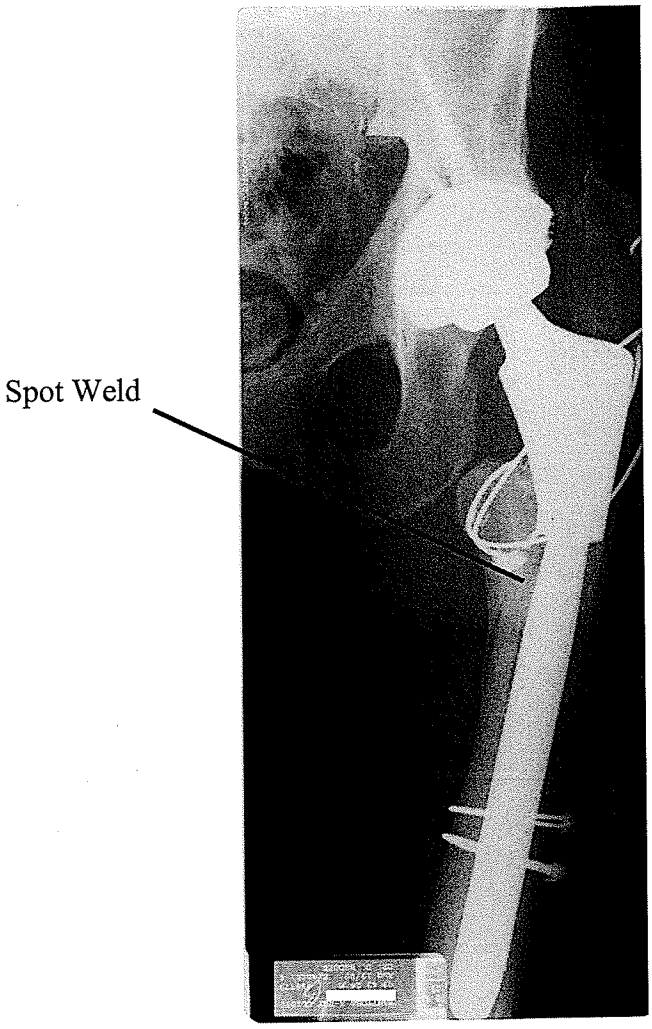

FIGURE 43: RADIOGRAPH OF IMPLANT #5 BEFORE STEM FRACTURE

Figure 43 shows the radiograph of implant #5 prior to implant fracture. This image shows that the stem is fixated distally in the canal of the femur. A spot weld directly below the modular junction can be seen on the medial side and there is a lack of

reactive lines along the stem in the femur. These provide confirmation of stem fixation. A close-up of the medial and lateral bone at the body can be seen in Figure 44.

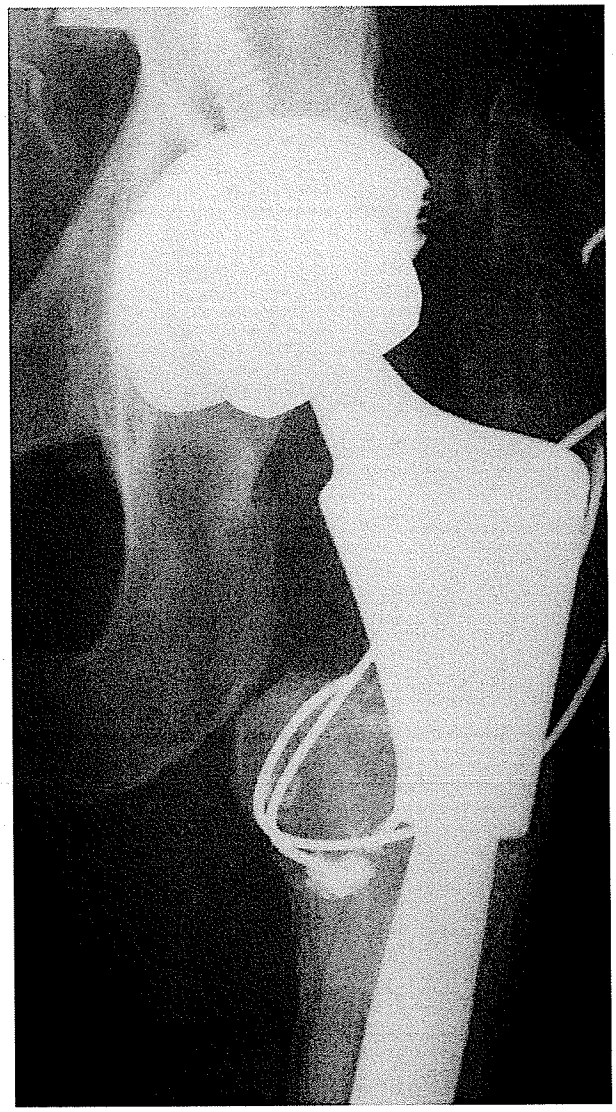

FIGURE 44: CLOSE-UP OF RADIOGRAPH OF IMPLANT #5

Figure 44 shows that there is less than 50% of medial bone present. Despite this, the medial bone is continuous over the modular junction and is ingrown into the body of

the implant. The lateral side also has less than 50% of bone present. Although the lateral bone is continuous over the modular junction, there is no bone ingrowth on this side.

A summary of these radiographic results can be seen in Table 7.

TABLE 7: SUMMARY OF RESULTS OF BONE INGROWTH ANALYSIS OF THE PATIENT FEMURS USING PATIENT RADIOGRAPHS

	Stem Fixed	Medial Bone at Body	Medial Bone is Continuous Across the Junction	Medial Bone Ingrowth at Body	Lateral Bone at Body	Lateral Bone is Continuous Across the Junction	Lateral Bone Ingrowth at Body
Implant #1	Yes	< 50%	Yes	No	< 50%	Yes	No
Implant #2	Yes	≥ 50%	Yes	Probable	0%	No	N/A
Implant #3	Yes	≥ 50%	Yes	Probable	≥ 50%	No	No
Implant #4	Yes	≥ 50%	No	Probable	≥ 50%	No	No
Implant #5	Yes	< 50%	Yes	Yes	< 50%	Yes	No

As mentioned in Chapter 3, ingrowth was defined as "yes" if there were spot welds present or if there was no evidence of subsidence, as "probable" if there were no spot welds present, but cortical bone was intimate to the stem and no radiolucent lines were present, and as "no" if radiolucent lines were present and/or evidence of subsidence. Proximal bone was investigated to determine if the body component was supported properly in vivo, which could prevent fatigue failure at the modular junction. By looking at Table 7, stem fixation was always present in all five implants studied. Medial bone, though varying in percentage and bone ingrowth, was always present and in four out of five cases, was continuous across the modular junction. Lateral bone at the body was only present in four out of five cases and varied in percentage. The lateral bone was also only

continuous across the modular junction two out of five times. In all five cases, there was no lateral bone ingrowth at the body.

Visual inspection of the body and the stem component of the modular hip implant was done to determine the presence of any osseointegration into the textured surface of the implant and to compare it to the radiographic findings. The following table summarizes the results.

TABLE 8: SUMMARY OF RESULTS FROM INSPECTING IMPLANT BODY AND STEM

	Medial Bone Ingrowth at Body	**Lateral Bone Ingrowth at Body**	**Distal Bone Ingrowth at Stem**
Implant #1	No	No	Yes
Implant #2	No	No	Yes
Implant #3	No	No	Yes
Implant #4	No	No	N/A
Implant #5	No	No	Yes

By looking at Table 8, it can be seen that by examining the body, there was no bony ingrowth on the medial and lateral side of all of the implants examined. In all cases where the stem was available, there was bony ingrowth, which confirms the bone ingrowth analysis done using the patient radiographs. However, when comparing the results of the medial bone ingrowth at the body from Table 8 of implants #2, #3, #4, and #5 with the same implants of Table 7 (x-ray findings), the observations are in disagreement. Although osseointegration may have appeared to be present at the medial body in the patient radiographs, visual inspection of the body indicate that this is not the case. This implies that examining patient radiographs are not exact and will only suggest certain findings, which must be confirmed or refuted by visual inspection of the

components. Therefore, it appears as though along with lack of lateral bone ingrowth, there was no medial bone ingrowth at the body either.

During loading of the modular hip implant in vivo, the medial side of the implant experiences compression and the lateral side experiences tension. This is why crack initiation of the stem occurs on the lateral side. If proper lateral bone support is present that has ingrown into the body of the implant, the lateral side may be supported better and may not experience as high of a tensile force. Alternately, a proper medial support that has ingrown into the body would decrease the moment arm that is created during loading, which would thus decrease the compressive and tensile stresses on both sides of the stem.

During the insertion surgery of the modular hip implant, an extended trochanteric osteotomy is often performed in order to drill down properly into the femur, ream out the canal, and position the implant accordingly. This is done by cutting a portion of the proximal end of the femur, including the trochanter, away during surgery. Once the modular implant is inserted into the patient, the portion that was removed is shaved down to accommodate the implant and is placed back with the femur, and the entire area is bound together using metal cables. This is done to hold the proximal end of the femur together so that the bone can grow into the proximal end of the implant. These cables can be seen in the patient radiographs in Figures 35-44. If the lateral bone from the osteotomy does not grow into the porous surface of the modular implant, the lateral side of the implant will have to withstand the entire tensile load on its own. Therefore, when a load is placed on the femoral head, the lateral side will tend to pull away from the osteotomy, since the lateral side is in tension. This creates more stress on the medial side bone, since it experiences compression, and less stress on the lateral side bone. Because of this,

according to Wolff's Law, the bone on the medial side will grow and osseointegrate into the medial side of the porous body component, while the bone on the lateral side will resorb. This may explain why in most cases that were studied, medial bone was present and appeared to be ingrown in the radiographs, whereas lateral bone was not present and thus not ingrown.

After examining patient radiographs, the operative reports of the modular implant insertion surgery were reviewed for mention if a bone graft on the femur was used during the operative procedure. The following table summarizes the results.

TABLE 9: SUMMARY OF RESULTS FROM REVIEWING OPERATIVE REPORTS

	Bone Graft Used During Implant Insertion	**Bone Graft Used After Implant Removal**
Implant #1	No	Yes
Implant #2	No	Yes
Implant #3	Yes	No
Implant #4	Yes	No
Implant #5	No	Yes

By looking at Table 9, it can be seen that bone graft was only used during the insertion surgery of implants #3 and #4. Both of these were grafted on the lateral side of the femur for proximal reconstruction. It should be noted that by looking at Table 7, implants #3 and #4 are the only implants being studied that had greater than 50% of lateral bone present at the body. However, osseointegration did not occur with the lateral bone present from the bone graft. Implants #1, #2, and #5 did not have any type of bone grafted onto the proximal femur during surgery, which reflected when examining the quantity of bone present in the radiographs prior to implant fracture.

It is of interest to calculate an approximation of the expected life of the retrieved modular hip stem. Over the course of one year, the hip implant experiences approximately 1 million cycles [7]. Since the average lifetime in vivo of the implants studied was approximately 4 years, this would mean that these modular implants experienced approximately 4 million cycles before failure.

Looking back to Table 2, it was shown that the fatigue strength or limit at 10 million cycles for hot forged Ti-6Al-4V was approximately 420 MPa. This means that Ti-6Al-4V can undergo up to 10 million cycles under a load of 420 MPa. In fact, the fatigue strength remains at approximately 420 MPa from 500,000 cycles onwards [9]. However, this value was obtained using a ± 420 MPa load, which is more severe than a 0-420 MPa load that a hip implant would experience. Referring back to Table 6, the average patient mass was 88 kg. Using the equation

$$F = mg \tag{4.1}$$

where g is the gravitational constant (9.81 N/kg) and m is the average patient mass, and assuming that the force applied is vertically downward on the implant and is distributed evenly, this means that the average force applied to the femoral head of the implant can be calculated as follows.

$$F = \left(88kg\right)\left(9.81\frac{N}{kg}\right)$$

$$= 863.28N$$

The femoral head experiences a force 2.4 times of that created from body weight during normal gait [31]. This means that the proximal end of the femur will actually experience

$$F = (2.4) * (863.28N)$$

$$= 2{,}072N$$

Therefore, this force of 2,072 N must theoretically result in a tensile stress due to bending at the fracture site of approximately 420 MPa to cause failure in 4 years.

4.3 Finite Element Analysis of the Modular Hip Implant

The modular Ti-6Al-4V hip implant was three-dimensionally modeled using Pro-Engineer Wildfire 2.0 (© 2004). There were several assumptions made when creating this model and some of the more difficult dimensions to obtain were estimated using a pair of dial calipers. Also, when each component of the modular hip implant was modeled, that is, the head, the body, and the stem, each part was drawn up to where it mated with another part. Each of these surfaces was joined together to create one solid component. Components were not drawn so that they overlapped in any way. Due to this, the assumption to neglect micro-motion was also made. In addition to this, all rounds and fillets on the surface of the modular implant were removed, since this is a requirement for Pro-Mechanica to function properly.

Once a three-dimensional model was created, a load of 2,072 N was applied to the femoral head of the modular implant using Pro-Mechanica. This value was previously calculated to be the average force created on the head of the femur by the patients that experienced a fractured modular hip implant in this study. This force was assumed to be applied vertically downwards on the femoral head, when in reality, the force is slightly on an angle from the vertical axis. In addition to this, the distal portion of the stem was

constrained to allow no movement during loading. This assumes that the stem is fixed distally in the canal of the femur in vivo, which was the case for each of the stems that was available. An image of the modular implant model with these parameters can be seen in Figure 45.

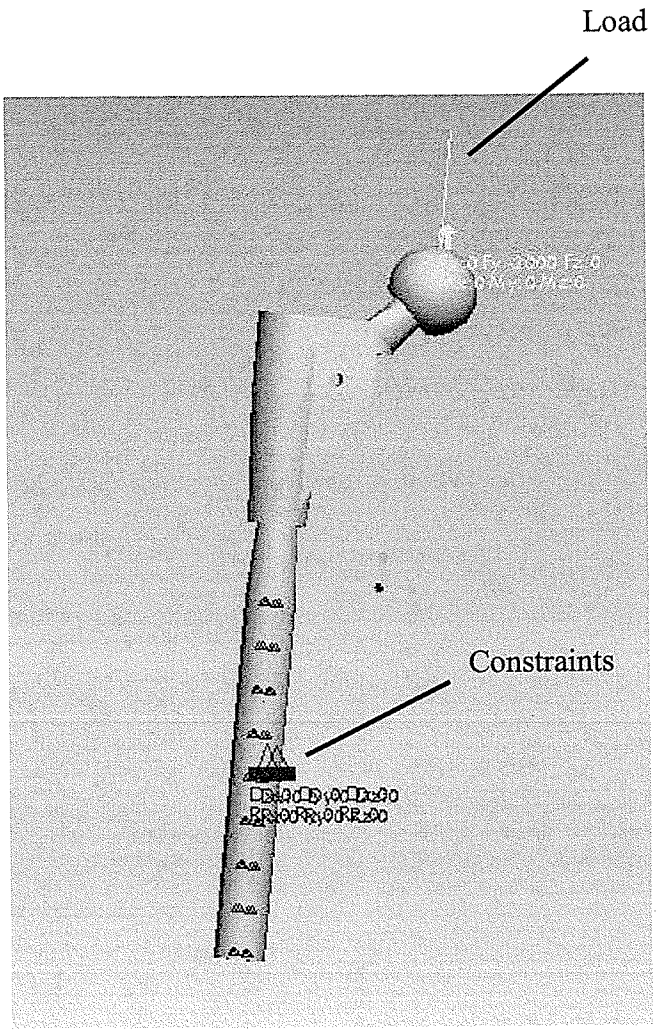

FIGURE 45: MODEL OF THE MODULAR IMPLANT WITH LOAD AND CONSTRAINTS

Using the Pro-Mechanica program, the model was simulated with the given stress and constraint. An anterior view of the stress distribution is displayed in Figure 46.

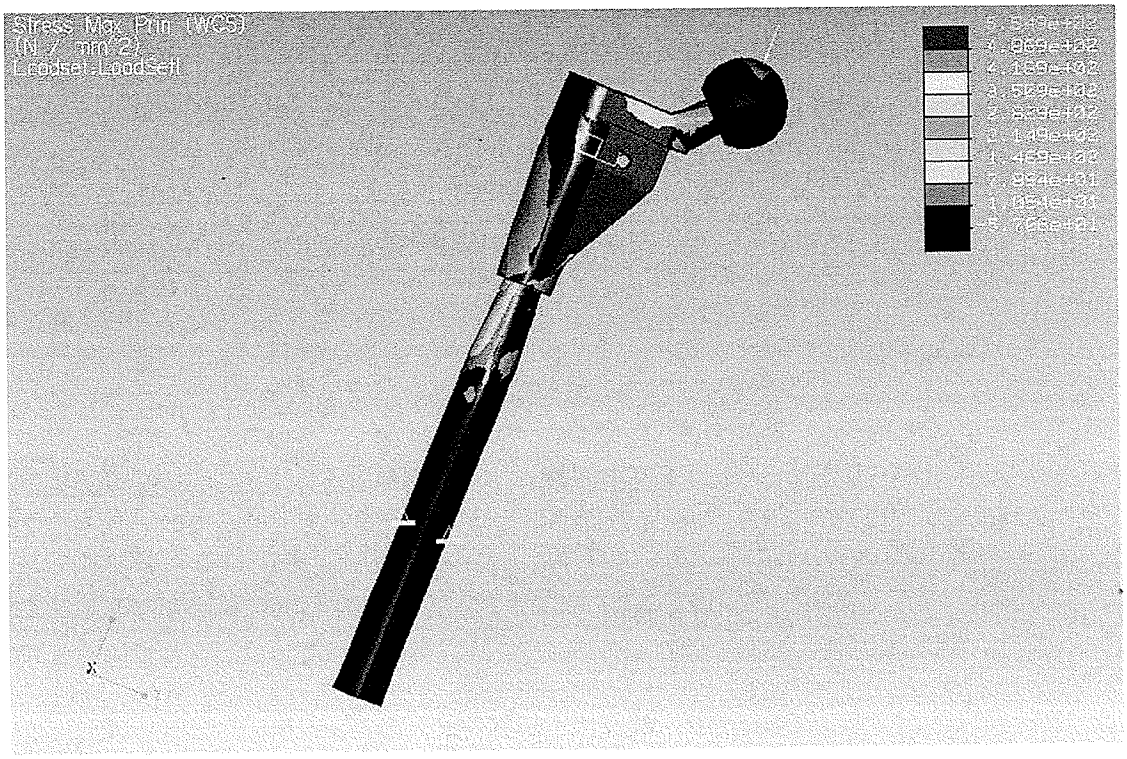

FIGURE 46: ANTERIOR VIEW OF THE FINITE ELEMENT ANALYSIS RESULTS OF THE MODULAR HIP IMPLANT

Figure 46 shows the stress distribution through the modular hip implant when a stress of 2,072 N is applied to the femoral head and the distal stem is fixed. It can be seen that the majority of the modular implant experiences approximately 5.7 N/mm^2, or 57 MPa, and is in compression, which is indicated by the negative value on the scale. However, lighter areas indicate tensile forces, which can be seen by the positive values on the scale. Although the neck of the body component that is mated with the femoral head experiences tensile forces on the superior side, these stresses are low ($\approx$ 79 MPa) in comparison to the lateral side of the modular junction of the stem and body. This can be seen in Figure 47.

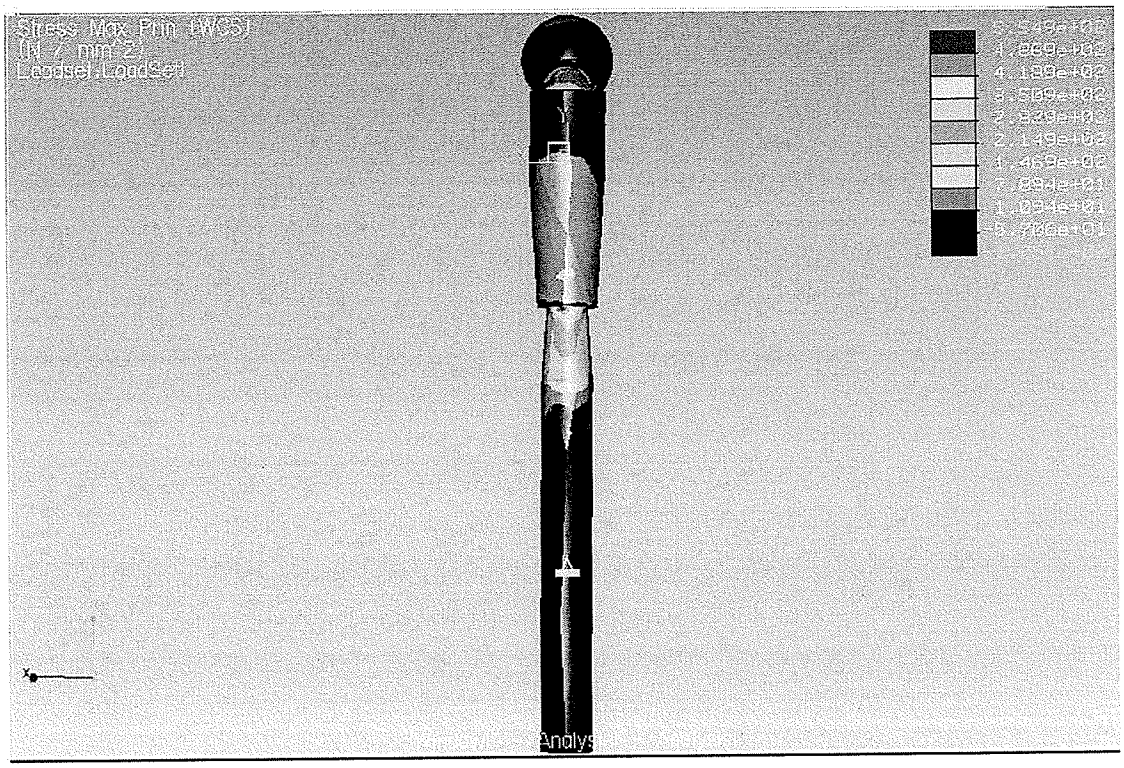

FIGURE 47: LATERAL VIEW OF THE FINITE ELEMENT ANALYSIS RESULTS OF THE MODULAR HIP IMPLANT

In Figure 47, the modular junction is the only part of the entire implant that experiences high stresses. The lateral side of the body experiences approximately 11 MPa, whereas the lateral side of the stem varies in stress. Figure 45 provides a close-up view of lateral side of the modular junction.

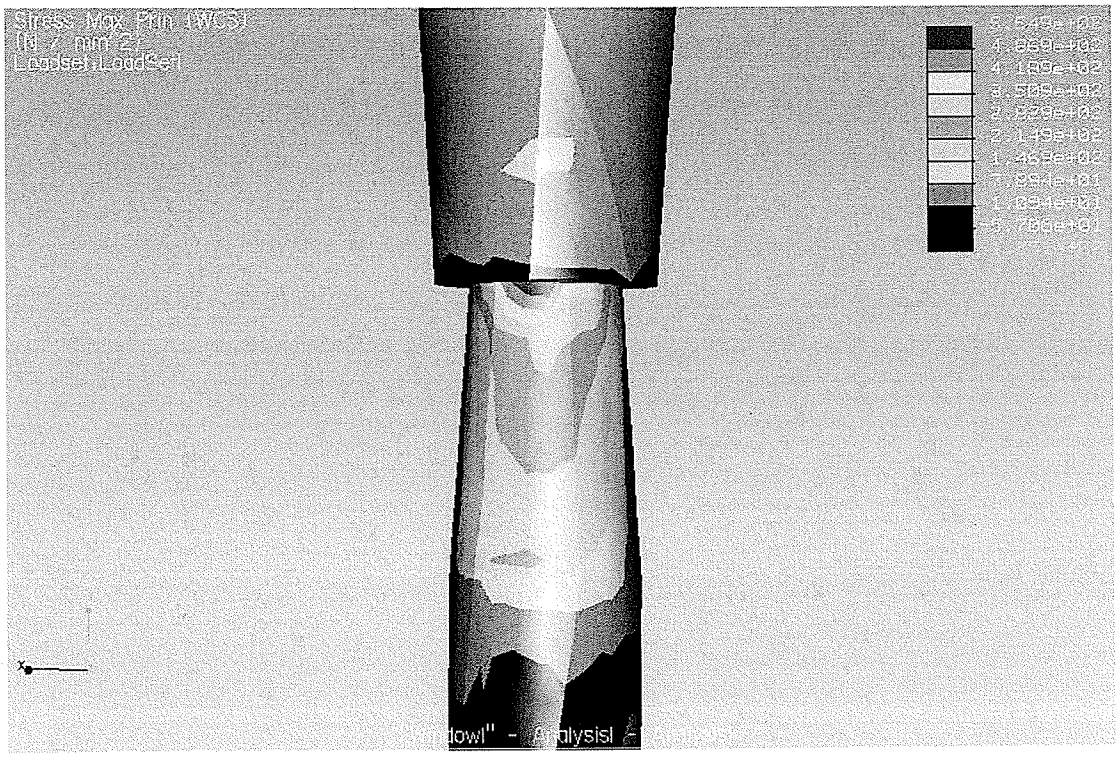

FIGURE 48: LATERAL VIEW OF THE FINITE ELEMENT ANALYSIS RESULTS OF THE MODULAR JUNCTION

From the close-up shown in Figure 48, it can be seen that as the modular junction on the lateral side is approached from the distal end, the stresses increase from approximately 11 MPa to 487 MPa. Although there is a high stress created at this interface, it is important to note that the typical yield strength of Ti-6Al-4V is 950 MPa and the fatigue strength or limit at 500,000 cycles and higher is approximately 420 MPa, which was shown in Table 2. The stress created at the junction, as shown by Figure 48, is slightly higher than the implant's fatigue strength and is approximately half the yield stress. This may contribute to failure of the modular stem.

To confirm the FEA results, the stress at the modular junction was calculated mathematically. When modeling the modular implant, the distance, *d*, from the centre

line of the femoral head to the centre line of the stem was approximated to be 0.0517 m (2.04 in). Therefore, the following calculations can be made:

$$M = Fd \tag{4.2}$$

where M is the moment created at the proximal end of the implant and F is the force created at the femoral head. Therefore, using the values previously found,

$$M = (2{,}072\ \text{N})*(0.0517\ \text{m})$$

$$= 107.12\ \text{N·m}$$

From here, using the moment calculated, the stress created at the modular junction can be estimated.

$$\sigma = \frac{My}{I} \tag{4.3}$$

where σ is the stress created at the modular junction, y is the distance to the neutral axis, and I is the moment of inertia. In order to obtain a value for the stress, the moment of inertia needs to be calculated. If it is assumed that the radius of the stem at the modular junction is approximately 0.00635 m (0.25 in), then

$$I = \frac{\pi r^4}{4} \tag{4.4}$$

$$= \frac{\pi(0.00635m)^4}{4}$$

$$= 1.277x10^{-9}\,m^4$$

Using the calculated moment of inertia, the stress can now be calculated with equation 4.3.

$$\sigma = \frac{(107.12N \cdot m)(0.00635m)}{1.277x10^{-9}\,m^4}$$

$$= 533MPa$$

It can be seen that the stress calculated is slightly higher than the value given through Pro-Mechanica (487 MPa). A higher value was expected in our calculations. This is because in the FEA, the bending moment created from the load at the femoral head causes a tensile force at the modular junction, yet the load also creates a compressive force throughout the stem. Therefore, this causes a decrease in the tensile component applied resulting in a slightly lower stress at the modular junction in the FEA. When doing calculations using equations, this factor is not considered, thus resulting in a slightly higher stress at the modular junction. Also, the calculated value is exceeding the fatigue strength or limit of Ti-6Al-4V at 500,000 cycles and higher.

Given the mathematical relationships above, it can be seen that if the distance that the moment acted over in equation 4.2 were reduced, the overall stress that the modular junction would experience would decrease as well, as shown by equation 4.3. Therefore, a medial bone support was added to the three-dimensional model to act as a medial bone graft and to compare the stress created at the modular junction. In Pro-Mechanica, the medial support was assumed to be similar to a vertical beam support and was constrained at the distal end to allow no movement. This assumes osseointegration of the bone graft added in vivo. An image of the modular implant model with the bone support is given in Figure 49.

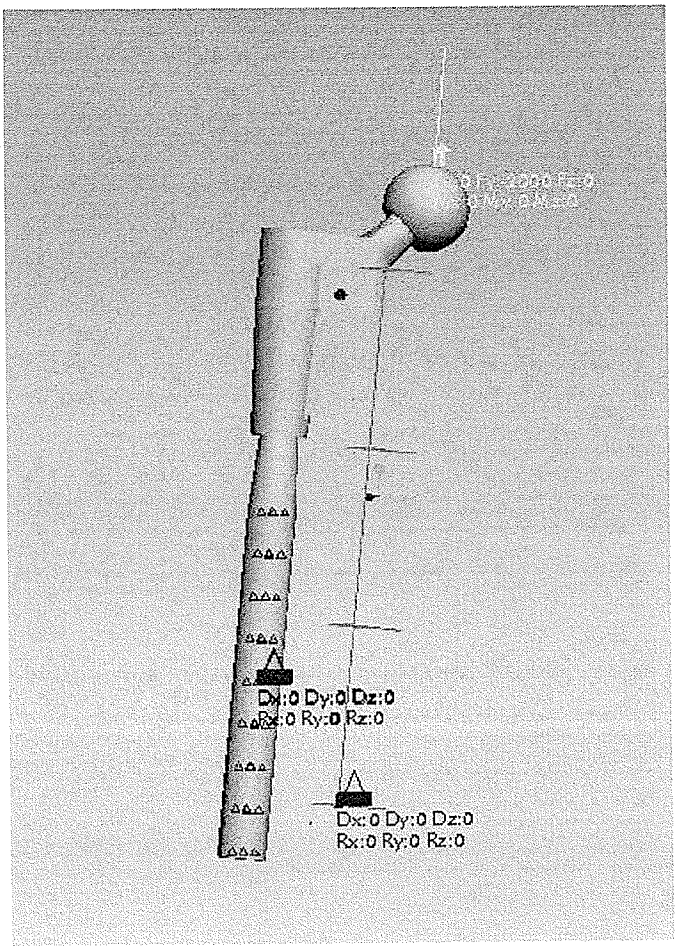

FIGURE 49: MODEL OF THE MODULAR IMPLANT WITH THE MEDIAL BONE SUPPORT, LOAD, AND CONSTRAINTS

Using the same parameters as before, the model was simulated in Pro-Mechanica with the same load of 2,072 N. An anterior view of the stress distribution is displayed in Figure 50.

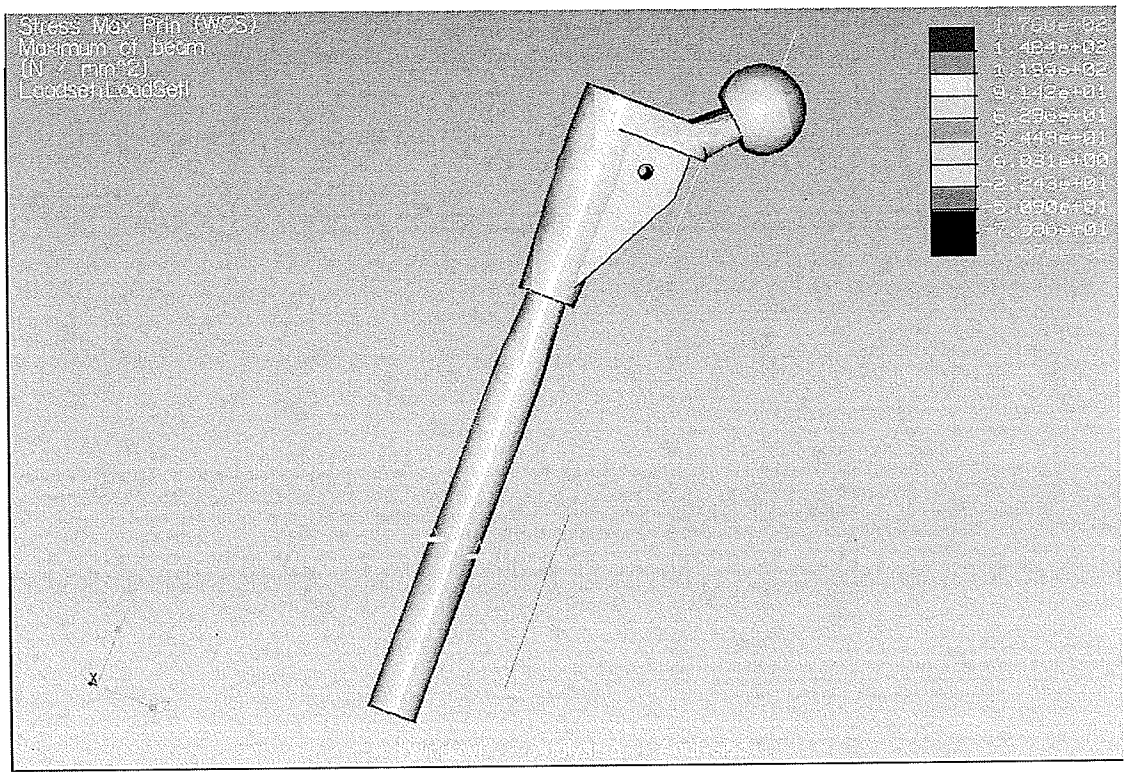

FIGURE 50: ANTERIOR VIEW OF THE FINITE ELEMENT ANALYSIS RESULTS OF THE MODULAR HIP IMPLANT WITH THE MEDIAL BONE SUPPORT

From Figure 50, it can be seen that the overall stress distribution in the modular hip implant has decreased significantly. The majority of the implant now experiences only approximately 22 MPa of compressive stress. It can also be seen that the neck of the body component that is mated with the femoral head now experiences a slightly smaller tensile force of approximately 60 MPa. More importantly, the stress experienced at the modular junction decreased. This can be seen in Figure 51.

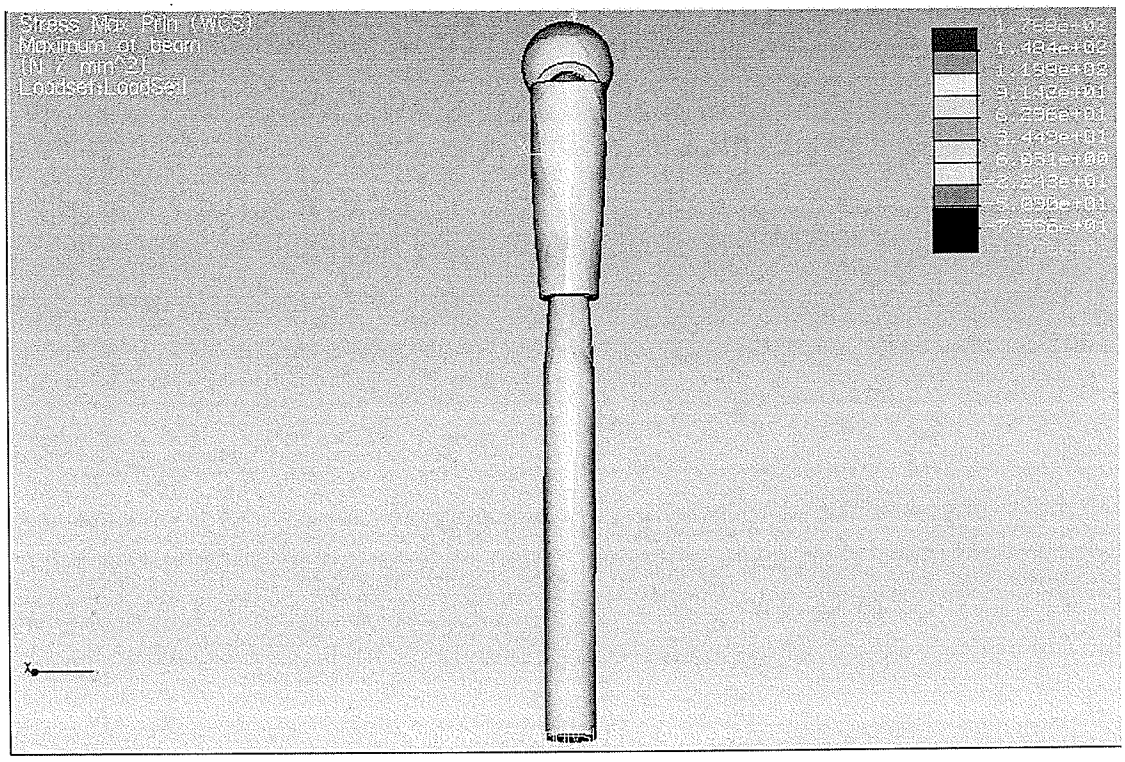

FIGURE 51: LATERAL VIEW OF THE FINITE ELEMENT ANALYSIS RESULTS OF THE MODULAR HIP IMPLANT WITH THE MEDIAL BONE SUPPORT

Figure 51 shows that the stresses on the lateral side of the modular implant have decreased significantly. A closer image of the modular junction can be seen in Figure 52.

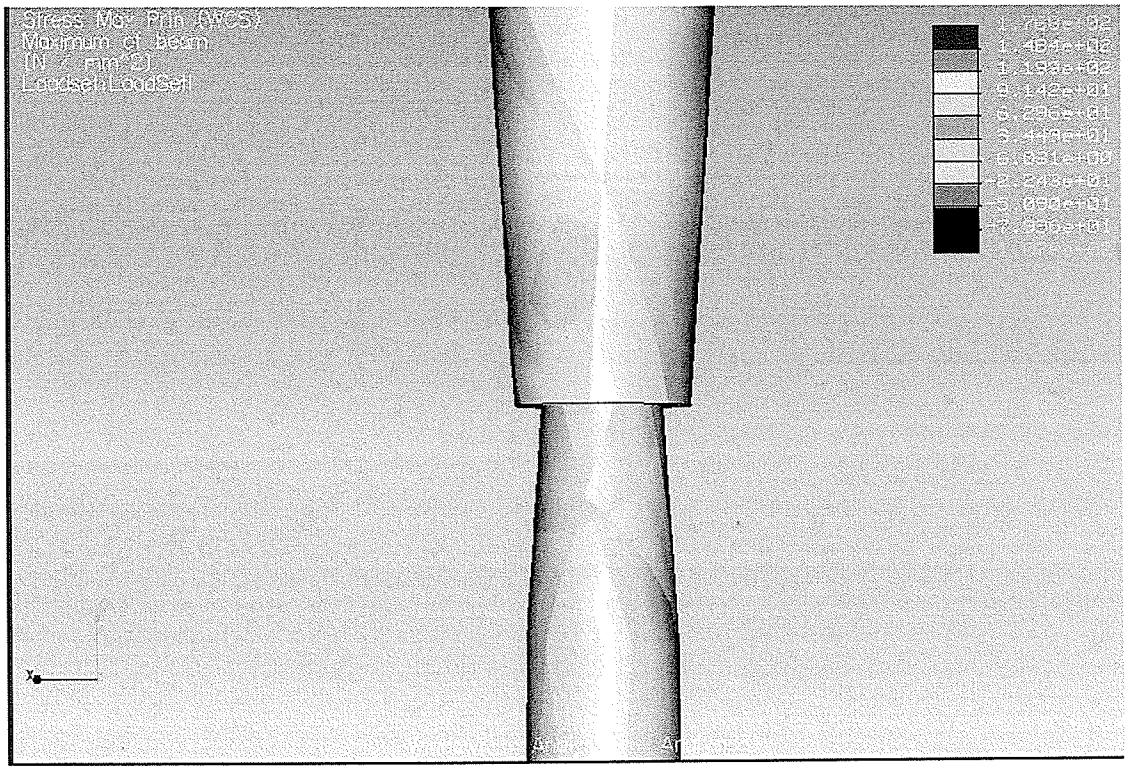

FIGURE 52: LATERAL VIEW OF THE FINITE ELEMENT ANALYSIS RESULTS OF THE MODULAR JUNCTION WITH THE MEDIAL BONE SUPPORT

From the close-up shown in Figure 52, it can be seen that the new stress at the modular junction is approximately 60 MPa in tension, which is significantly less than before (487 MPa).

To confirm the FEA results, the stress was mathematically calculated again at the modular junction. With the bone support added, the distance, *d*, from the centre line of the femoral head to the location of the bone support is 0.0162 m (0.64 in) in Pro-Mechanica. Therefore, the new moment created using equation 4.2 is as follows:

$$M = (2{,}072\ \text{N})*(0.0162\ \text{m})$$

$$= 33.56\ \text{N·m}$$

Using this new value for the moment, a new value for the stress can be calculated using equation 4.3 as follows:

$$\sigma = \frac{(33.56N \cdot m)(0.00635m)}{1.277x10^{-9}m^4}$$

$$= 166{,}880{,}187.9\,Pa$$

$$= 166.9\,MPa$$

This calculated value is again slightly higher than the value found using the program (60 MPa). This is again due to the fact that a compressive force is created in the FEA at the stem, which causes a decrease in the tensile component applied at the same location. Therefore, this creates slightly lower stresses at the modular junction than in the calculations.

In summary, by performing finite element analysis, the highest stress point was predicted to be at the modular junction of the implant. It was also predicted that by adding a medial bone support, the tensile stresses on the lateral side of the modular junction would be decreased substantially.

4.4 Mechanical Testing of the Modular Hip Stem

Tensile tests were done on the 6061 aluminum alloy and Ti-6Al-4V material to ensure compliance to typical values. The results obtained from tensile testing are shown in Table 10.

TABLE 10: SUMMARY OF RESULTS FROM TENSILE TESTING OF THE 6061 AL ALLOY AND TI-6AL-4V

	Gauge Length, cm (in)	Gauge Diameter, cm (in)	Yield Stress, MPa (ksi)	Ultimate Tensile Strength, MPa (ksi)	Elongation, %
6061 Al Alloy *Test 1*	2.54 (1.00)	0.638 (0.251)	275.79 (40)	303.37 (44)	22
6061 Al Alloy *Test 2*	2.54 (1.00)	0.635 (0.250)	303.37 (44)	330.95 (48)	25
Ti-6Al-4V	2.13 (0.84)	0.579 (0.228)	912.87 (132.4)	963.20 (139.7)	20

By comparing the results of Table 10 with the values from Table 2 and 5, it is shown that the results obtained are close to typical values. It was shown in Table 5 that the tensile strength for the 6061 aluminum alloy is 310 MPa (45 ksi), the yield stress is 276 MPa (40 ksi), and that the elongation is 17%. The values obtained from the tensile testing of the 6061 aluminum alloy are in agreement with these values, especially test 1. In Table 2, it was shown that the tensile strength of Ti-6Al-4V is 1075 MPa (156 ksi) and that the elongation is 13%. The values obtained through the tensile test are relatively close to these values as well.

Hardness tests were also done to compare results to typical values. During the test, ten hardness readings were taken on the Rockwell A scale using a diamond brale indenter and an average of the ten readings was calculated. From here, a standard deviation was calculated as well. The results of the hardness tests can be seen in Table 11.

TABLE 11: SUMMARY OF RESULTS FROM HARDNESS TESTING OF TI-6AL-4V

	Mean Hardness, HRA	**Standard Deviation**
Sample From Specimen Used in Tensile Test	67.2	1.2
Implant #1	66.7	0.4
Implant #2	69.0	4.8
Implant #3 ***(Transverse Cross-Section)***	65.3	0.1
Implant #3 ***(Axial Cross-Section)***	66.2	0.4
Implant #4	66	0.4
Implant #5	66.6	0.3

The typical hardness value for Ti-6Al-4V is 32 HRC [8]. By looking at Table 11, it was found that the average value for hardness was 66.7 HRA. Using a simple hardness conversion table, it was found that 66.7 HRA equals approximately 33 HRC. Therefore, the values obtained through hardness testing also are in agreement with typical values.

Since the values obtained through tensile testing and hardness testing were extremely close to typical standard values and can withstand in vivo loads, it is evident that the modular stems are not failing in vivo due to incorrect mechanical properties.

As mentioned in Chapter 3, fatigue testing was done to replicate patient motion and to determine if the implant would fracture and fail by the same mechanism at the modular junction as in vivo. A total of twenty nine fatigue tests were done: twenty 6061 aluminum alloy stems and nine Ti-6Al-4V stems. The fatigue machine was set to apply a compressive load as a sine wave, with a frequency of 5 or 10 cycles per second. The minimum load was always set to 10% of the maximum load.

Of the twenty 6061 aluminum alloy stems that were tested, ten of them did not break. Although most of these bent due to a high load that was applied, two tests were stopped due to lack of results. Initially, a hole was made in the top circular plate of the compression cage for the femoral head to sit in, which acted as an acetabulum. A schematic of this is shown in Figure 53.

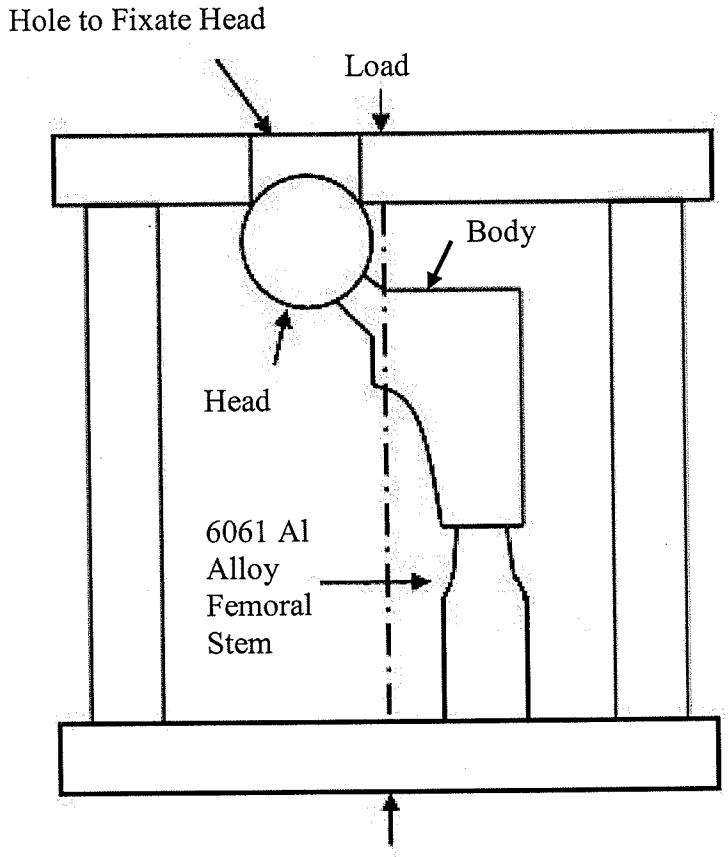

FIGURE 53: SCHEMATIC OF MODULAR HIP IMPLANT WITH THE 6061 AL ALLOY STEM IN COMPRESSION CAGE, WITH FEMORAL HEAD FIXED IN POSITION

These two tests that were stopped involved the femoral head sitting in this hole. The modular implant experienced high cycles at a high load, yet nothing happened to the 6061 aluminum alloy stem. Thus, the test was stopped in both cases. Since the femoral head sat in the hole made in the top circular plate, the ball was securely fixated and

created compressive forces in the whole implant, rather than tensile forces. Therefore, the implant did not break nor bend at the modular junction. Although fracture of the implant did not occur, one of the rods of the compression cage ended up fatiguing and fracturing due to the high load and high cycles. Thus, this rod plus its opposite rod, which were attached to the top circular plate of the compression cage, were replaced.

Since placing the femoral head in the hole created in the top plate was not providing sufficient results, the hole was covered with a plug made of polyethylene to prevent the femoral head from being restricted during fatigue testing, thus creating tensile forces on the lateral aspect of the femoral stem. A schematic of this is shown in Figure 54.

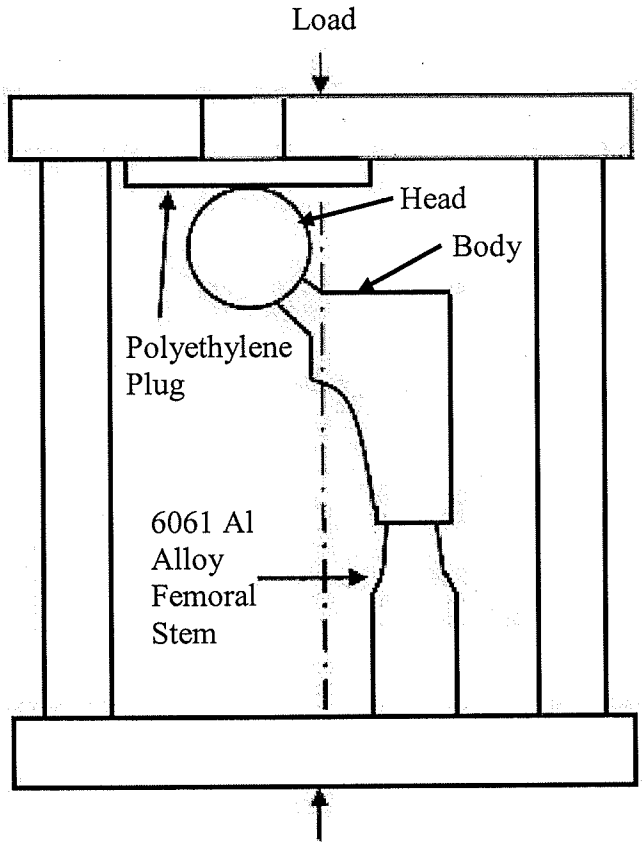

FIGURE 54: SCHEMATIC OF MODULAR HIP IMPLANT WITH THE 6061 AL ALLOY STEM IN COMPRESSION CAGE USING POLYETHYLENE PLUG

One test was done using this type of plug. However, due to the high loads that were used, the femoral head wore away most of the polyethylene and caused it to break apart. This created a similar situation as the last, where the femoral head was restricted and compressive forces were created. Since nothing was happening to the stem, the load was increased several times until the stem bent due to the load being too high.

Given that the cobalt-chrome head wore away the polyethylene, a new plug was fabricated out of the 6061 aluminum alloy. This was also done to prevent the femoral head from being restricted during fatigue testing. Eight tests were done using this type of plug, and in five of these cases the 6061 aluminum alloy stem fractured. Although the 6061 aluminum alloy plug was much more resilient than the polyethylene plug, the

cobalt-chrome head created an indentation and groove on the surface of the 6061 aluminum alloy plug in each test where this plug was used. Due to this indentation and the high forces being used in the test, the problem arose again where the femoral head was restricted and caused the entire implant to experience compressive forces. The 6061 aluminum alloy stem experienced very high cycles, but eventually fatigued and broke.

To solve this problem of restricting the femoral head, another plug was designed. Using the same 6061 aluminum alloy plug, a circular piece of Teflon was added to the surface. Oil was put in between the 6061 aluminum alloy plug and the Teflon to allow for easy sliding. A hole was cut through the centre of the Teflon piece to allow the femoral head to rest. A schematic of this is shown in Figure 55.

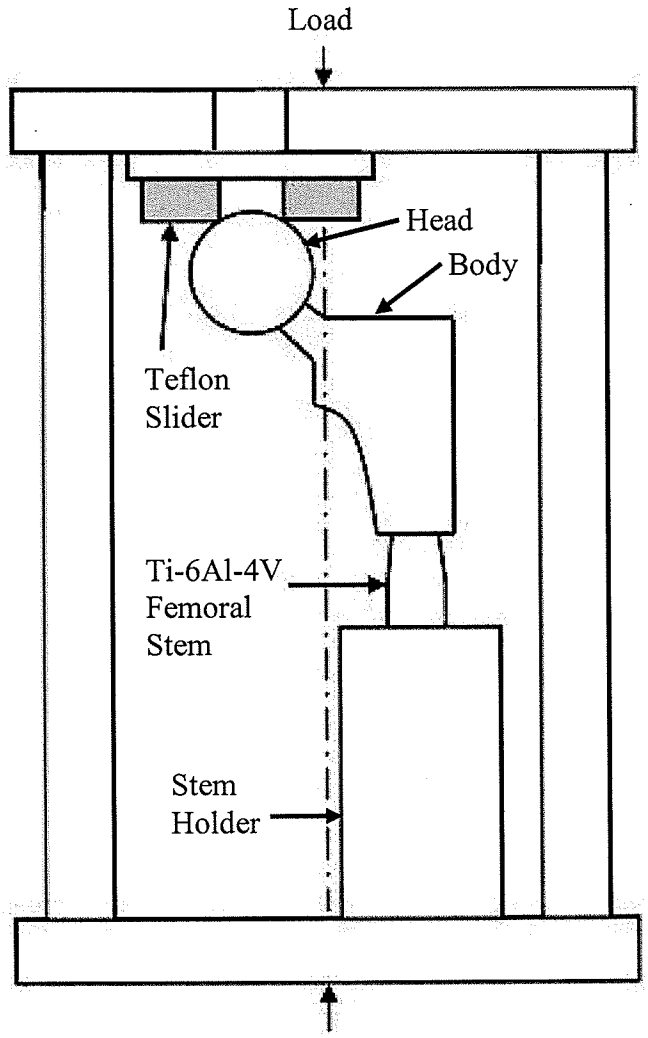

FIGURE 55: SCHEMATIC OF MODULAR HIP IMPLANT WITH TI-6AL-4V STEM IN COMPRESSION CAGE USING THE 6061 AL ALLOY PLUG WITH TEFLON SLIDER

The Teflon slider allowed the head to freely slide along the top circular plate of the compression cage, which is closest to in vivo conditions. Although this is not exactly the case in vivo, since the femoral head sits in the acetabulum, the testing may give slightly higher stresses than are present in vivo. Eight of the Al tests and all nine of the Ti-6Al-4V tests (tests13-29) used this type of plug. Figure 55 shows the final design that was used.

To prevent the body and stem from rotating during the fatigue tests, the stem was compressed into the body using the hydraulic cylinder of the fatigue machine. To determine what stress to apply to compress the stem in the body component, the following calculations were made.

If it is approximated that the diameter of the stem at the modular junction, d, is 0.0127 m (0.5 in), the area of the stem at the modular junction can be calculated as follows.

$$A = \frac{\pi d^2}{4} \tag{4.5}$$

$$= \frac{\pi(0.0127m)^2}{4}$$

$$= 1.27x10^{-4}\,m^2$$

If 137.9 MPa (20,000 psi) is taken, which is approximately half of the yield stress of the 6061 aluminum alloy and high enough to be significant, the force can be calculated as follows.

$$\sigma = \frac{F}{A} \tag{4.6}$$

$$137.9x10^{6}\,Pa = \frac{F}{1.27x10^{-4}\,m^2}$$

$$F = 17{,}513.3N$$

$$F = 17.5kN$$

Therefore, for fatigue tests 4-26 and test 29, the stem was compressed in the body component with 17.5 kN.

The detailed summary of all of the fatigue tests conducted is given in Table 12.

TABLE 12: SUMMARY OF RESULTS OF FATIGUE TESTING OF THE 6061 AL ALLOY STEMS AND TI-6AL-4V STEMS

	Type of Stem	Type of Plug	Loads Cycled Between, (kN)	Frequency, (Hz)	Cycles to Failure	Details
Test 1	Al 6061	-	-	-	-	Bending test only
Test 2	Al 6061	No Plug	0.4 – 4.4	10	403,287	Test was stopped because nothing was happening
Test 3	Al 6061	Poly Plug	0.4 – 4.4	10	337,453	Nothing happened, increased load
			0.6 – 6	10	111,706	Nothing happened, increased load
			0.8 – 8.8	10	144	Stem bent because load was too high
Test 4	Al 6061	Al Plug	0.74 – 7.4	5	< 100	Stem started to bend, reduced load
			0.7 – 7.0	5		Stem continued to bend, reduced load
			0.68 – 6.8	5		Stem continued to bend, stopped test
Test 5	Al 6061	No Plug	0.7 – 7.0	10	973,061	Jig broke and the rods were replaced
			0.68 – 6.8	10	-	Stem started to bend, reduced load
			0.6 – 6.0	10	-	Stem continued to bend, reduced load
			0.58 – 5.8	10	-	Stem continued to bend, stopped test
Test 6	Al 6061	Al Plug	0.46 – 4.6	10	550	Stem started to bend, reduced load
			0.4 – 4.0	10	382	Stem continued to bend, reduced load
			0.3 – 3.0	10	31,897	Stem continued to bend and cracked
Test 7	Al 6061	Al Plug	0.3 – 3.0	10	3,629,014	Nothing happened, increased load
			0.31 – 3.1	10	2,588,644	Nothing happened, increased load
			0.32 – 3.2	10	2,016,755	Stem broke
Test 8	Al 6061	Al Plug	0.34 – 3.4	10	927,799	Stem broke
Test 9	Al 6061	Al Plug	0.35 – 3.5	10	2,400,273	Stem broke
Test 10	Al 6061	Al Plug	0.37 – 3.7	10	989,313	Stem broke
Test 11	Al 6061	Al Plug	0.4 – 4.0	10	3,571,429	Nothing happened, increased load
			0.42 – 4.2	10	2,520,248	Nothing happened, increased load
			0.44 – 4.4	10	896,488	Nothing happened, increased load
			0.46 – 4.6	10	53,003	Nothing happened, increased load
			0.48 – 4.8	10	842,871	Nothing happened, increased load

			0.5 – 5.0	10	892,108	Nothing happened, increased load
			0.52 – 5.2	10	815,121	Nothing happened, increased load
			0.54 – 5.4	10	309,916	Stem broke
Test 12	Al 6061	Al Plug	0.55 – 5.5	10	810,807	Nothing happened, increased load
			0.56 – 5.6	10	176, 643	Nothing happened, increased load
			0.58 – 5.8	10	753,740	Nothing happened, increased load
			0.60 – 6.0	10	821,800	Nothing happened, increased load
			0.62 – 6.2	10	962,824	Nothing happened, increased load
			0.64 – 6.4	10	90,145	Stem bent because load was too high
Test 13	Al 6061	Al Plug/Teflon	0.62 - 6.2	10	< 20	Stem bent because load was too high
Test 14	Al 6061	Al Plug/Teflon	0.60 – 6.0	10	< 20	Stem bent because load was too high
Test 15	Al 6061	Al Plug/Teflon	0.5 – 5.0	10	< 20	Stem started to bend, reduced load
			0.44 – 4.4	10	<10	Stem continued to bend, stopped test
Test 16	Al 6061	Al Plug/Teflon	0.3 – 3.0	10	523,943	Stem broke
Test 17	Al 6061	Al Plug/Teflon	0.32 – 3.2	10	135,236	Stem broke
Test 18	Al 6061	Al Plug/Teflon	0.32 – 3.2	10	21,811	Stem broke
Test 19	Al 6061	Al Plug/Teflon	0.32 – 3.2	10	619,299	Stem broke
Test 20	Al 6061	Al Plug/Teflon	0.29 – 2.9	10	22,739	Stem broke
Test 21	Ti-6Al-4V	Al Plug/Teflon	0.95 – 9.5	5	4,206	Replaced rods, stem broke
Test 22	Ti-6Al-4V	Al Plug/Teflon	0.85 – 8.5	5	4,741	Stem broke
Test 23	Ti-6Al-4V	Al Plug/Teflon	0.6 – 6.0	5	75,964	Stem broke
Test 24	Ti-6Al-4V	Al Plug/Teflon	0.5 – 5.0	5	1,411,659	Stem broke
Test 25	Ti-6Al-4V	Al Plug/Teflon	0.5 – 5.0	5	138,345	Stem broke
Test 26	Ti-6Al-4V	Al Plug/Teflon	0.5 – 5.0	5	1,685,041	Stem broke
Test 27	Ti-6Al-4V	Al Plug/Teflon	0.5 – 5.0	5	246,299	Assembled using device, stem broke
Test 28	Ti-6Al-4V	Al Plug/Teflon	0.5 – 5.0	5	881,732	Assembled using device, stem broke
Test 29	Ti-6Al-4V	Al Plug/Teflon	0.5 – 5.0	5	93,552	Stem broke further down, holder worn

*GREYAREAS INDICATE THAT THE STEM FAILED BY FATIGUE

Table 12 shows that tests 7-11 and 16-20 actually failed by fatigue. Tests 7-11 were done using only the 6061 aluminum alloy plug to cover the hole in the top circular plate, whereas tests 16-20 use the 6061 aluminum alloy plug with the Teflon insert to allow for sliding of the femoral head. It can be seen from Table 12 that by using the 6061 aluminum alloy plug with the Teflon insert, the number of cycles to failure is significantly less than simply using the 6061 aluminum alloy plug.

After completing twenty fatigue tests using the 6061 aluminum alloy stems, it was determined that 3 kN was providing excellent fatigue results. Therefore, using the average yield stress determined in tensile testing for both materials, the following ratio was determined to obtain a starting point to test the Ti-6Al-4V stems.

$$\sigma_y \text{ (6061 Al alloy)} = 289.58\ MPa$$

$$\sigma_y \text{ (Ti-6Al-4V)} = 912.87\ MPa$$

$$\frac{3kN}{289.58\,MPa} = \frac{F}{912.87\,MPa} \tag{4.7}$$

$$F = 9.46kN$$

Using this information, the first Ti-6Al-4V fatigue test that was done in this study cycled between 0.95 – 9.5 kN. Since the stem broke after only 4,206 cycles, the load was gradually lowered to increase the number of cycles to failure. Table 12 shows that as the load decreases in tests 21-26, the number of cycles to failure increases. However, test 25 does not follow this trend. This is because when the modular stem was cut to fit into holder for the compression cage, it was cut slightly short. Therefore, a small piece was cut off and put at the bottom of the holder in order to raise the stem up to proper level. By doing this, the stem was not constrained the same way in the holder and this likely affected the results of the test.

From the data displayed in Table 12, the following stress versus number of cycles to failure (S-N) graphs were created.

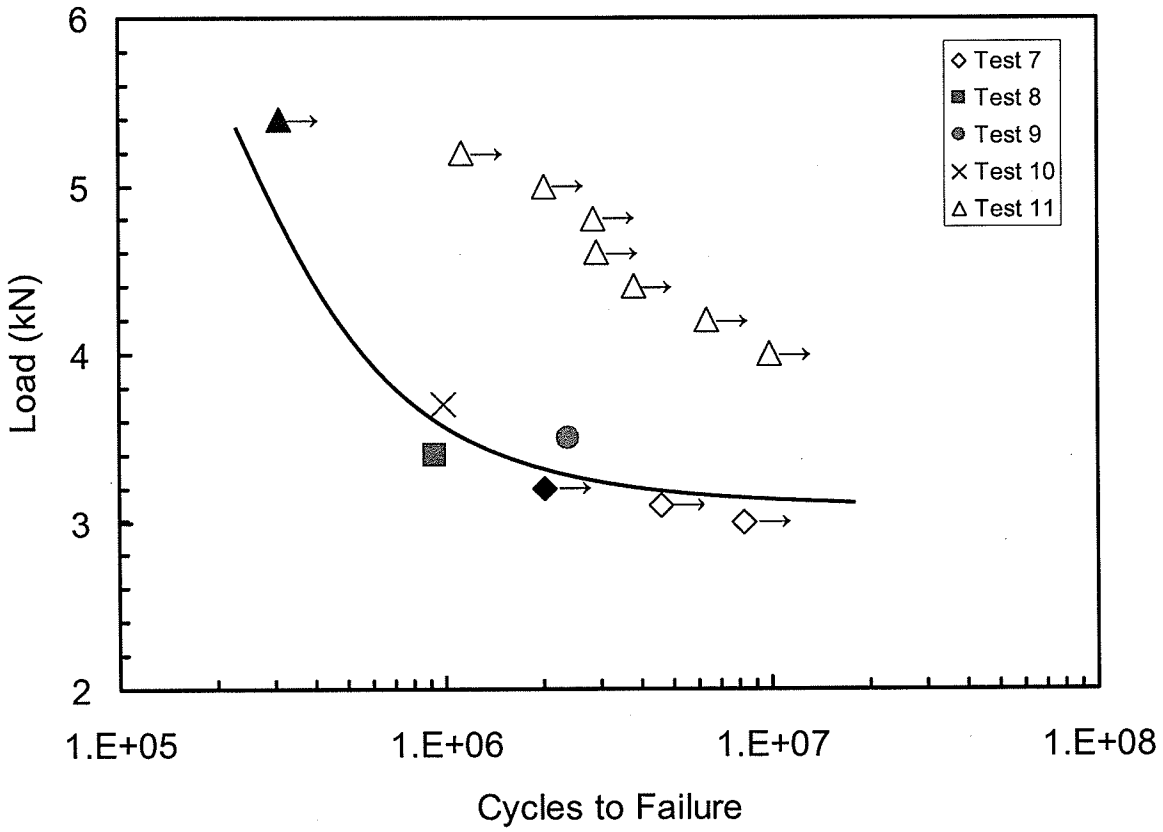

FIGURE 56: S-N CURVE (LOAD VS. CYCLES TO FAILURE) FOR THE 6061 AL ALLOY FATIGUE TESTS USING THE 6061 AL ALLOY PLUG ONLY

Figure 56 shows the fatigue results for tests 7-11, in which only the 6061 aluminum alloy plug was used to cover the hole in the top circular plate. The points that are filled in with colour each indicate a separate test, and indicate where the stem broke. The points that are not filled in with colour indicate how many cycles the stem underwent until the load was increased. These points continue to increase in load until the modular stem fractured by fatigue. Because of this, each of these successive points has an arrow

attached to it. This means that if the stem was set to fatigue only at that load, the stem would have gone through more cycles than recorded in the test. By looking at the points at which the stem broke, an S-N curve shows the trend from test to test. The overall trend is that when the stress applied decreases, the number of cycles that the implant can undergo before failure increases. In general, it can be seen that at lower loads, the femoral head could eventually slide on the 6061 aluminum alloy plug and cause the modular stem to fail. However, as the load increased to higher values, the femoral head could not slide due to the high frictional and compressive forces between the femoral head and the 6061 aluminum alloy plug. Thus, the entire implant experienced compression and the head was restricted in movement. This would explain why the stem underwent almost 10 million cycles before failure.

Fatigue data for all the 6061 aluminum alloy stems with the Teflon slider assembly is shown later in Figure 61 with the Ti-6Al-4V stems. The following S-N graph was obtained for only the Ti-6Al-4V fatigue tests using the 6061 aluminum alloy plug with the Teflon slider.

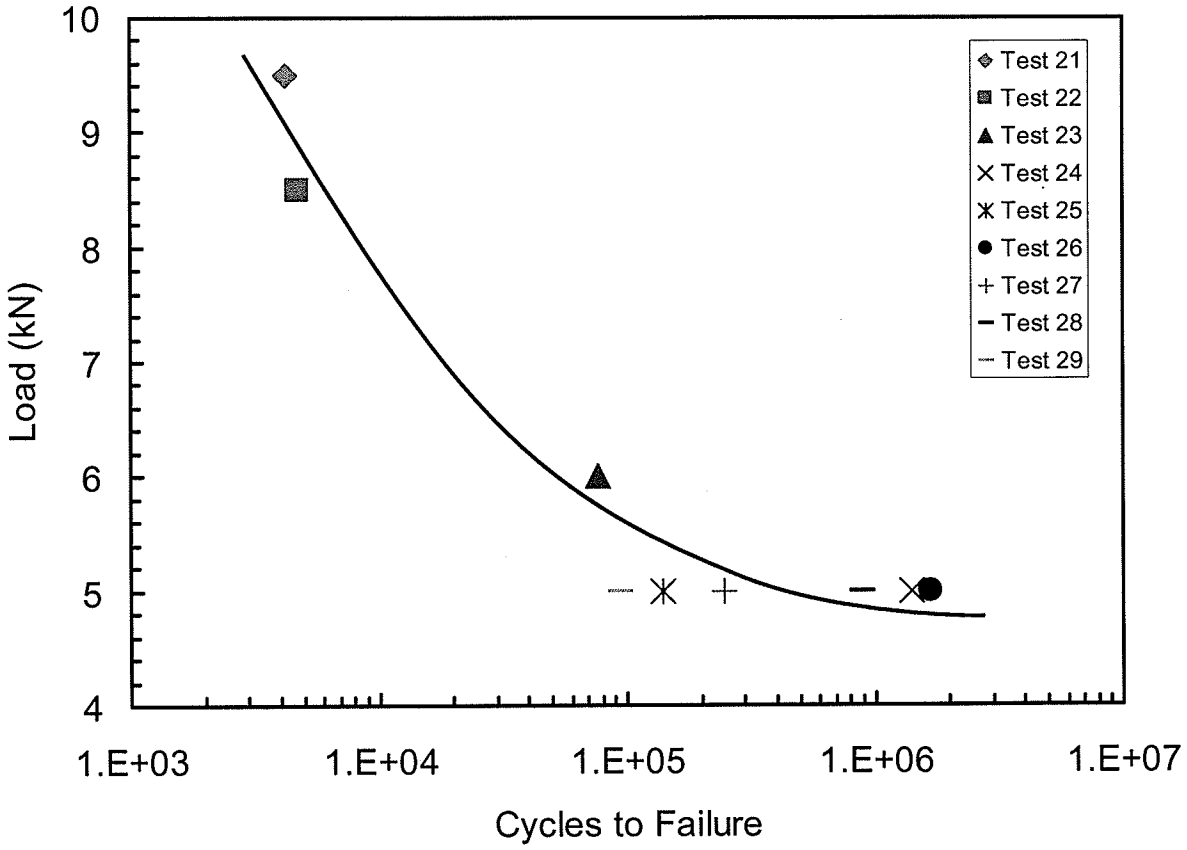

FIGURE 57: S-N CURVE (LOAD VS. CYCLES TO FAILURE) FOR TI-6AL-4V FATIGUE TESTS USING THE 6061 AL ALLOY PLUG WITH THE TEFLON SLIDER

Figure 57 shows the fatigue results for tests 21-29 for the Ti-6Al-4V stems. In these tests, the 6061 aluminum alloy plug with the Teflon slider was used to prevent any type of restriction to the femoral head. Each point on the graph indicates where the modular stem broke. Similar to Figure 57, an S-N curve can be drawn through the points which clearly shows the trend of the graph. As the stress applied decreases, the number of cycles that the implant can undergo before failure increases. As previously mentioned, the modular stem for test 25 was cut too short, and thus was likely not fixated properly in the holder in the compression cage. Due to this discrepancy, the recorded number of cycles to failure is inconsistent with the trend for tests 21-24 and test 26, and can be seen

clearly in Figure 57. Test 29 also deviates from the trend created by tests 21-24 and test 26. This is because the holder was worn out in the location where the modular stem was fixated and this was not noticed until after the test was completed. This caused the stem again to not be fixated properly and led to premature stem fracture.

Recall in section 4.2, it was found that the retrieved modular implants experienced approximately 4 million cycles before failure under a load of 2 kN in vivo. According to the S-N curve in Figure 57, it is estimated that under a 2 kN load, the implant should experience over 10 million cycles prior to failure. However, this is not the case. Therefore, there must be another mechanism causing the implants to fail by fatigue.

Tests 27 and 28 of the Ti-6Al-4V stems were also done using plug with the Teflon slider. As discussed earlier, the majority of the 6061 aluminum alloy stems and all the Ti-6Al-4V stems prior to test 27 were compressed into the body component with approximately 17.5 kN using the hydraulic cylinder of the fatigue machine. The modular stems for tests 27 and 28 were assembled into the body component using the proper surgical assembly tools. By doing this, the stem is pulled up into the body component and tensile forces are applied to the stem, rather than compressive forces like the other tests. This means that when the modular hip implant is assembled using the proper surgical tools, the stem will already have tensile forces acting on it.

Figure 54 shows that the number of cycles to failure recorded for the Ti-6Al-4V is lower for both tests 27 and 28 (246,299 and 881,732 cycles) comparing to tests 24 and 26 (1,411,659 and 1,685,041 cycles) at the same cyclic load. This indicates the difference between pulling the stem up into the body component with tensile forces versus pushing the stem up into the body component creating compressive forces on the stem. When the

load is applied to the femoral head of the implant, the lateral aspect of the stem is put into tension. If the stem has been pulled up into the body component, these tensile forces will add to the residual tensile forces that are already present from assembling the modular components. Therefore, an even greater tensile force is created at the lateral side of the modular junction. However, if the stem is compressed into the body, a portion of the tensile forces applied to the lateral side by the load at the femoral head will be counteracted by the residual compressive forces that are already present. Therefore, a lesser tensile force is experienced on the lateral side of the modular junction, causing the modular implant to undergo higher cycles to failure. Since this is a desired property of the modular implant, assembly by compressing the stem into the body component should be considered.

Another difference exists between the stems that were pulled up into the body component and the stems that were compressed during assembly. After fracture of the modular stems occurred, it was noticed that for tests 21-26, which have the stems compressed in the body, that the proximal side of the fracture surface was almost flush with the bottom of the body component. This means that crack initiation occurred directly at the interface between the stem and the body. This can be seen in Figure 58.

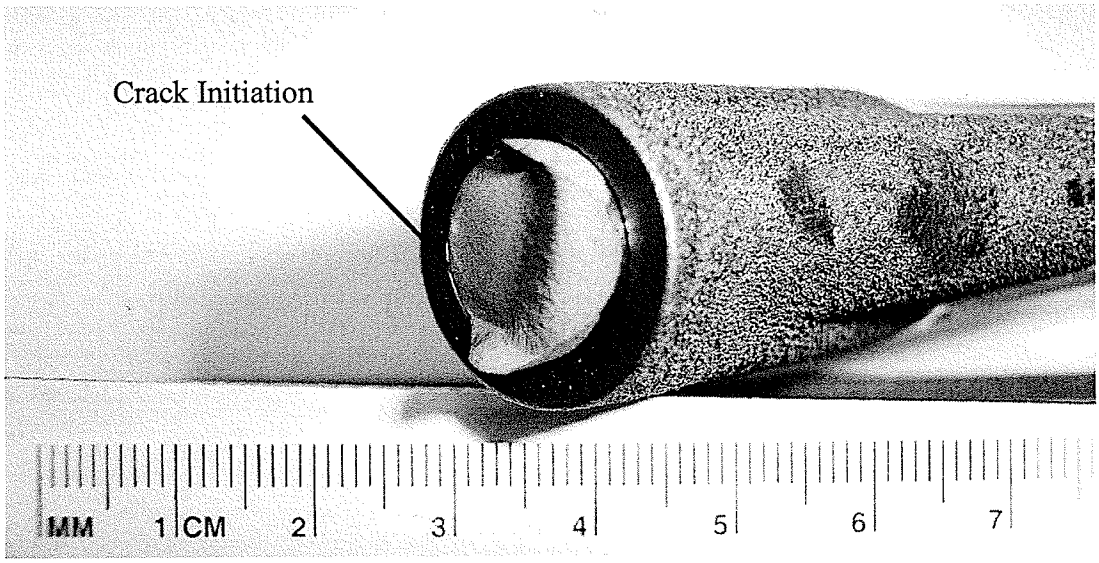

FIGURE 58: TYPICAL FRACTURE SURFACE FROM TI-6AL-4V FATIGUE TESTS 21-26, CRACK INITIATION IS INDICATED IN THE IMAGE

Figure 58 shows a typical fatigue fracture that occurred in the Ti-6Al-4V tests 21-26. It can be seen in this image that crack initiation occurred on the lateral side, and occurred almost flush with the bottom surface of the body component.

Contrary to this, for tests 27 and 28, which have Ti-6Al-4V stems that were pulled up into the body, the proximal side of the fracture surface did not have such a flat appearance. In fact, crack initiation did not occur directly at the interface between the stem and the body. It occurred at a location on the stem that was within the body component, a few millimeters above the interface. This can be seen in Figure 59.

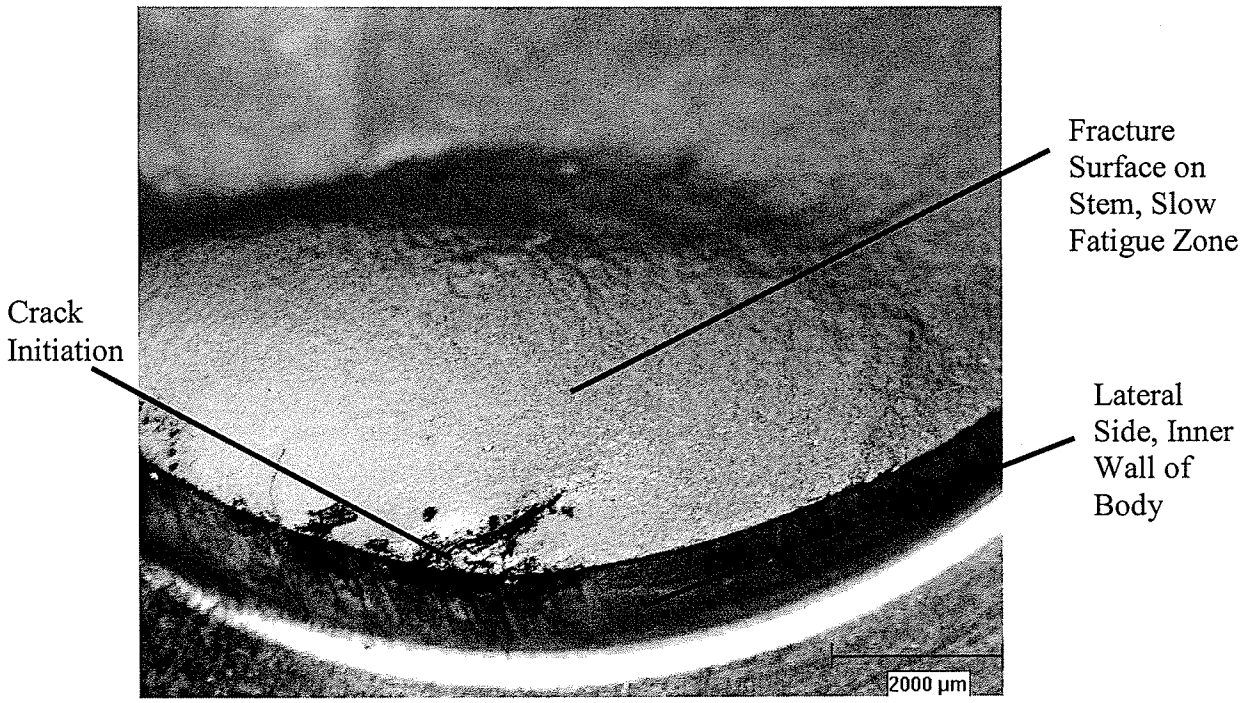

FIGURE 59: TYPICAL FRACTURE SURFACE FROM TI-6AL-4V FATIGUE TESTS 27 AND 28 TAKEN AT 10X, CRACK INITIATION IS TOWARDS THE BOTTOM OF THE SECTION

Figure 59 shows that crack initiation occurs towards the bottom of the section. Also, crack initiation of the stem occurring slightly above the bottom surface of the body component. According to the scale in the image, this crack started approximately 2 mm higher than the fracture surface of Figure 58. After the crack has formed, it then propagates downwards towards the interface and then finally breaks off. The fracture surface created in tests 27 and 28 are topographically exact replicas of the five fractured stems that occurred in vivo. For comparison purposes, an image of the fracture surface of implant #1 can be seen in Figure 60.

FIGURE 60: IMPLANT #1 - TYPICAL RETREIVED FRACTURE SURFACE FOR IMPLANTS STUDIED TAKEN AT 10X, CRACK INITIATION IS TOWARDS THE BOTTOM OF THE SECTION

Figure 60 shows a typical fracture surface of the implants studied. Crack initiation occurs towards the bottom of the section. It is shown that crack initiation also occurred slightly above the bottom surface of the body component. According to the scale, the crack also started approximately 2 mm higher than the fracture surface of Figure 58.

As shown, the fractures of tests 21-26 are different than the fractures of tests 27 and 28. This is because crack initiation always occurs at the point of highest stress. In tests 21-26, the residual stresses on the stem were in compression, thus counteracting the tensile forces applied. Therefore, the highest stresses created on the stem were the bending stresses created directly at the interface caused by the load applied to the femoral head. This explains why crack initiation occurred at this location. In tests 27 and 28, the residual stresses on the stem are tension. Therefore, when the load is applied to the femoral head, the highest stresses occur on the stem within the body component. This

explains why crack initiation occurs slightly above the modular junction. Once the crack is initiated, the material at that location is relieved of the tensile stresses that were once there. This causes the crack to propagate to the area with the next highest stresses, which would be towards the modular junction. This creates the uneven fracture surface that was noted on the stems.

The following figure shows the trends of all of the tests that were successful in obtaining a fractured stem and that utilized the 6061 aluminum alloy plug with the Teflon slider. The 6061 aluminum alloy stems and the Ti-6Al-4V stems have been separated for comparison.

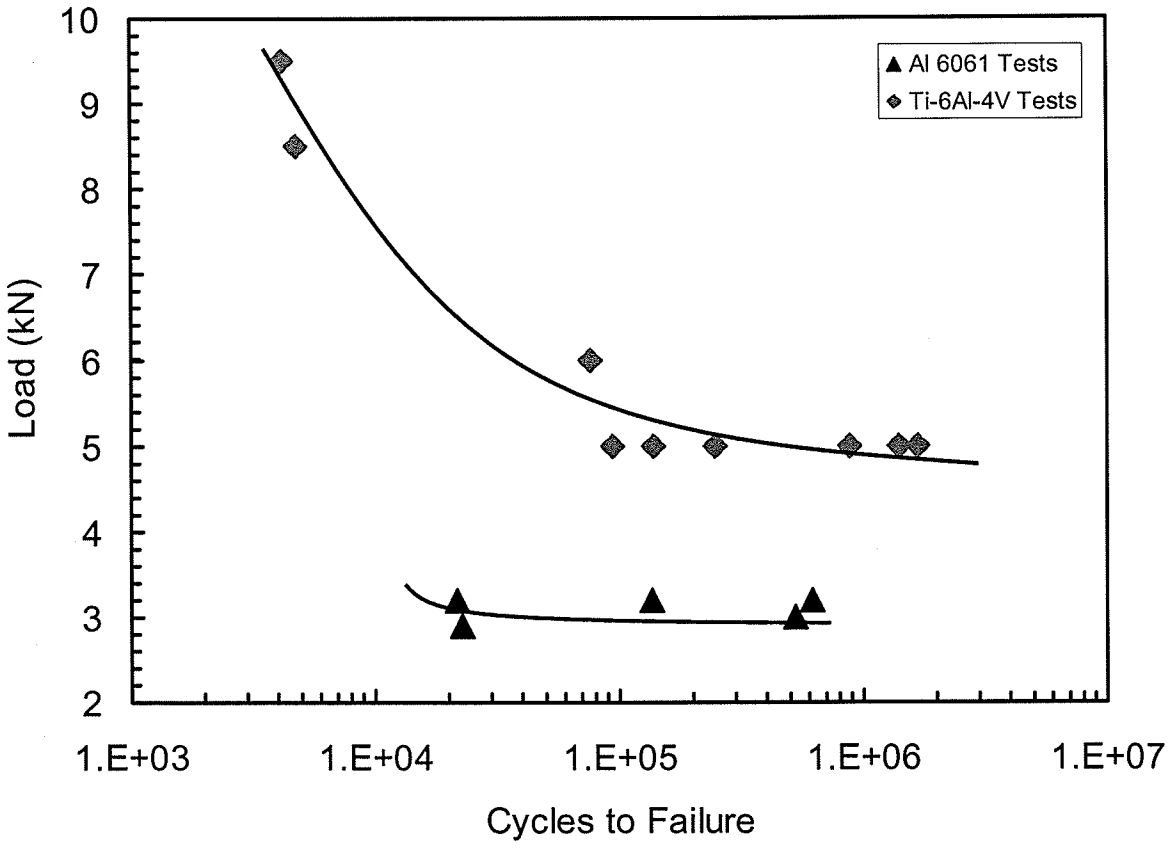

FIGURE 61: S-N CURVE (LOAD VS. CYCLES TO FAILURE) FOR ALL TESTS USING THE 6061 AL ALLOY PLUG WITH THE TEFLON SLIDER

Figure 61 shows the S-N curves created with the fatigue test results of these tests. It can be seen that the 6061 aluminum alloy stems had comparable cycles to failure at 3 kN to that of the Ti-6Al-4V stems at 5 kN. It was initially thought that the number of cycles to failure that the stem would be able to withstand would be dependent on the material's tensile strength [18]. However, as found in the tensile tests conducted, the average tensile strength for the 6061 aluminum alloy was approximately 290 MPa (42 ksi) and the tensile strength for Ti-6Al-4V was 913 MPa (132 ksi). Therefore, since the tensile strength of Ti-6Al-4V was approximately 3 times that of the 6061 aluminum alloy, then according to equation 4.6, the load that the stem can withstand giving comparable cycles to failure should be approximately 3 times as well. The tests that were cycling at 5 kN were only at a 1.7 times load increase than that of the tests that were cycling at 3 kN. This value is almost half of what was predicted. Thus, the failure of the stem must be dependent on another material property.

The following relationship exists for stress as well:

$$\sigma = E\varepsilon \tag{4.8}$$

where ε is the amount of strain. This equation shows that for a given strain, ε, the stress is proportional to the modulus of elasticity. In this equation, the variable that is dependent on the type of material is the modulus of elasticity. Referring back to Table 2 and Table 5, the modulus of elasticity for the 6061 aluminum alloy was approximately 69 GPa (10 x 10^6 psi) and the modulus of elasticity for Ti-6Al-4V was 120 GPa (17.4 x 10^6 psi). By comparing these values, the modulus of elasticity for Ti-6Al-4V is approximately 1.7 times that of the 6061 aluminum alloy. Looking at the fatigue data that was collected, this would indicate that the stress and failure of the implant is dependent on the modulus of

elasticity of the material used for the stem and not the tensile stress of the material. Therefore, it may be beneficial to utilize an implant composed of a material with a higher modular of elasticity, such as stainless steel or a cobalt-chrome alloy. Although these materials may not be as biocompatible as titanium, this problem would be solved if the surface of these implants was coated with titanium.

Another factor that contributes to the tensile forces on the lateral side of the modular stem is the grinding stresses that are applied to the stem during the fabrication process. When the stems are machined, a residual tensile force can be left on the surface of the stem. This can be seen in Figure 62.

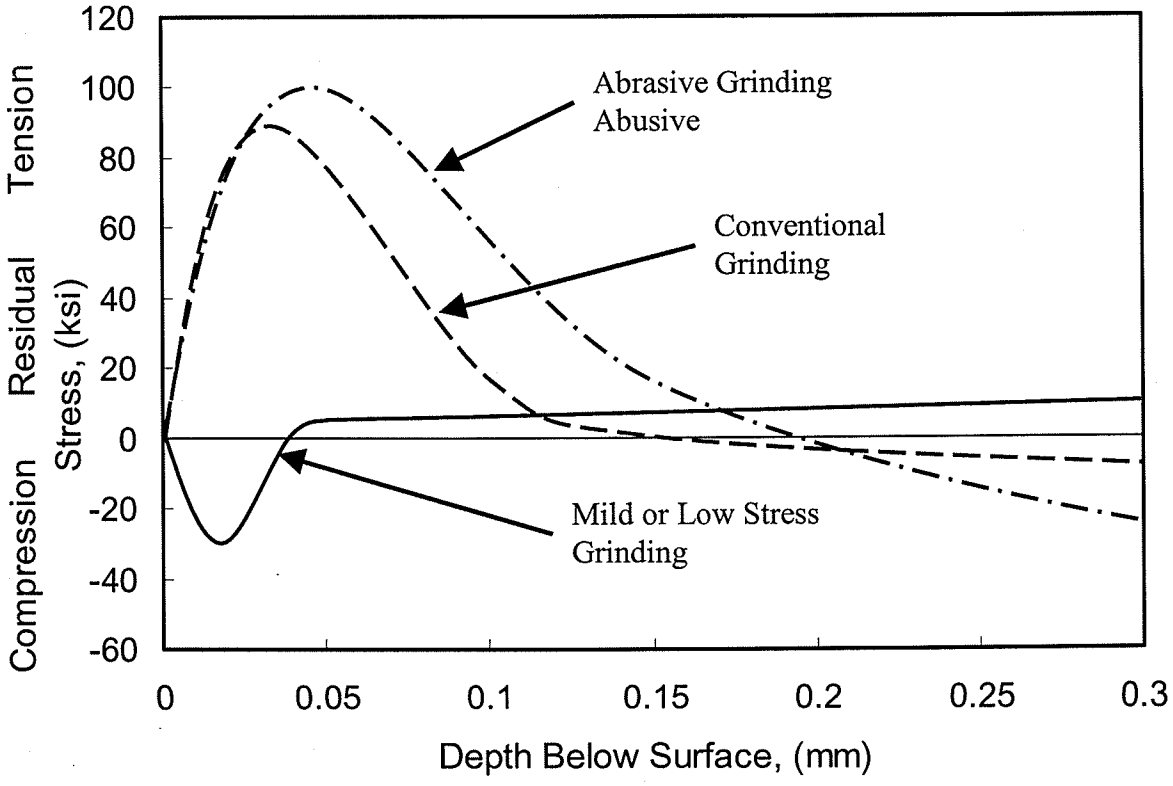

FIGURE 62: TYPICAL GRINDING STRESSES PRODUCED BY SURFACE GRINDING [32]

Figure 62 shows the magnitude of stresses that can be created on the surface of the modular stem by grinding. If mild or low stress grinding was not employed during the fabrication process, at less than 0.05 mm from the surface of the stem, there could be up to 620 MPa (90 ksi) of residual tensile stresses. This amount is very significant. As found before in the finite element analysis, the stress on the lateral side at the modular junction was approximately 487 MPa on average. Therefore, if conventional grinding was used, the stress would be approximately 1107 MPa, or 1 GPa, on the lateral side at this junction. This value is higher than the fatigue strength or limit at 500,000+ cycles, the yield stress, and the ultimate tensile strength for Ti-6Al-4V, and does not even include the extra residual tensile stress that is added from pulling the stem up into the body component. However, by looking at Figure 62, if mild or low stress grinding is used on the modular stem during the fabrication process, then this residual stress becomes 207 MPa (30 ksi) in compression at a distance of less than 0.05 mm from the surface. This would counteract the stresses created in vivo and thus would create a lower stress at the modular junction. Therefore, it would be very important to ensure that the modular stems are machined using mild or low stress grinding processes.

Once all the Ti-6Al-4V fatigue tests were complete, a typical fracture surface was chosen for inspection under the SEM. The stem that was chosen was from Test 27, where the stem was assembled into the body component with the proper surgical tools. Since the fracture surface had not been exposed to corrosive extracellular fluids and crevice corrosion in vivo, the presence of a TiO_2 layer would be absent, and thus striations and undamaged areas should be clearly visible under the SEM.

The rapid fracture area was examined first. An image of this can be seen in Figure 63.

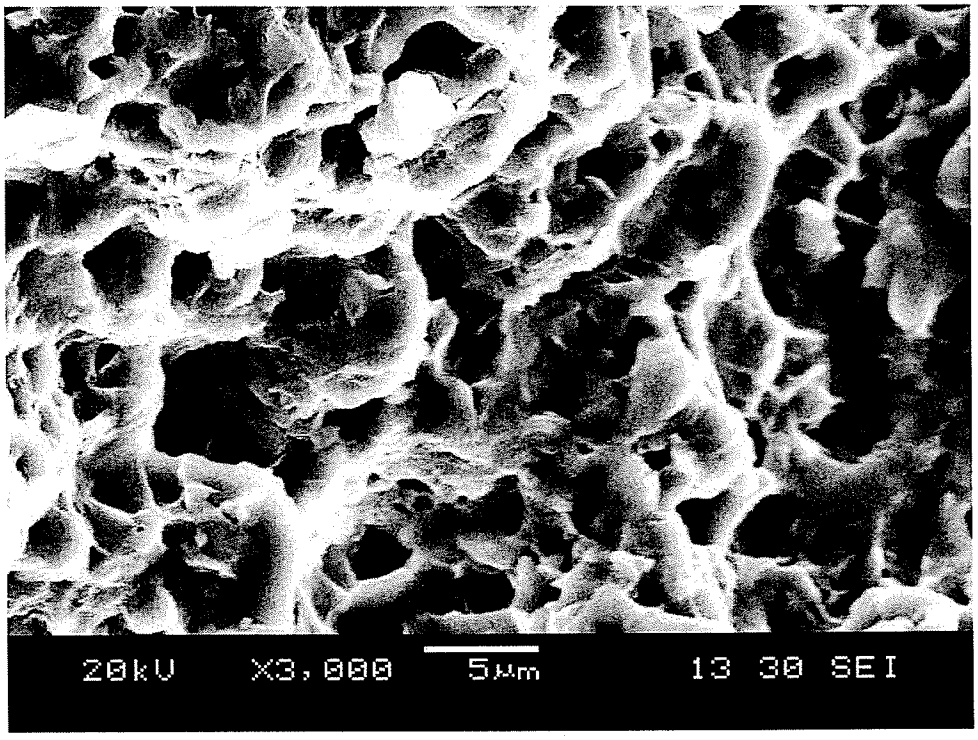

FIGURE 63: SEM IMAGE OF TI-6AL-4V FATIGUE TEST 27, RAPID FRACTURE ZONE TAKEN AT 3000X

Figure 63 shows an SEM image of the rapid fracture zone. This image clearly indicates a ductile fracture due to the presence of cups and cones. Unlike Figure 32, there is no damage in this image and all features are very clear and distinct. The slow fatigue area was then examined under the SEM for striations. An image of this is seen in Figure 64.

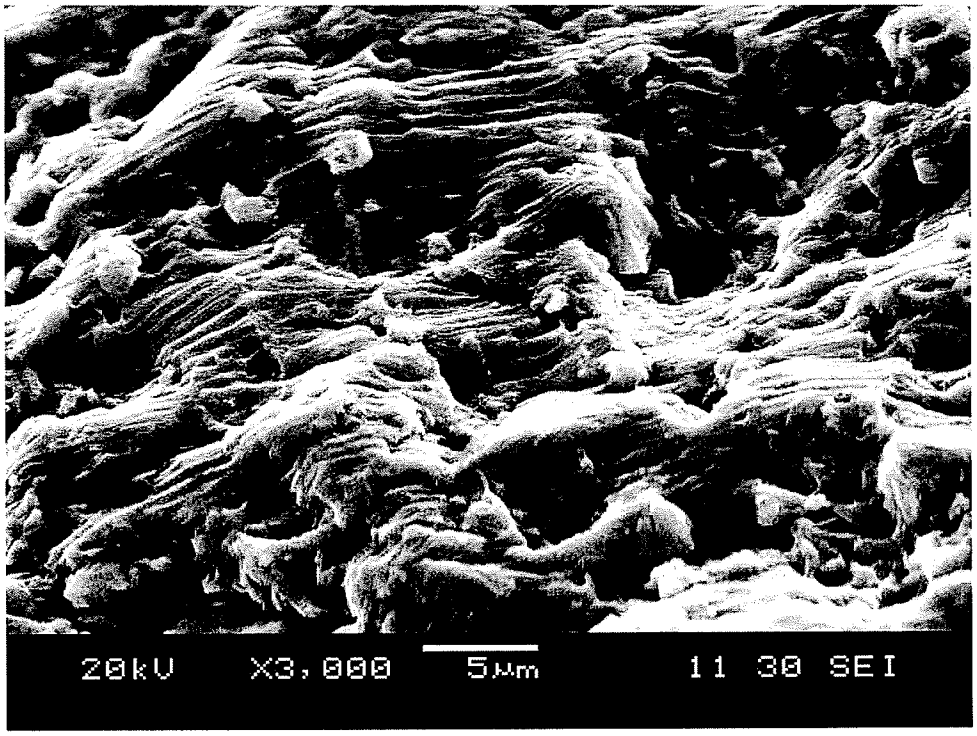

FIGURE 64: SEM IMAGE OF TI-6AL-4V FATIGUE TEST 27, SLOW FATIGUE ZONE TAKEN AT 3000X

Figure 64 shows an SEM image of the slow fatigue zone. Since there is no TiO_2 layer present, the striations on the surface are clear to see, which are perpendicular to the direction of crack propagation. Each striation, or ripple, indicates every time the crack propagated further after crack initiation. According to the scale, each striation is approximately 1 micron apart. Thus, the crack tip propagated approximately 1 micron at a time before it became a rapid ductile failure. It can be seen in Figure 64 that the fracture surface is not flat. This is due to the toughness of the material.

In summary, fatigue testing showed that fracture continued to occur at the modular junction, with crack initiation occurring on the lateral side of the stem. It is postulated that if the stem was compressed in the body component rather than pulled up, the residual stress would be in compression, thus lowering the stress at the site of crack

initiation. It is also suggested that if the modular stems were machined using mild or low stress grinding processes, the residual tensile stresses left near the surface of the stem would be significantly less than other grinding processes. Both of these predictions would considerably lower stresses at the modular junction and increase the life of the implant in vivo.

CHAPTER 5

CONCLUSIONS

Retrieved fractured Ti-6Al-4V modular hip stems were examined to become more familiar with the causes of failure and to gain a better understanding of utilizing them in patients in order to mitigate future fractures in vivo. In this study, microscopic analysis was performed to analyze the fracture surfaces of the failed stems and to determine if there were any major defects contributing to failure. Macroscopic analysis, which included radiographic analysis, implant inspection, and chart review, was done to examine the effects of osseointegration, bone grafting, and patient characteristics. Finite element analysis was performed to confirm the highest point of stress in the modular implant, to obtain an approximation of these stresses, and to determine the effects of the addition of a medial bone support. Finally, mechanical testing of the 6061 aluminum alloy and Ti-6Al-4V stems was done to determine tensile, hardness, and fatigue properties. The following conclusions have been made from this study:

1. Fracture of the modular stem occurs near the modular junction. This is because there are stress risers at the junction. Since the lateral side of the stem experiences tension and the medial side undergoes compression when a load is applied to the femoral head, crack initiates on the lateral side.

2. Microscopic analysis showed evidence of a corrosion byproduct, possibly TiO_2, on the fracture surface. A TiO_2 layer on the fracture surface could further

accelerate crack propagation since TiO_2 has a slightly lower density than Ti-6Al-4V. However, crack propagation occupies only the final few percentage of the fatigue life and thus has little effect on the total life of the implant. Therefore, this is not the mechanism that causes implant failure.

3. Microscopic analysis showed no evidence that stress corrosion cracking, corrosion (i.e. crevice corrosion, corrosion fatigue, pitting corrosion), major material defects (i.e. high inclusion content, porosity), or any other defects contributed to implant failure. There was also no evidence of a notch created on the stem from assembly with the body component.

4. Radiographic and retrieval analysis of the five studied stems showed that in all cases, the stem was fixed distally. Radiographic analysis indicated that medial bone, though varying in percentage and bone ingrowth, was always present and in four out of five cases, was continuous across the modular junction. However, visual inspection was not in agreement with this, since radiographic analysis is not exact and only suggests certain findings, which needs to be confirmed or refuted by visual inspection of the implant components. Visual inspection indicated that there was no medial osseointegration. Lateral bone at the body was only present in four cases and varied in percentage, and was only continuous across the modular junction in two cases. There was no lateral bony ingrowth at the body in all five cases. If proper lateral bone support is present and osseointegration has occurred on both sides of the implant, the lateral side of the

implant may be supported better and may not experience as high of a tensile force.

5. Finite element analysis confirmed that the highest point of stress on the modular implant when loaded is on the lateral side of the modular junction and is estimated to be 487 MPa at loads seen with normal activities. This is slightly higher than the fatigue life at 500,000 cycles and higher of the Ti-6Al-4V modular stem and may be a factor in failure of the implant. FEA also showed that if a proper medial bone support is present that has osseointegrated into the modular implant, this tensile stress on the lateral side will be significantly reduced to approximately 60 MPa.

6. Tensile tests and hardness tests of both the 6061 aluminum alloy and Ti-6Al-4V materials that were used in this study showed expected mechanical properties. Therefore, it is confirmed that the modular stems were not fracturing due to major defects in the material.

7. Fatigue testing of the 6061 aluminum alloy and Ti-6Al-4V modular stems followed expected stress vs. number of cycles to failure (S-N) trends and showed that fracture continued to occur at the modular junction, with crack initiation occurring on the lateral side of the modular stem.

8. Fatigue testing of the Ti-6Al-4V modular stems showed that when the modular stem was compressed into the body component rather than the conventional intra-operative method of pulling it up into the body, residual stresses on the stem would be in compression, thus lowering the stress at the site of crack initiation. Normal assembly of the implant, which involves the modular stem being pulled up into the body component, creates residual tensile stresses within the stem. This results in a shorter fatigue life.

9. Fatigue testing showed that fracture of the implant may be dependent on the modulus of elasticity rather than the tensile strength of the material. If this is the case, it would be beneficial to utilize an implant composed of a material with a higher modulus of elasticity, such as stainless steel or a cobalt-chrome alloy. These implant alloys do not encourage osseointegration as do titanium alloys, and thus it may be advantageous to coat the surface of non-titanium implants with titanium.

CHAPTER 6

RECOMMENDATIONS FOR FUTURE WORK

For future work done in this developing area of research, the following suggestions can be made:

1. The differences between pulling the modular stem up into the body component versus compressing it into the body should be investigated further. It would be important to quantify the effect of pulling and compressing the modular stem into the body component at different forces.

2. Although approximately 4,893 N (1,100 lbs) was said to be the force that the modular stem was pulled up into the body component, it would be important to utilize strain gauges on the modular stem to confirm this value.

3. Further investigating the residual stresses left on the surface of the modular stem due to grinding during the fabrication process would be essential.

REFERENCES

[1] E. N. Marieb and K. Hoehn, *Human Anatomy & Physiology, 7th Edition*. San Francisco, CA: Pearson Education, Inc., 2007, pp. 237-241.

[2] R. D. Crowninshield, W. J. Maloney, D. H. Wentz, and D. L. Levine. "The Role of Proximal Femoral Support in Stress Development Within Hip Prostheses," *Clinical Orthopaedics and Related Research*, vol. 420, pp. 176-180, 2004.

[3] Canadian Institute for Health Information. *Waiting for Health Care in Canada: What We Know and What We Don't Know*. ISBN 1-55392-784-2, March 7, 2006.

[4] Manitoba Government News Release. *Health Minister Announces Strategy To Address Long Wait Times For Hip and Knee Operations*. November 2, 2005

[5] J. Cluett, "*Hip Replacement Implant Options*" [Online]. 2007. Available: http://orthopedics.about.com/od/hipkneereplacement/a/implants.htm [October 20, 2007].

[6] Stryker, "*Joint Replacements*" [Online]. 2005. Available: http://www.stryker.com/jointreplacements/sites/trident/healthcare/alumceramics/php [February 2005].

[7] W. D. Callister, Jr., *Materials Science and Engineering: An Introduction*. United States of America: John Wiley & Sons, Inc., 2000, pp. 169-172, 373-375, 749-755.

[8] J. C. J. Webb and R. F. Spencer. "The Role of Polymethylmethacrylate Bone Cement in Modern Orthopaedic Surgery," *The Journal of Bone & Joint Surgery*, vol. 89-B, pp. 851-857, 2007.

[9] H. E. Boyer, *Atlas of Fatigue Curves*. Metals Park, Ohio: American Society for Metals, 1986, pp. 432-436, 438-439, 443.

[10] V. C. Mow and R. Huiskes, *Basic Orthopaedic Biomechanics and Mechano-Biology*. Philadelphia, PA: Lippincott Williams & Wilkins, 2005, pp. 497-511.

[11] S. Affatato, R. Torrecillas, P. Taddei, M. Rocchi, C. Fagnano, G. Ciapetti, and A. Toni. "Advanced Nanocomposite Materials for Orthopaedic Applications. I. A Long-Term In Vitro Wear Study of Zirconia-Toughened Alumina," *Journal of Biomedical Materials Research Part B: Applied Biomaterials*, pp. 76-82, 2005.

[12] ASTM International Std. F 1472 – 02a, *Standard Specification for Wrought Titanium-6Aluminum-4Vanadium Alloy for Surgical Implant Applications (UNS R56400)*, ASTM International, 2002.

[13] J. J. Jacobs, N. J. Hallab, R. M. Urban, and M. A. Wimmer. "Wear Particles", *The Journal of Bone & Joint Surgery*, vol. 88, pp. 99-102, 2006.

[14] A. Sargeant, T. Goswami, and M. Swank. "Ion Concentrations From Hip Implants," *The Journal of Surgical Orthopaedic Advances*, vol. 15, pp. 113-114, 2006.

[15] V. Milavec-Puretic, D. Orlic, and A. Marusic. "Sensitivity to Metals in 40 Patients with Failed Hip Endoprosthesis," Archives of Orthopaedic and Trauma Surgery, vol. 117, pp. 383-386, 1998.

[16] C. A. Busch, M. N. Charles, C. M. Haydon, R. B. Bourne, C. H. Rorabeck, S. J. MacDonald, and R. W. McCalden. "Fracture of Distally-Fixed Femoral Stems After Revision Arthroplasty," *The Journal of Bone & Joint Surgery*, vol. 87-B, pp. 1333-1336, 2005.

[17] A. G. Della Valle, B. Becksac, J. Anderson, T. Wright, B. Nestor, P. M. Pellicci, and E. A. Salvati. "Late Fatigue Fracture of a Modern Cemented Forged Cobalt Chrome Stem for Total Hip Arthroplasty," *The Journal of Arthroplasty*, vol. 20, pp. 1084-1088, 2005.

[18] I. LeMay, *Principles of Mechanical Metallurgy*. New York, NY: Elsevier North Holland, Inc., 1981, pp. 254-258, 308.

[19] C. Laird and G. Smith. "Initial Stages in Damage in High Stress Fatigue in Some Pure Metals," *Philosophical Magazine*, vol. 8, pp. 1945-1963, 1963.

[20] C. A. Engh, P. Massin, and K. E. Suthers. "Roentgenographic Assessment of the Biologic Fixation of Porous-Surfaced Femoral Components," *Clinical Orthopaedics and Related Research*, vol. 257, pp. 107-128, 1990.

[21] C. Ruff, B. Holt, and E. Trinkaus. "Who's Afraid of the Big Bad Wolff?: "Wolff's Law" and Bone Functional Adaptation," *American Journal of Physical Anthropology*, vol. 129, pp. 484-498, 2006.

[22] Zimmer. *ZMR Porous Revision Hip Prosthesis: Surgical Technique for Revision Hip Arthroplasty.*

[23] Personal Communication, 2008: Jeff Dickerson, Product Manager for Revision Hips, U.S. Hip Marketing, Zimmer, Inc. (574) 371-8620, (574) 527-0345 (cell), jeff.dickerson@zimmer.com

[24] ASM Handbook Committee, R. F. Mehl (Chairman of all Volume 7 Committees), *ASM Metals Handbook: Volume 7, Atlas of Microstructures of Industrial Alloys, 8th Edition*. United States of America: American Society for Metals, 1972, pp. 322, 327, 330.

[25] "Handbook of Analytical Methods, Materials Evaluation and Engineering, Inc., Energy Dispersive Spectroscopy – Description of Technique" [Online], 2000. Available: http://www.mee-inc.com/eds.html [May 7, 2008].

[26] ASTM International. *Annual Book of ASTM Standards 2005, Section Three: Metals Test Methods And Analytical Procedures, Volume 03.01, Metals-Mechanical Testing; Elevated and Low-Temperature Tests; Metallography, 9th Edition*. United States of America: ASTM International, 2005, pp. 26, 62-79.

[27] ASM International Handbook Committee. *Metals Handbook (Volume 2), Properties and Selection: Nonferrous Alloys and Special-Purpose Materials*. United States of America: ASM International, 1990, pp. 26, 102-103.

[28] ASTM International Std. F 1612 – 95, *Standard Practice for Cyclic Fatigue Testing of Metallic Stemmed Hip Arthroplasty Femoral Components with Torsion*, ASTM International, 2000.

[29] D. R. Lide. *Handbook of Chemistry and Physics, 83rd Edition*. Boca Raton: CRC Press, 2002-2003, pp. 4-91.

[30] M. G. Fontana. *Corrosion Engineering, 3rd Edition.* United States of America: McGraw-Hill, Inc., 1986, pp. 115.

[31] J. S. Gottschall, R. Kram. "Ground Reaction Forces During Downhill and Uphill Running," *The Journal of Biomechanics*, vol. 38, pp. 445-452, 2004.

[32] E. P. DeGarmo, J. T. Black, R. A. Kohser, and B. E. Klamecki. *Materials and Processes in Manufacturing, 9th Edition*. United States of America: John Wiley & Sons, Inc., 2003, pp. 664.

APPENDIX A

DIMENSIONAL DRAWINGS OF THE COMPRESSION CAGE ASSEMBLY

BILL OF MATERIALS	
QTY	ITEM DESCRIPTION
4	ROD
2	CIRCULAR PLATE
2	RECTANGULAR PLATE
16	3/4" NUT
2	1" NUT
1	GRIP SECTION

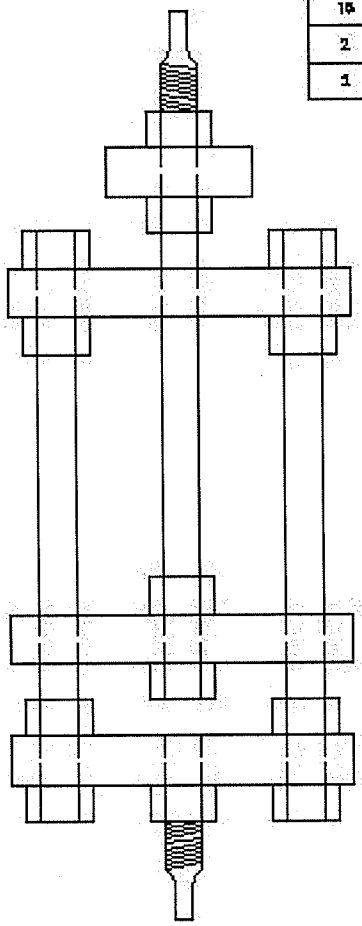

The University of Manitoba
Department of Mechanical Engineering

COMPRESSION CAGE ASSEMBLY

SIZE	FSCM NO.	DWG NO.	REV
A			

SCALE 1:3 SHEET 1 of 4

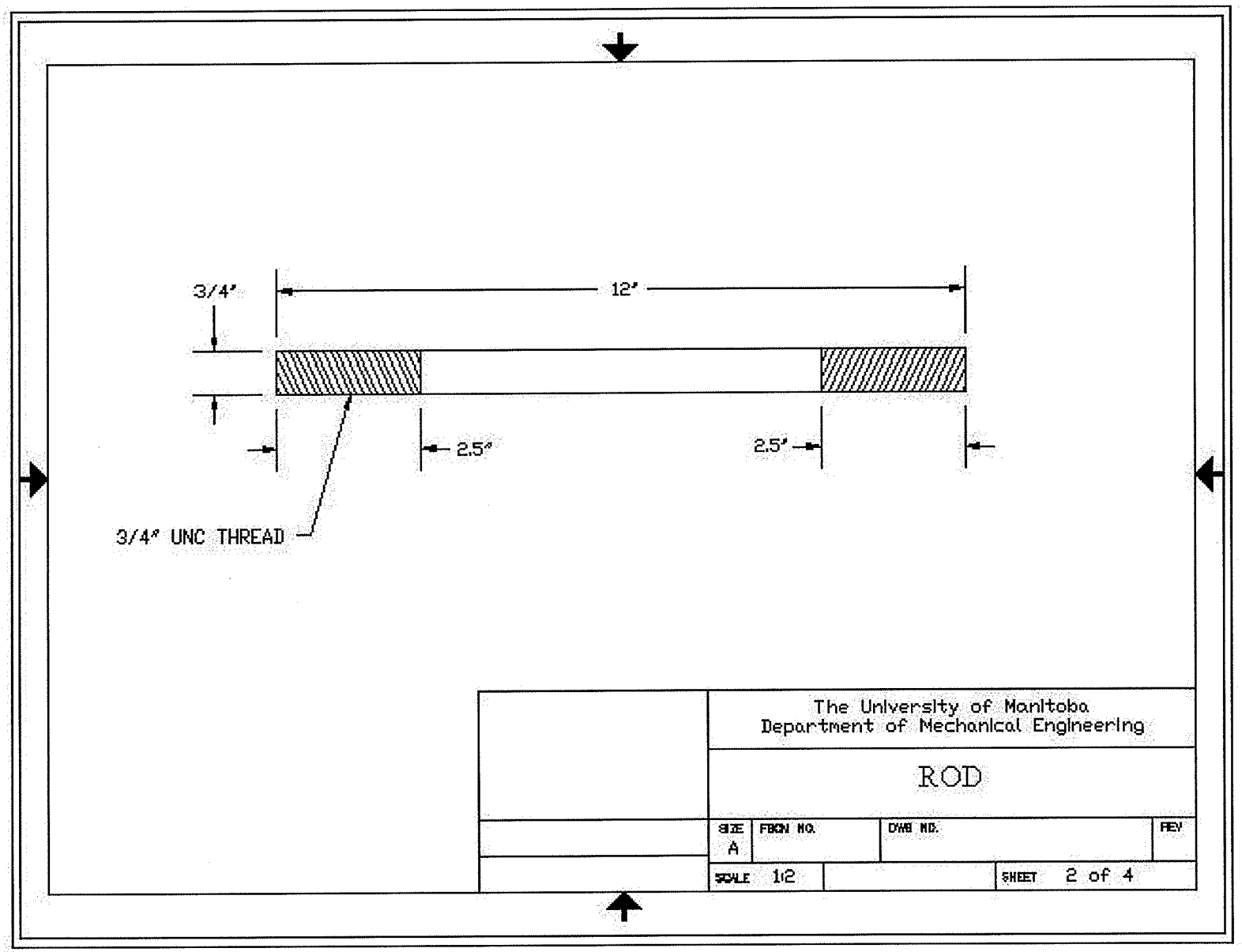
3/4"
12"
2.5"
2.5"
3/4" UNC THREAD
The University of Manitoba
Department of Mechanical Engineering
ROD
SIZE
A
FSCM NO.
DWG NO.
REV
SCALE 1:2
SHEET 2 of 4

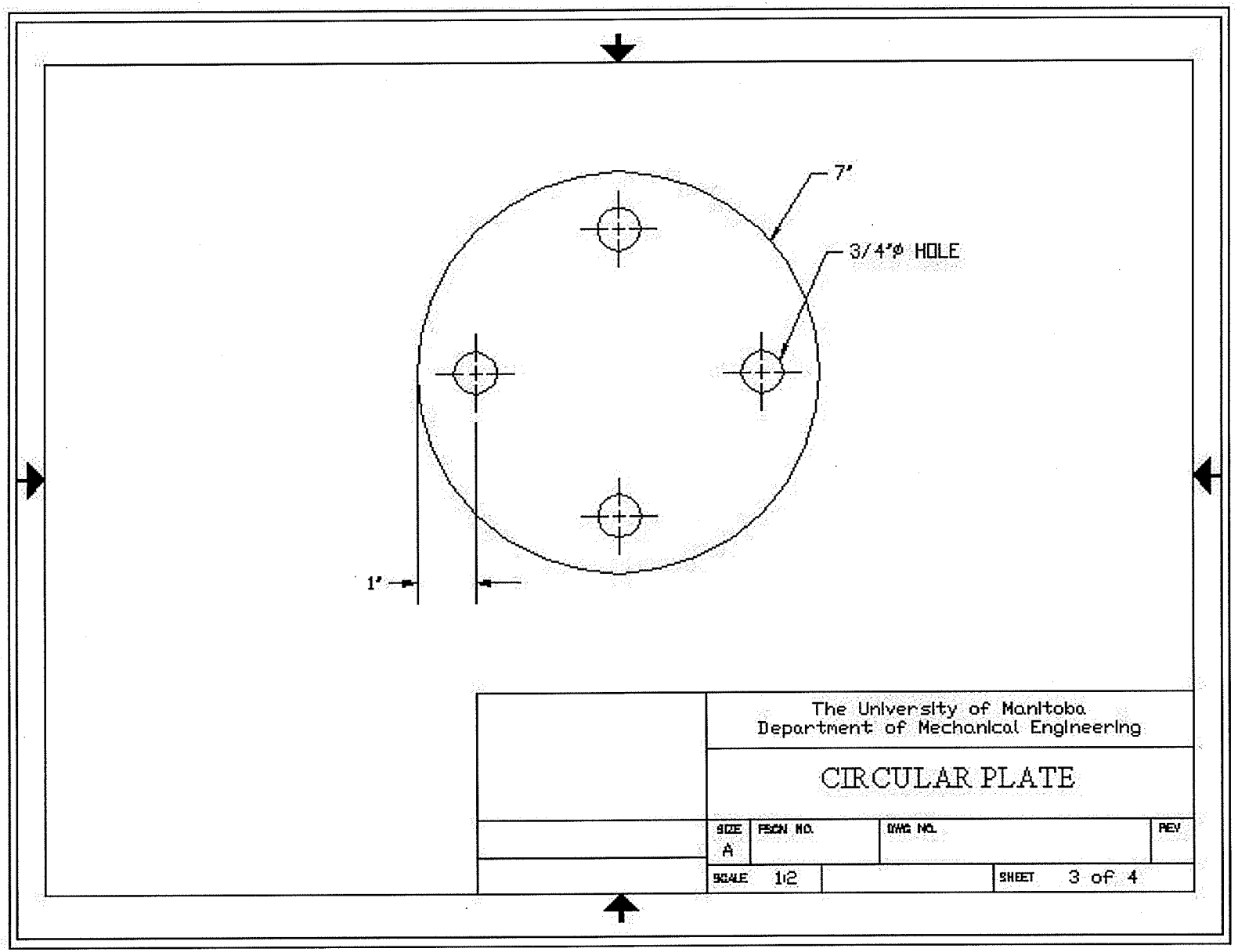
7"
3/4"ø HOLE
1"
The University of Manitoba
Department of Mechanical Engineering
CIRCULAR PLATE
SIZE
A
FSCM NO.
DWG NO.
REV
SCALE 1:2
SHEET 3 of 4

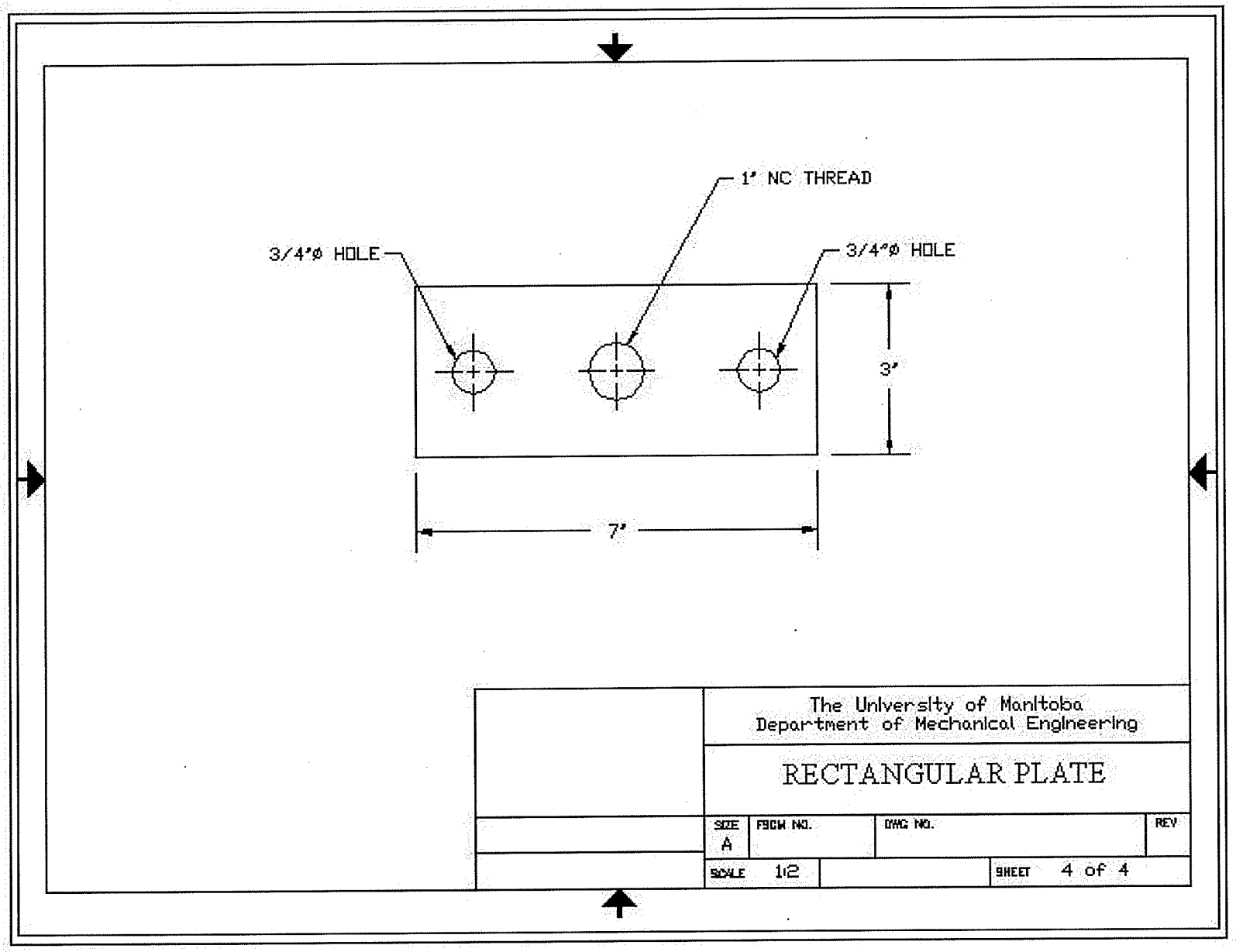
1" NC THREAD
3/4"ø HOLE
3/4"ø HOLE
3"
7"
The University of Manitoba
Department of Mechanical Engineering
RECTANGULAR PLATE
SIZE
A
FSCM NO.
DWG NO.
REV
SCALE 1:2
SHEET 4 of 4

APPENDIX B

DIMENSIONAL DRAWING OF THE 6061 ALUMINUM ALLOY STEM

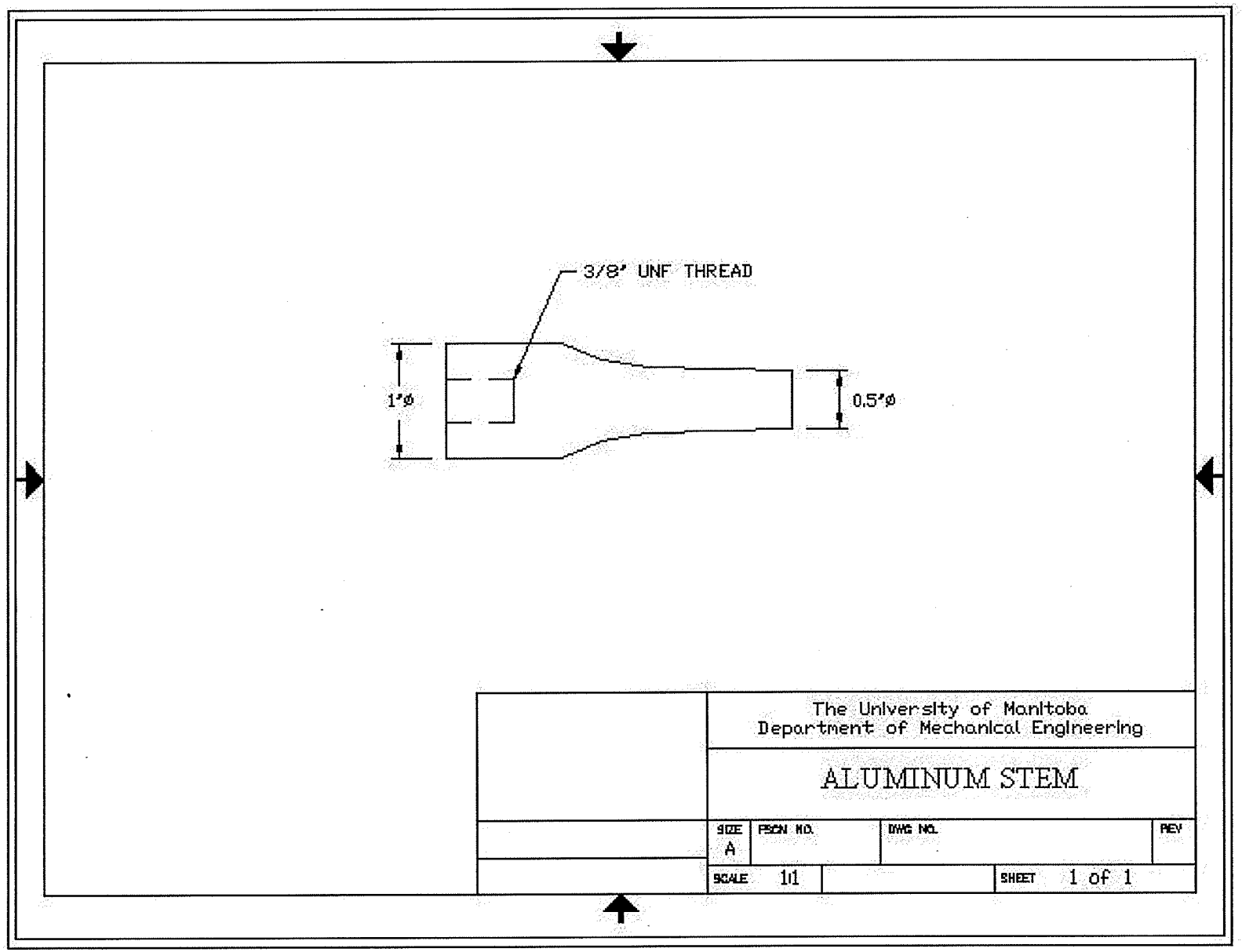
3/8" UNF THREAD
1"ø
0.5"ø
The University of Manitoba
Department of Mechanical Engineering
ALUMINUM STEM
SIZE
A
FSCM NO.
DWG NO.
REV
SCALE 1:1
SHEET 1 of 1